Faculdade de Engenharia da Universidade do Porto

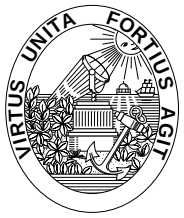

Atmospheric Flow over Forested and Non-Forested Complex Terrain

José Carlos Pereira Lopes da Costa
MSc in Mechanical Engineering
Universidade do Porto

Submited in partial satisfaction of the
requirements for the degree of
Doctor of Philosophy
in the
Universidade do Porto

July 2007

Atmospheric Flow over Forested and Non-Forested Complex Terrain

José Carlos Pereira Lopes da Costa

Abstract

The main purpose of this work was to contribute to the development of CFD (*Computational Fluid Dynamics*) tools for studying the wind flow over complex orography, both with and without forest, with applications to wind energy. For these purpose, a RaNS (*Reynolds averaged Navier-Stokes*) k-ε turbulence model is tuned, mainly its forest canopy model, using experimental data and LES (*Large-Eddy Simulation*) results for the establishment of benchmark solutions. The study includes a series of computer flow simulations of different type of flows, ranging from real cases to idealized flow over canopies.

The flow over *Serra de Alvoaça*, in Portugal, showed how CFD can be used at the wind farm design stage, providing an increased and detailed knowledge of the flow that point-sonic or cup anemometers cannot provide. Computer simulations have increased the confidence on the field data, since the quality of which was a matter of doubt. For instance, it was possible to determine that the highest speed-up did not occur at the highest location of a ridge, due to the high slope of the upstream terrain. The study was crucial in the last stage of design of the wind farm, enabling a final validation of wind farm layout.

The following study revealed the weakness of the computational tools available and the need for modelling the wind flow over forested regions. Code development was based on the simulation of real cases: a sparsely forested region in Scotland and a large forested region in the South of France. The canopy model by Svensson and Häggkvist (1990) was used. The results of the Scottish case were an improvement over previous computer simulations without the canopy model, and showed the difficulties of comparing detailed three-dimensional computer simulations with field data point measurements. In the case of the French site, agreement was excellent between mean velocity field measurements at 7 heights above the ground, between 48 and 100 m, and computer results. It was shown that the presence of the canopy could increase the turbulence levels by almost two orders of magnitude, when compared to the results obtained without the canopy.

The RaNS $k - \varepsilon$ based canopy models available in the literature typically differ in the number of terms used for modelling the canopy flow physics and the set of model constants. The two terms model class seems to become the established one, due to a more accurate representation of the turbulent spectral shortcut and enhancement of the turbulent dissipation process. Nevertheless, its performance is largely dependent on the

model constants, which show large differences in the published literature. The present work contributes to the clarification of this feature by systematically testing some of the available models, by comparing not only velocity and turbulent results but also a term-by-term comparison of the turbulence phenomena embedded in the transport equation of the turbulent kinetic energy as predicted by LES. Among the four canopy models tested, the Sanz (2003) canopy model presented the best results.

The Sanz (2003) procedure for determining of the canopy model constants, using k-ε turbulent model, was extended using k-ε-$\overline{v^2}$-f turbulent model (Durbin, 1991). An explicit derivation for the canopy related constants β_p and β_d was established, which became functions of the turbulence models constants. The various sets of canopy related constants were tested using both k-ε and k-ε-$\overline{v^2}$-f turbulence model. A canopy model constant set, named "CM1", proved to satisfactorily mimic the LES results when used on k-ε turbulent model. The results were an improvement compared to the Sanz (2003) canopy model constant set, and model "CM1" was the best model of all being tested in the present study.

Resumo

O objectivo principal deste trabalho foi contribuir para o desenvolvimento das ferramentas de Mecânica dos Fluidos Computacional (CFD – *Computational Fluid Dynamics*) destinadas ao estudo do vento sobre topografia complexa, com ou sem floresta, para aplicações de energia eólica. Para este efeito, foi testado e ajustado o modelo de turbulência k-ε, baseado no método das médias de Reynolds (RaNS – *Reynolds averaged Navier-Stokes*), sobretudo no que concerne à procura de um adequado modelo de floresta, usando como referência dados experimentais e a resultados de LES (*Large-Eddy Simulation*). Este estudo envolveu diversas simulações computacionais de vários tipos de escoamentos, indo desde topografias florestadas reais até vegetação com geometrias idealizadas.

O estudo do escoamento sobre a *Serra de Alvoaça*, em Portugal, demonstrou como o CFD pode ser usado no projecto de um parque eólico, fornecendo um conhecimento completo e detalhado do escoamento, impossível de obter apenas através de medições com anemómetros de copos ou anemómetros sónicos. As simulações computacionais do vento sobre o local aumentaram a confiança nas medições efectuadas no terreno, já que alguns dos seus resultados eram duvidosos. Nomeadamente, foi possível compreender a razão pela qual a velocidade era estranhamente mais reduzida nas zonas mais elevadas da cumeada, verificando-se que ela era fortemente influenciada pelo elevado declive do terreno a montante. O estudo foi crucial no último estágio do desenho do parque, validando o seu *layout* definitivo.

O estudo seguinte revelou as fraquezas das ferramentas CFD e a necessidade de a capacitar para a modelação de escoamentos em regiões florestadas. Efectuou-se desenvolvimento de código tendo por base casos reais: uma região esparsamente florestada na Escócia e uma região com largas zonas de floresta em França. Nestes casos foi aplicado o modelo de floresta de Svensson and Häggkvist (1990). Os resultados no caso escocês constituíram uma melhoria relativamente aos obtidos anteriormente sem modelo de floresta, revelando no entanto dificuldades associadas à comparação de simulações tridimensionais com medições pontuais efectuadas no terreno. No caso francês, a concordância revelou-se excelente entre a velocidade média medida em 7 alturas acima do solo, entre os 48 e os 100 m, e os resultados computacionais. Verificou-se que a presença de floresta pode incrementar os níveis de turbulência em quase duas ordens de grandeza, em comparação da modelização sem modelo de floresta.

Os modelos de floresta baseados no modelo RaNS k-ε disponíveis na literatura tipicamente diferem no número de termos usados para a modelação da física do escoamento e no conjunto de constantes usadas no modelo. As modelações com dois termos parecem ser as mais adequadas, devidos à sua mais precisa representação do atalho espectral da turbulência existente entre a vegetação, e do seu processo de dissipativo. No entanto, a sua performance é muito dependente nas constantes do modelo, muito diferentes entre as diversas publicações. O presente trabalho contribui para a clarificação desta questão, através de testes sistemáticos de alguns dos diversos modelos que não só comparam resultados de velocidade e turbulência, mas também através da comparação termo a termo dos fenómenos da turbulência contidos na equação de transporte da energia cinética da turbulência como prevista pelo LES. De entre os quatro modelos de floresta testados, o modelo de Sanz (2003) apresentou os melhores resultados.

O procedimento de Sanz (2003) para determinar as constantes do modelo de floresta, usando o modelo de turbulência k-ε, foi estendido usando o modelo k-ε-$\overline{v^2}$-f (Durbin, 1991). Conseguiu-se obter uma relação explicita para as constantes do modelo de floresta β_p and β_d, tornando-as apenas dependentes das constantes do modelo de turbulência. Os diversos conjuntos de constantes de modelo de floresta obtidos foram testados usando os modelos k-ε and k-ε-$\overline{v^2}$-f. Um conjunto designado por "CM1", quando aplicado ao modelo de turbulência k-ε, imitou de forma satisfatória os resultados do LES. Estes resultados constituíram uma significativa melhoria do modelo de floresta relativamente ao modelo de Sanz (2003), sendo o modelo "CM1" o melhor modelo de floresta entre os diversos testados neste trabalho.

Résumé

Le but principal de ce travail est de contribuer pour le développement d'outils de simulation d'écoulements en ordinateur (CFD - *Computational Fluid Dynamics*), à savoir des modèles basés sur RaNS (*Reynolds averaged Navier-Stokes*), pour l'étude des écoulements atmosphériques, et particulièrement du comportement du vent sur des topographies complexes avec ou sans forêt, potentiellement destinée à la production d'énergie éolienne. Pour cet effet, le modèle de turbulence k-ε, basé sur la méthode des moyennes de Reynolds (RaNS), surtout en ce qui touche la recherche d'un certain modèle de forêt, utilisant comme repères des donnés expérimentales et des donnés provenant du model LES (*Large-Eddy Simulation*). Cette étude a impliqué diverses simulations informatiques de plusieurs types d'écoulement, allant de topographies boisées réelles à des végétations aux géométries idéalisées.

L'étude de l'écoulement sur *Serra de Alvoaça*, au Portugal, a démontré comment le CFD peut être utilisée dans le projet d'un parc éolien, en permettant une complète et très détaillée connaissance de l'écoulement, impossible d'obtenir uniquement à travers des mesures provenant des anémomètres à gobelet ou soniques. Les simulations informatiques du vent sur le lieu ont augmenté la confiance dans les mesures effectuées sur place, d'autant plus qu'il y avait certains doutes sur leur fiabilité. Notamment, cela a permit de comprendre que la vitesse était plus réduite dans les zones les plus élevé de la ligne de sommet parce qu'elles étaient fortement influencée par la forte inclinaison du terrain au sommet du mont. L'étude a été crucial pour la conception du parc en validant sont *layout* définitif.

L'étude suivante a révélé les faiblesses des outils CFD ainsi que la nécessité de faire la simulation des écoulements sur les régions de forêt. En conséquence on a développé un code ayant pour base des cas réels : une région peu boisée en Écosse et une région avec des grandes zones de forêt en France. Dans ces cas le modèle de forêt de Svensson and Häggkvist (1990) a été appliqué. Les résultats dans le cas écossais ont constitué une amélioration à l'égard des résultats obtenus précédemment sans le modèle de forêt, révélant néanmoins des difficultés associées à la comparaison de simulations tridimensionnelles avec des mesures rapides effectuées sur le terrain. Dans le cas français, l'accord entre les mesures de la vitesse moyenne recueilli à 7 hauteur différentes au-dessus du sol, entre 48 et 100 m, et les résultats informatiques a été excellent. Il s'est vérifié que la présence de forêt peut augmenter deux ordres de grandeur aux niveaux de turbulence vérifiés dans la simulation

sans modèle de forêt.

Les modèles de forêt basés sur le RaNS k-ε disponibles dans la littérature diffèrent typiquement dans le nombre de termes utilisés pour le modelage de la physique de l'écoulement et dans l'ensemble de constantes utilisées dans le modèle. Les modelages avec deux termes semblent être ajustés, dus à sa plus précise représentation du raccourci spectral de la turbulence existante entre la végétation ainsi que de son processus de dissipatif. Néanmoins, sa performance est très dépendante des constantes du modèle, très différentes dans les diverses publications. Le présent travail contribue à la clarification de cette question, à travers des essais systématiques de certains modèles qui, non seulement comparent des résultats de la vitesse et de la turbulence, mais aussi comparent terme à terme les phénomènes de la turbulence contenus dans l'équation de transport d'énergie cinétique de la turbulence tel que prévue par LES. Parmi les quatre modèles de forêt testés, le modèle de Sanz (2003) a présenté les meilleurs résultats.

La procédure de Sanz (2003) pour déterminer les constantes du modèle de forêt, utilisant le modèle de turbulence k-ε, a été élargie utilisant le modèle k-ε-$\overline{v^2}$-f (Durbin, 1991). On a réussi à obtenir une relation explicite pour les constantes du modèle de forêt β_p et β_d qui les rendes uniquement dépendantes des constantes du modèle de turbulence. Les plusieurs ensembles de constantes de modèle de forêt obtenus ont été testés sur les modèles k-ε et k-ε-$\overline{v^2}$-f. Un ensemble désigné par CM1 appliquée au modèle de turbulence k-ε a imité de forme satisfaisante les résultats de LES. Ces résultats ont constitué une significative amélioration du modèle de forêt à l'égard du modèle de Sanz (2003), étant le modèle CM1 le meilleur modèle de forêt entre plusieurs testés dans ce travail. Parmi les quatre modèles de forêt testés, le modèle de Sanz (2003) a présenté les meilleurs résultats.

Agradecimentos

Gostaria de agradecer ao Prof. Doutor José Manuel Laginha Mestre da Palma a confiança que depositou em mim para a execução este trabalho. Agradeço também e especialmente todo o seu empenho, disponibilidade e paciência manifestadas na sua orientação.

Agradeço também ao Doutor Fernando Aristides Castro, co-orientador, amigo e colega, por toda a orientação, encorajamento e amizade.

Um outro agradecimento é dirigido aos restantes colaboradores do CEsA – Centro de Estudos de Energia Eólica e Escoamentos Atmosféricos – especialmente para o Doutor Carlos Santos, amigo sempre disponível e para o Doutor Alexandre Silva Lopes, sem o qual todos os cálculos à volta do LES teriam sido bastante mais complicados. Também para o colega Carlos Rodrigues, pelo sempre excessivo empenho em ajudar.

À família, amigos e colegas de ofício não directamente envolvidos neste trabalho, que pelo incentivo ou pelo simples facto de existirem tornaram todos estes anos de trabalho memoráveis, gostaria de manifestar o meu grande apreço.

I would like to thanks RES (Renewable Energy Systems Ltd. - UK), specialy to Peter Stuart, for all the cooperation in this work.

Agradeço também ao ISEP - Instituto Superior de Engenharia do Porto - onde tenho a honra de ser docente, pelo apoio que possibilitou a execução deste trabalho.

Por último, agradeço a bolsa que financiou este trabalho de doutoramento, às instituições ligadas ao PRODEP - Programa de Desenvolvimento Educativo para Portugal.

Porto, 29 de Julho de 2007

À memória de meu pai, à minha mãe,
e à Carla, a quem coube a árdua tarefa de me fazer feliz!

Contents

List of Figures

List of Tables

Nomenclature

Upper-case Roman

C_μ^* k-ε-$\overline{v^2}$-f turbulence model constant

C_μ k-ε turbulence model constant

C_D Drag coefficient

C_L k-ε-$\overline{v^2}$-f turbulence model constant

C_z Simplification used in the canopy model - $C_z = C_D a$

$C_{\varepsilon 1}$ k-ε turbulence model constant

$C_{\varepsilon 2}$ k-ε turbulence model constant

$C_{\varepsilon 4}$ Canopy model constant

$C_{\varepsilon 5}$ Canopy model constant

C_{f1} k-ε-$\overline{v^2}$-f turbulence model constant

C_{f2} k-ε-$\overline{v^2}$-f turbulence model constant

F_i Canopy drag force component

LAI Leaf Area Index – $LAI = \int_0^{h_{\text{can}}} a(z)dz$

P Fluid pressure ensemble average

$\mathcal{P}$ Specific wind power - $\mathcal{P} = \frac{1}{2}\rho V_h^3$

$\mathcal{P}_k$ k equation production term – $\mathcal{P}_k = \sigma_{ij}\frac{\partial U_i}{\partial x_j}$

$S(i,\theta)$ Speed-up parameter – $S(i,\theta) = \frac{V_h(i,\theta)}{V_{h_{Ref}}(\theta)}$

S_ε ε equation canopy term

S_k k equation canopy term

S_{ij} Rate-of-strain tensor - $S_{ij} = \frac{1}{2}\left(\frac{\partial u_i}{\partial x_j} + \frac{\partial u_j}{\partial x_i}\right)$

$\overline{S}_{ij}$ Rate-of-strain tensor using filtered velocities – $\overline{S}_{ij} = \frac{1}{2}\left(\frac{\partial \overline{u}_i}{\partial x_j} + \frac{\partial \overline{u}_j}{\partial x_i}\right)$

T_{ij} Molecular viscosity stress tensor of the ensemble averaged velocity – $T_{ij} = \mu\left(\frac{\partial U_i}{\partial x_j} + \frac{\partial U_j}{\partial x_i}\right)$

TI Horizontal turbulence intensity – $TI = \frac{(2/3k)^{1/2}}{V_h}$

$\mathbf{U}$ Ensemble average velocity vector

U Wind direction component of ensemble averaged velocity

U_i Velocity ensemble average component (or $\langle u_i \rangle$)

U_∞ Free stream velocity

U_{mean} Longitudinal velocity averaged in all the domain (Chapters 5 and 6)

U_{med} Same as U_{mean}

V Transversal to wind direction component of ensemble averaged velocity

V_h Wind horizontal velocity - $\sqrt{U^2 + V^2}$

V_z Wind vertical velocity (also presented as W)

W Vertical component of ensemble averaged velocity

Lower-case Roman

a Leaf area density - [m^2/m^3]

$\overline{f}$ Function used in the k-ε-$\overline{v^2}$-f turbulence model, on its "code friendly" version – $f = \overline{f} - 5\varepsilon\frac{\overline{v^2}}{k^2}$

f Function used in the k-ε-$\overline{v^2}$-f turbulence model

h_{can} Canopy heigh

k Turbulent kinetic energy – $k = \frac{1}{2}\left(\langle u'^2 \rangle + \langle v'^2 \rangle + \langle w'^2 \rangle\right)$

k_h "Horizontal" turbulent kinetic energy – $k_h = \frac{2}{3}k + \nu_t\frac{\partial W}{\partial z}$

l_m Mixing length

p	Fluid pressure
s'_{ij}	Fluctuating rate-of-strain tensor – $s'_{ij} = \frac{1}{2}\left(\frac{\partial u'_i}{\partial x_j} + \frac{\partial u'_j}{\partial x_i}\right)$
t	time
$\mathbf{u}$	Velocity vector
$\overline{\mathbf{u}}$	Filtered velocity vector
$\overline{u}_i$	Filtered velocity component in direction i
u	Wind direction velocity component
u'	Turbulent fluctuation of the wind direction velocity component
u^*	Friction velocity
u_i	Velocity component in direction i
u'_i	u_i turbulent fluctuation
$\overline{v^2}$	Ensemble average of the velocity fluctuation normal to the streamlines. Scalar used in the k-ε-$\overline{v^2}$-f turbulence model
v	Wind velocity transversal component
v'	Turbulent fluctuation of the wind velocity transversal component
w	Wind velocity vertical component
w'	Turbulent fluctuation of the wind velocity vertical component
$\boldsymbol{x}$	Position vector
x	Cartesian longitudinal coordinate
x_i	Cartesian coordinate in direction i
y	Cartesian transversal coordinate
z	Cartesian vertical coordinate
z_0	Roughness length
z_{agl}	Vertical coordinate above ground level

Upper-case Greek

Δt Calculation time step

Δx Mesh control volume dimension along the wind direction

Δy Mesh control volume dimension, transversal to wind direction

Δz Mesh control volume dimension on the vertical direction

Lower-case Greek

α Wind profile shear factor

α' Dimensionless coefficient (Massman, 1997) – $\alpha' = 0.05$

α'' Dimensionless parameter – $\alpha'' = \sigma_\varepsilon \left(C_{\varepsilon 2} - C_{\varepsilon 2}\right)$ - see equation (6.34)

β Dimensionless parameter – $\beta = \sqrt{\frac{C_\mu \alpha''^2}{1+C_{f1}} \left(\frac{2}{3} C_{f1} + C_{f2} + \frac{2\alpha'' C_L^2}{C_\mu^*}\right)}$ - see equation (6.34)

β_d Canopy model constant

β_p Canopy model constant

δ Boundary layer height of the inlet flow

δ_{ij} Kronecker tensor

κ Von Karmann constant – $\kappa = 0.41$

μ Dynamic molecular viscosity

μ_t Dynamic turbulent viscosity

ν Molecular cinematic viscosity

ν_t Turbulent cinematic viscosity

ρ Density

σ_ε k-ε turbulence model constant

σ_k k-ε turbulence model constant

σ_{ij} Turbulent viscosity stress tensor – $\sigma_{ij} = -\frac{2}{3}\rho k \delta_{ij} + \mu_t \left(\frac{\partial U_i}{\partial x_j} + \frac{\partial U_j}{\partial x_i}\right)$

τ_{xz}^* Shear stress at the top of the canopy – see equations (5.5) and (5.6)

τ_{ij}^R Sub-grid stress tensor (or residual stress tensor) – $\tau_{ij}^R = \rho\overline{u_i u_j} - \rho\overline{u}_i\overline{u}_j$

τ_{ij} Molecular viscosity stress tensor – $\tau_{ij} = 2\mu S_{ij}$

ε Dissipation rate of kinetic turbulent energy

Symbols

$( )'$ Perturbation

$\langle( )\rangle$ Ensemble average (upper-case is also used for the same purpose)

$\overline{( )}$ Filtered

$|( )|$ Vector norm

Abbreviations

agl Above ground level

CFD Computational fluid dynamics

DNS Direct Navier-Stokes

LES Large-eddy Simulation

RaNS Reynolds averaged Navier-Stokes

TKE Turbulent kinetic energy

WAsP Wind Atlas Analysis and Application Program. See Mortensen et al. (2004).

Chapter 1

Introduction

The study of wind flow around wind farm is an important issue in order to take decisions about location, layout, operation and performance of the wind farm. A classical approach involves wind measurements, which are restricted to a small number, two or three, of mast locations on the field. It is a hard task to characterize the whole domain with such a small number of data points, and experience and skills are crucial in all stages of wind farm design.

The wind energy resource engineering is based on a well established methodology, comprising field measurements, using cup anemometer and wind vanes for a minimum period of one year, followed by wind resource evaluation, recurring to linearized versions of the fundamental equations of the fluid flow (Troen and Petersen, 1989).

The wind flow over complex terrain poses a series of new problems that cannot be tackled by conventional tools mentioned above, and often requires more detailed field measurements and engineering calculations, to infer the overall quality of the site and decide on the most convenient location of every wind turbine. The difficulties and uncertainties related to wind flow over complex terrain have been a recurrent, unsolved, problem listed in many publications, namely those edited under the auspices of the *EWEA – European Wind Energy Association* (EWEA, 2005).

In recent years, computational fluid dynamics (CFD) have played a role in this issue, providing the possibility of a detailed study of the whole extent of a wind flow around a wind farm. However the complex orography and topographic elements, such as forest canopy, pose complex problems and there is a large field of study in order to make CFD a reliable and useful tool in wind engineering.

1.1 Motivations of this work

Wind energy engineering relies on software applications, mathematical models, namely the well known so-called WAsP (Mortensen et al., 2004). This software uses the local orography, terrain roughness, combined with measured data obtained on site. The whole place characterization is based on a wind speed-up (wind increase) proportional to the terrain elevation, departing from some well known locations where wind behaviour was previously measured. This tool, WAsP and programs alike, proved to be very useful, mainly on gentle orography, and have been used extensively in wind farm design. However, its application to complex orography has always been questioned.

Many wind energy potential sites are located in high mountains, as it could be found in Portugal, and surrounded with complex elements such as forests and sharp ridges. The wind behaviour on those places may not be predicted using linear or simple methods. It usually involves unexpected wind direction changes, and high turbulent phenomena such as recirculation zones or unsteady flow.

Computer simulation of fluid flows (CFD) has been extensively used in many fields of science and engineering, namely automotive, aeronautics and weather prediction, as opposed to wind energy engineering, where it is not clear how and at what stage of a wind farm design CFD can be used. The main advantages of these tools is their ability to capture a more realistic wind behaviour, such as recirculation zones downstream of a hill (not detected by WAsP). It also quantifies and gives important information about the propagation of the turbulent kinetic energy, which is an important, and many times neglected, issue to define "may" or "may not" locations for wind turbines. Nevertheless, there are many aspects to improve on the CFD capabilities to deal with some topographical elements and mimic the wind conditions in its vicinity. Probably one of most important is the forest canopy.

Forest regions are often in remote and inhabited areas, where the use of land for forest plantation precludes its use by any other activity, including farming. The increased number of wind parks and the shortage of ideal (or near-to-ideal) sites, has forced wind farm installers to, at least, consider the possibility of installing wind farms in the vicinity or within forests, adding an additional use (and value) to the land. This was made possible also because of increasing size, power and efficiency of modern wind turbines, operating at higher distances from the ground, and well above the trees. However, forested zones may produce turbulent structures that propagate its effects much above trees top. It is then important for CFD codes for wind engineering applications to have reliable canopy models, that could fairly reproduce its effects in the wind flow.

1.2 Brief bibliographic review

A feature that distinguishes canopy flows from more familiar boundary layer flows is the removal of momentum from the air stream as aerodynamic drag on the foliage over an extended vertical region, rather than just at the surface plane. This can also be explained, instead of a boundary layer, considering the combination of the flow inside and above the canopy as a plane mixing layer, with a velocity profile inflection point depending on the canopy height and foliage density (Raupach, 1994). The momentum removal, i.e. momentum sink, is combined with a high rate of dissipation of turbulent kinetic energy (TKE) by the intense very fine scale shear layers, due to the vegetation. As the larger eddies act against the foliage, wake scale eddies are formed and turbulent energy dissipation is submitted to the *spectral short-cut* mechanism (Finnigan and Belcher, 2004), which enhances TKE transfer from the energy-containing scales to the dissipation scales.

The wind flow over vegetation has been of interest in many areas of application. Because of its importance in mass and heat exchanges between the atmosphere and the soil, the flow over canopies has attracted the interest of applied meteorologists and climatologists. Many of the published literature on atmospheric flow over canopies is mainly concerned with this type of problems.

To our knowledge, the study by Neff and Meroney (1998) is the only one available in the published literature that was driven by a motivation clearly related with wind energy. There is not much information available when it comes to analyse this same problem from an engineering point of view, and this is something of which the wind energy community is well aware of, as shown for instance by the *Workshop on the Influence of Trees on Wind Farm Energy Yields*, organized under the auspices of the BWEA (2004).

Recent developments have been made within the framework of linear models, namely the study by Finnigan and Belcher (2004), an extension to the seminal work by Jackson and Hunt (1975), on the wind flow over hills, but now considering the flow over forested hills; or upgraded versions of the WAsP software application, Dellwik et al. (2006). Forested regions are modelled using an exaggerated roughness length and a zero-plane displacement, i.e. a vertical shift of the boundary to roughly coincide with the top of the trees, e.g. Raupach (1994) and Verhoef et al. (1997). Recently, Harman and Finnigan (2007) have established a unified theory for the flow in the canopy and roughness sub-layer.

The state of the art of canopy flows was set by Raupach and Tom (1981) and more recently by Finnigan (2000). These two review papers, 20 years apart, evidence two alternative, and in our view also complementary, approaches to the modelling of flow over vegetation, respectively the Reynolds-averaged-Navier-Stokes (RaNS) and the Large-Eddy Simulation (LES). The physics of the flow over trees, as interpreted by Finnigan (2000), because of its eddy and time-dependent structure can only be modelled by LES. The work by Shaw and Shumann (1992) is one of such studies, showing good agreement with measured field data, to which others followed, e.g. Dwyer et al. (1997), Su et al. (1998), Patton et al.

(1998), Brown et al. (2001), Yang et al. (2006) and Mao et al. (2007), all taking advantage of LES as a tool for studying the turbulent field, spectra and its mechanisms, within and above a forest canopy. Other kind of LES studies go beyond the simple assumption of the canopy as a momentum sink, simulating the flow among the canopy elements, in order to fully characterize canopy parameters, such as its drag coefficient, or to explore the flow in detail. Yue et al. (2007) and Chester et al. (2007) uses plant representation as fractal vegetation, while Xie and Castro (2006) uses staggered wall-mounted cubes to study the urban obstacles canopy.

In spite of all of its advantages, because LES requires high computational resources, it is not a tool for engineering daily routines. Computer simulations of atmospheric flows tend to rely on RANS turbulence models. According with Wilson et al. (1998), gradient diffusion models are good enough if there is no need to know the individual terms of the Reynolds stress tensor, and in practical applications, the greatest uncertainty is still associated with the canopy drag coefficients and not with the turbulence model (Pinard and Wilson, 2001). Katul et al. (2004), in an overview of canopy models available on literature, argue that even simple one-equation turbulence model are good enough. However, being a widespread turbulence model found in many commercial CFD codes, canopy models are usually extensions of the two-equation k-ε model (Launder and Spalding, 1974). Contrary to standard applications of the k-ε model, the literature survey shows a still ongoing development of canopy models extensions to this model, cf. Katul et al. (2004); Sogachev and Panferov (2006). Agreement cannot be found in simple matters such as the mathematical form of the terms in the transport equation for k and ε, or the most appropriate set of constants (Svensson and Häggkvist, 1990; Liu et al., 1998; Green, 1992; Sanz, 2003; Foudhil et al., 2005). Nevertheless, a good use has been made of these models for solving practical and engineering problems, eg. Kobayashi et al. (1994); Lopes da Costa et al. (2006).

Experimental studies, laboratory or field experiments, are crucial for our understanding of the physics embodied in canopy flows. Poggi and Katul (2006) analysed the TKE and scalar spectra of the flow among a canopy, involving the analysis of the *spectral short-cut*. Studies of the combination of canopy with terrain orography are also a recurring issue using idealized sinusoidal two-dimensional hill covered with vegetation canopy (Ruck and Adams, 1991). The *ejection-sweep* phenomena, found above a forest canopy along with high order turbulence statistics, is studied by (Poggi and Katul, 2007b), also in the case of the flow over forested hills; the recirculating region formed in the hill wake is observed (Poggi and Katul, 2007a) and it was noticed that, due to the canopy, it cannot be characterized by a classical rotor, but by an intermittent zone with alternating positive and negative velocity. Due to its inhomogeneous behaviour that demands two- or three-dimensional deployment of instruments, field experiments in high and dense canopies are a daunting task, and field detailed measurements are rare. The Irvine et al. (1997) work, that presents field results for a transition moorland to forest on a almost flat area (with a very gentle slope), is one of the most used reference on this matter.

1.3 The contributions of this study

The major aim of this thesis is to contribute to an increased knowledge on the flow over complex terrain either without or with trees and develop software tools that can properly address this problem. Our contribution was made via the assessment of limitations of currently available mathematical models of the RaNS type, namely extensions to the k-ε turbulence model. This exercise was carried out by comparison against LES results, showing the weakness of some available models, which were unable to mimic the main turbulence mechanisms. Alternative set of canopy related model constants were derived, yielding improved predictions of the flow over homogeneous forests and clearings.

The works by Castro (1997) and Castro et al. (2003) were our starting points, and most of the canopy models and variants developed and presented in this thesis, were implemented into VENTOS® computer code (Castro and Palma, 2002) and are currently being used in the design methodology of modern wind farms.

1.4 Outline of this thesis

The subject being addressed in the present dissertation brings together two problems of their own: computer simulations of the wind flow over complex terrain and the wind flow over forest canopies.

We begin, in Chapter 2, to present the fundamental equations of the mathematical models used in this work. A brief description is made of the RaNS turbulence models, and also the LES formulation and its sub-grid model. In the final section the canopy model formulation and constants, used in the RaNS calculations, are described.

On a first approach, in Chapter 3, simulations over a complex terrain for a wind farm location at *Alvoaça* (near *Serra da Estrela* highs - Portugal) were made. The flow particularities of this site were studied, namely the unsteady behaviour of the flow that forced us to use URaNS simulations.

In Chapter 4, a simple canopy model was tested and analysed, comparing its results with field measurements on a couple of locations (in Scotland and France), with an important presence of forest canopy. Results proved to be more satisfying than those produced considering canopy as surface roughness. However, the turbulent kinetic energy seemed to be not always well estimated.

Several other canopy models were studied in Chapter 5, tested and compared with the previous canopy model. The calculation of the two k and ε canopy drag terms was then reviewed, dividing each other in source and sink terms. This modification was intended to include in the model a turbulent phenomena known as “canopy turbulent short-cut”, as described by Finnigan (2000). Some calculations were implemented also for a flat and

horizontally continuous forest. LES results for the same situation were produced, based on Shaw and Shumann (1992) seminal work regarding LES on canopy flows. Its results were compared with several canopy models purposed by different authors for RANS k-ε turbulence model. Although the "canopy turbulent short-cut" principle does not guarantee good results, it showed to be a condition *sine qua non* to reproduce a good turbulence behaviour. This was observed, comparing the RaNS and LES budget terms of the turbulent kinetic energy (k) transport equation (production, dissipation (ε), diffusion and canopy model term). Among the different canopy models, the model presented by Katul et al. (2004) and deduced by Sanz (2003) had the best results.

In Chapter 6, we expand the Sanz (2003) analytical deduction of the canopy model coefficients, in order to find a better canopy model constant set. The deduction of Sanz (2003) model departed from the use of Kolmogorov's relation on a flow within a portion of dense and homogeneous canopy, were the mixing length does not vary. This relation, applied in the model equations allows to create some constraints on k and ε equation canopy terms, that establish simple relations between canopy model coefficients. In order to avoid the need to specify some canopy constants, the procedure of Sanz (2003) was applied to the k-ε-v^2-f model (Durbin, 1991), that has two additional equations. This extra informations enable the determination of an additional pair of constants, not possible with the standard k-ε model formulation. A new coefficients set was them created and tested, producing more adjusted results to those obtained by others canopy models previously tested.

In Chapter 7, the new canopy coefficients set was then applied to complex terrain simulations studied on the beginning of this work, and its results analysed and compared with those obtained by the simpler canopy model. Some improvement was found, mainly in the turbulent kinetic energy results which values were lower than those produced by the former model (Svensson and Häggkvist, 1990). It was also briefly study the turbulence propagation in the studied domain, and some suggestions were made in order to obtain results closer to the measurements.

The conclusions of this work are presented in Chapter 8, along with the final observations and some possible issues for future work.

Chapter 2

Mathematical Models

Abstract

The fundamental equations of the mathematical models used in this work are presented. A brief description of the Reynolds averaged Navier-Stokes (RaNS) equations is made, starting from the fundamental fluid mechanical equations. The two turbulence models used on RaNS calculations, k-ε and k-ε-$\overline{v^2}$-f models, are described. The Large Eddy-Simulations (LES) method, also used in this work, and its sub-grid model are presented. Finally, the application of the canopy model in those different CFD methods is described.

2.1 Introduction

The mathematical model for incompressible flows, which is the approach used here for the study of the atmospheric wind flow, is based on several differential simultaneous equations: the continuity equation and the momentum conservation equations, also known as Navier-Stokes equations. The next section will present those fundamental equations together with the simplifications and numerical techniques used on the following chapters.

As it is well known, and for the current state of knowledge, the solution of this model is not reachable without the use of numerical tools, such as the finite volumes or finite elements methods. In this work, we used the finite volume method, implemented on the two computer programs developed by Castro (1997), using RaNS turbulence models - VENTOS® - and Silva Lopes (2000), using LES.

The most wide spread method used to model the wind flow is the RaNS method. This work is a contribution for the improvement of the RaNS method, mainly using the k-ε turbulence model, in the simulation of atmospheric flows over complex orography and

topography elements, such as forest canopy. The LES method is here used as a tool to benchmark the results obtained by the different solutions that are tested with the RaNS method.

2.2 Fundamental equations

The principles of conservation of mass and momentum, when applied to a portion of fluid volume - *control volume* -, produce the fundamental equations of fluid mechanics. From the mass conservation principle we obtain the continuity equation

$$\frac{\partial (\rho u_i)}{\partial x_i} = 0, \tag{2.1}$$

and the momentum conservation principle (second Newton law), when applied to a portion of fluid volume, yields the Navier-Stokes equations,

$$\frac{\partial (\rho u_i)}{\partial t} + \frac{\partial (\rho u_i u_j)}{\partial x_j} = \frac{\partial \tau_{ij}}{\partial x_j} - \frac{\partial p}{\partial x_i} + F_i, \tag{2.2}$$

were x_i are the Cartesian coordinates, u_i are the velocity components, ρ is the density, t represents time, p the fluid pressure and F_i is an external force that may act over the fluid.

In this work it is considered that the wind flow is an incompressible flow, and that the air is a Newtonian fluid; being so, there is a linear relation between the rate-of-strain tensor,

$$S_{ij} = \frac{1}{2}\left(\frac{\partial u_i}{\partial x_j} + \frac{\partial u_j}{\partial x_i}\right), \tag{2.3}$$

and the stress tensor,

$$\tau_{ij} = 2\mu S_{ij}. \tag{2.4}$$

It is possible to solve those equations using numerical techniques. It is called *Direct Numerical Simulation* - DNS. However, for complex geometry problems this involves a great deal of time and computer resources and frequently it is simply not feasible. Alternative methods must be used in engineering studies, less demanding on computational resources, that enable us to obtain relevant solutions for the most of the flow geometries, such as the wind flow over topography. Two of those methods are used in this work: *Reynolds averaged Navier-Stokes* (RaNS) method, and *Large Eddy Simulation* (LES). In RaNS all the turbulence is modelled, while LES uses a turbulence model for the turbulent scales smaller then the mesh (sub-grid model), and calculates the turbulence that can be captured by the mesh resolution.

In the next sections we will describe this methods with more detail.

2.2.1 Reynolds averaged Navier-Stokes equations

The *Reynolds averaged Navier-Stokes* method (RaNS) consists in decomposing a instantaneous variable value on two terms: a ensemble averaged term and a turbulent fluctuating term. For instance, in the case of the x_i-direction velocity vector component u_i, its ensemble average is denoted as U_i (or $\langle u_i \rangle$), and is defined as

$$U_i = \langle u_i \rangle \equiv \lim_{N \to \infty} \frac{1}{N} \sum_{n=1}^{N} (u_i)_n \,, \tag{2.5}$$

being N the number of similar hypothetical experiments made to reproduce the flow under study, and to measure u_i. The velocity vector component u_i may be then defined by

$$u_i(\boldsymbol{x}, t) = U_i(\boldsymbol{x}, t) + u_i'(\boldsymbol{x}, t) \,, \tag{2.6}$$

where u_i' is the turbulent fluctuating term of u_i.

This formulation is the more generic, and is established for transient flows. It is named *Unsteady Reynolds averaged Navier-Stokes* formulation (URaNS). From the continuity and Navier-Stokes equations (2.1 and 2.2), after Reynolds decomposition (2.6) and averaging are

$$\frac{\partial U_j}{\partial x_j} = 0 \,, \tag{2.7}$$

$$\rho \frac{\partial U_i}{\partial t} + \rho \frac{\partial U_i U_j}{\partial x_j} = -\frac{\partial P}{\partial x_i} - \rho \frac{\partial \left\langle u_i' u_j' \right\rangle}{\partial x_j} + \frac{\partial T_{ij}}{\partial x_j} + F_i \,, \tag{2.8}$$

where

$$T_{ij} = \mu \left(\frac{\partial U_i}{\partial x_j} + \frac{\partial U_j}{\partial x_i} \right) \,, \tag{2.9}$$

and pressure p is composed by its ensemble averaged mean and fluctuating parts P and p' respectively, with ρ and μ the density and the dynamic molecular viscosity of air, here considered constants. The $\left\langle u_i' u_j' \right\rangle$ term is the ensemble averaged of the product of the velocity fluctuating parts. This represents the turbulent effects on the ensemble averaged velocity field, also known as *Reynolds stress tensor*. The term F_i represents an external force over the fluid, that in our calculations will be the drag force induced be the presence of the canopy.

In the majority of the cases, we will be dealing with stationary flows and the previous formulation can be simplified, considering

$$u_i(\boldsymbol{x}, t) = U_i(\boldsymbol{x}) + u_i'(\boldsymbol{x}, t) \,, \tag{2.10}$$

where $U_i(\boldsymbol{x})$ became the time average value of $u_i(\boldsymbol{x}, t)$. In those cases, and in opposition to URaNS, we will call it simply RaNS. The equations for the mean velocity and pressure

would be simplified as

$$\frac{\partial U_j}{\partial x_j} = 0, \tag{2.11}$$

$$\rho\frac{\partial U_i U_j}{\partial x_j} = -\frac{\partial P}{\partial x_i} - \rho\frac{\partial \langle u_i' u_j' \rangle}{\partial x_j} + \frac{\partial T_{ij}}{\partial x_j} + F_i. \tag{2.12}$$

The next sub-sections present the two different turbulence models used in this work, and the way how they deal with the Reynolds stress tensor, $\langle u_i' u_j' \rangle$.

The RaNS calculations for this work were made using the code VENTOS®, developed by Castro (1997), with some recent modifications.

2.2.1.1 k-ε turbulence model

The k-ε turbulence model uses two scalars: k stands for the turbulent kinetic energy,

$$k = \frac{1}{2}\left(\langle u'^2 \rangle + \langle v'^2 \rangle + \langle w'^2 \rangle\right), \tag{2.13}$$

and ε as its dissipation rate. The Reynolds stress tensor is modelled using

$$-\rho\left\langle u_i' u_j' \right\rangle = 2\mu_t\left(\frac{\partial U_i}{\partial x_j} + \frac{\partial U_j}{\partial x_i}\right) - \frac{2}{3}\rho k \delta_{ij}, \tag{2.14}$$

applying the Boussinesq concept for the turbulent viscosity, μ_t. The turbulent viscosity is obtained by

$$\mu_t = \rho C_\mu \frac{k^2}{\varepsilon}, \tag{2.15}$$

where C_μ characterizes the relation between turbulent shear stress and turbulent kinetic energy:

$$C_\mu \equiv \sqrt{\frac{\tau_{xz}}{\rho k}}. \tag{2.16}$$

Along with equations (2.7) and (2.8) (or equations (2.11) and (2.12)), the k-ε formulation treats k and ε as flow scalars, and deals with them using the following equations:

$$\rho\frac{\partial k}{\partial t} + \rho\frac{\partial U_i k}{\partial x_j} = \frac{\partial}{\partial x_j}\left[\left(\mu + \frac{\mu_t}{\sigma_k}\right)\frac{\partial k}{\partial x_j}\right] + \mathcal{P}_k - \rho\varepsilon + S_k\ , \tag{2.17}$$

$$\rho\frac{\partial \varepsilon}{\partial t} + \rho\frac{\partial U_i \varepsilon}{\partial x_j} = \frac{\partial}{\partial x_j}\left[\left(\mu + \frac{\mu_t}{\sigma_\varepsilon}\right)\frac{\partial \varepsilon}{\partial x_j}\right] + \frac{\varepsilon}{k}\left(C_{\varepsilon 1}\mathcal{P}_k - C_{\varepsilon 2}\rho\varepsilon\right) + S_\varepsilon. \tag{2.18}$$

The turbulent production is defined as,

$$\mathcal{P}_k = \sigma_{ij}\frac{\partial U_i}{\partial x_j}, \tag{2.19}$$

Table 2.1: Constants used in the k-ε turbulence model.

	$C_{\varepsilon 1}$	$C_{\varepsilon 2}$	C_μ	σ_k	σ_ε
Standard	1.44	1.92	0.090	1.0	1.30
Atmospheric flow	1.44	1.92	0.033	1.0	1.84

where

$$\sigma_{ij} = -\frac{2}{3}\rho k \delta_{ij} + \mu_t \left(\frac{\partial U_i}{\partial x_j} + \frac{\partial U_j}{\partial x_i} \right). \tag{2.20}$$

The source/sink terms, S_k and S_ε found in the RaNS k and ε equations, were introduced in the equations to model the effects of an eventual forest canopy presence in the flow. Its formulation, which is the main issue of this work, will be presented in the section 2.3.

Two different configurations of the k-ε model constants might be used and they are presented in table 2.1. The "standard" engineering constants have been used for numerous flows types. However, for atmospheric flows $C_\mu = 0.033$ is preferred to 0.09 so that μ_t matches its atmospheric surface layer value (the Prandtl number for the turbulent dissipation, σ_ε, is also adjusted on that sense). We will use the "atmospheric flow" configuration, except when it is explicitly mentioned.

2.2.1.2 k-ε-$\overline{v^2}$-f turbulence model

Our calculations were in most of the cases (and when it is not explicitly mentioned) based on the standart RaNS k-ε turbulence model. However, in Chapter 6 we propose a procedure based on the "code friendly" variant of the original k-ε-$\overline{v^2}$-f model of Laurence et al. (2004). Full details on the k-ε-$\overline{v^2}$-f model formulation and its variants can be found in e.g. Durbin (1991) and Laurence et al. (2004).

Complementing the momentum, k and ε equation, the k-ε-$\overline{v^2}$-f model has a transport equation for $\overline{v^2}$, [1]

$$\rho \frac{\partial \overline{v^2}}{\partial t} + \rho \frac{\partial U_j \overline{v^2}}{\partial x_j} = k\overline{f} - 6\overline{v^2}\frac{\varepsilon}{k} + \frac{\partial}{\partial x_j}\left(\frac{\nu_t}{\sigma_k} \frac{\partial \overline{v^2}}{\partial x_j} \right), \tag{2.21}$$

and an elliptic relaxation equation for a function $\overline{f}$,

$$L^2 \nabla^2 \overline{f} - \overline{f} = \frac{C_{f1}}{T}\left(\frac{\overline{v^2}}{k} - \frac{2}{3} \right) - C_{f2}\frac{\mathcal{P}_k}{k} - 5\overline{v^2}\frac{\varepsilon}{k^2}, \tag{2.22}$$

[1] In this model $\overline{v^2}$ can be thought as the ensemble average of the velocity fluctuation normal to the streamlines (not in the x_2 or y direction). Using the previous notation, $\overline{v^2}$ should be represented as $\langle v_\perp'^2 \rangle$. But $\overline{v^2}$ notation, similar to the used by Laurence et al. (2004), is simpler and, as this does not induce erroneous interpretation, we will keep it.

following Laurence et al. (2004). In the "code friendly" version of this model, f (primarily defined by Durbin (1991)) is substituted by $\overline{f}$, defined using

$$f = \overline{f} - 5\varepsilon\frac{\overline{v^2}}{k^2}, \tag{2.23}$$

and neglecting the term

$$5L^2\nabla^2\left(\varepsilon\frac{\overline{v^2}}{k^2}\right). \tag{2.24}$$

The turbulent time and length scales, T and L are defined by

$$T = \frac{k}{\varepsilon} \text{ and } L = C_L\frac{k^{3/2}}{\varepsilon}. \tag{2.25}$$

The turbulent eddy viscosity is defined in this model as

$$\nu_t = C_\mu^*\overline{v^2}\frac{k}{\varepsilon}, \tag{2.26}$$

where C_μ^* is different from C_μ in k-ε model.

For now, equations (2.21) and (2.22) does not present canopy related terms. This subject will be discussed latter, in Chapter 6

2.2.2 Large eddy-simulations

In a very similar way to RaNS, Large Eddy-Simulations decompose the variables in two terms; but in this case we are interested in simulate the larger turbulent flow scales. The variables are filtered in order to calculate the larger scales (captured by the mesh resolution) and the smaller scales of scale smaller than the grid resolution, are treated by a sub-grid scale turbulence model. Formally, one may think of filtering as the convolution of a function with a filtering kernel G. For instance, the filtered x_i-direction velocity vector component u_i may be defined as

$$\overline{u}_i(\boldsymbol{x},t) = \int G(\boldsymbol{x}-\xi)\,u_i(\boldsymbol{x},t)\,d\xi. \tag{2.27}$$

resulting in

$$u_i(\boldsymbol{x},t) = \overline{u}_i(\boldsymbol{x},t) + u_i'(\boldsymbol{x},t). \tag{2.28}$$

The fundamental equations used in the LES are,

$$\frac{\partial\overline{u}_j}{\partial x_j} = 0\ , \tag{2.29}$$

$$\rho\frac{\partial\overline{u}_i}{\partial t} + \rho\frac{\partial\overline{u}_j\overline{u}_i}{\partial x_j} = -\frac{\partial\overline{p}}{\partial x_i} + \frac{\partial}{\partial x_j}\left(\mu\frac{\partial\overline{u}_i}{\partial x_j}\right) - \frac{\partial\tau_{ij}^R}{\partial x_j} + F_i\ , \tag{2.30}$$

where pressure p is decomposed into spatial filtered and residual sub-grid scale parts, $p = \overline{p} + p'$, and with ρ and μ representing density and the dynamic molecular viscosity of air. τ_{ij} is the sub-grid scale stress tensor and F_i is a drag force induced be the presence of the canopy.

The sub-grid stress tensor (or residual stress tensor),

$$\tau_{ij}^R = \rho\overline{u_i u_j} - \rho\overline{u}_i\overline{u}_j, \tag{2.31}$$

was calculated using the dynamic model Germano et al. (1991) with a Lagrangian approach of Meneveau et al. (1996) for averaging along the fluid particle trajectories.

The LES for this work were made using the code developed by Silva Lopes (2000).

2.3 Canopy models

The canopy presence is represented on the RaNS and LES momentum equations as a drag force, thought to reproduce the momentum dissipation that the trees and its foliage should produce in the flow.

In LES, the drag force induced by the forest canopy acting in the x_i-direction, F_i, is given by,

$$F_i = -C_D a(z) \rho \left|\overline{\mathbf{u}}\right| \ \overline{u}_i, \tag{2.32}$$

where C_D is a constant drag coefficient, $a(z)$ is the local foliage density, and $|\overline{\mathbf{u}}|$ is the magnitude of the velocity vector. The drag coefficient value varies between 0.1 and 0.3 for most of the vegetation (Katul et al., 2004); the leaf area density $a(z)$ $(\mathrm{m}^2/\mathrm{m}^3)$ can vary appreciably with z, especially in forested systems.

In RaNS simulations, the drag force is

$$F_i = -C_D a(z) \rho \left|\mathbf{U}\right| U_i. \tag{2.33}$$

The forest canopy presence also has its turbulent mechanisms, as it is discussed by Finnigan (2000). The forest acts on the flow creating near its top a plane mixing layer, slowing down the air among the vegetation. This phenomena and all the complex behaviour of the air around the trees are expected to produce high turbulence levels. However, the canopy is also a turbulence dissipater, mainly for the higher length scales. On that sense, canopy may be regarded as a strong dissipater for the larger turbulent scales as the turbulent eddies are breaked in to small foliage wake eddies that dissipate rapidly. This can be thought as a spectral short-cut of the turbulent energy cascade.

In the RaNS calculations, source/sink terms, S_k and S_ε found in k and ε equations, model the mentioned mechanisms of turbulence production and destruction due to the

canopy foliage. Different authors propose different source/sink terms and in order to put them together we used,

$$S_k = \rho C_z \left(\beta_p |\mathbf{u}|^3 - \beta_d |\mathbf{u}| k\right) , \quad (2.34)$$

$$S_\varepsilon = \rho C_z \left(C_{\varepsilon 4}\beta_p \frac{\varepsilon}{k} |\mathbf{u}|^3 - C_{\varepsilon 5}\beta_d |\mathbf{u}| \varepsilon\right) , \quad (2.35)$$

as in Sanz (2003) and Katul et al. (2004), where $C_z = C_D a(z)$.

At the beginning of this work, it was used a simple canopy model purposed by Svensson and Häggkvist (1990), which only considered the production mechanism (section 4). This corresponds to use the following canopy model constants: $\beta_p = 1.0$, $\beta_d = 0$, $C_{\varepsilon 4} = 1.95$ and $C_{\varepsilon 5} = 0$. Later on, trying to improve our results, other canopy models were tested, involving non zero values for β_d and $C_{\varepsilon 5}$.

2.3.1 Roughness length and zero-displacement model

A classical and simpler approach to simulate forest canopy, described by Raupach (1994) and Verhoef et al. (1997), consists on the use of an exaggerated roughness length z_0 at canopy locations and a zero-plane displacement d of the bottom boundary. Basically, the results are shifted d meters upward along the vertical, as a way to replicate the boundary-layer type of flow above the tree tops. Another possibility is to create a fake elevation on the forested zones, with a transition ramp on the edges, has its is done on WASP software (Mortensen et al., 2004).

This simple method can produce satisfactory results in simple situations, but obviously is unable to resolve the flow within the forest and has serious limitations to reproduce the flow near the edges of the canopy, mainly its turbulent flow complex behaviour. However, in some sections of this work, the models described above were also compared with this simpler approach.

Chapter 3

The Wind Flow over *Serra de Alvoaça*

Abstract

After a field measurements study on the *Serra de Alvoaça* wind farm site, for reasons that could not be explained, the maximum velocity did not occur at the highest elevation. This raised some questions on quality and confidence on the engineering studies based on linear models, and also on the field measurements.

The wind farm would be located at the top of a ridge and, for higher locations, simulations showed that this was due to increased slope of the terrain upstream of that ridge. This higher slope was responsible for a higher slant of the wind vector and a reduced horizontal velocity.

The analysis of the wind flow characteristics at ten locations of the proposed layout showed that no major difficulties should be expected from the operation of the park. Any change (even small) of location, which can occur during the installation phase, should be considered very cautiously. There is the risk of moving the wind turbine into locations of large turbulence intensity and vertical components of wind velocity.

3.1 Introduction

In the present chapter we illustrate the importance of non-linear models to resolve the wind flow over a mountainous region, i.e., the *Alvoaça* wind farm site, in the *Covilhã* borough. We use a difficult engineering application, to explore the capabilities in modelling and estimate the wind conditions (speed and turbulence) in a very complex orography region.

This chapter is also an example of our quest for a methodology and an example of how CFD can be used in wind farm engineering studies. This involves questions on when and at what stage of the study is desirable to use CFD, which variables are most important and how to process the information.

The work present in this chapter follows a series of studies (Silva and Rodrigues, 2005), based on field measurements using cup anemometers, performed since year 2000 at *Serra de Alvoaça*, which led to the decision of building the wind farm–*Parque Eólico de Alvoaça*– by ENERNOVA.

The issue that brought us to this study was that the field measurements were not conclusive, and produced unexpected results that, when applied to WAsP (Mortensen et al., 2004) yield contradictory conclusions, mainly at masts PORT094 and PORT095 (with errors above 25%). Being the mast PORT095 located 335 m above PORT094, it was expected that wind conditions on that spot would be much more favourable for wind energy production, but this was not the case. WAsP could not deal with this issue. The main objective of these calculations was investigate the wind behaviour at those locations, trying to understand those results in all these consequences on the proposed wind farm layout.

A methodology was followed where high resolution sonic anemometer measurements were performed for a period of time long enough to collect data within the most energetic sectors of the wind rose. These measurements were combined with three-dimensional computer flow simulation (VENTOS® solver (Castro and Palma, 2002; Castro et al., 2003, 2004)) to uncover some hidden aspects of the wind flow over *Serra de Alvoaça* that could not be explained by conventional tools alone, i.e., cup anemometer and computer codes based on linear models, like WAsP(Mortensen et al., 2004).

3.2 Case study description

3.2.1 Topography and land cover

The wind farm under study is to be built at *Serra de Alvoaça*, in the Covilhã and Seia boroughs, near the *Serra de Estrela*. A photo and a three-dimensional representation of the site are shown in figures 3.1 and 3.2, where the 13 positions (Table 3.1) under study can be seen from different view angles. Locations PORT094 - *Bulde*, PORT095 - *Fojo* and PORT329 - *Bugalheira* are wind measurement stations, while the remaining spots are the planned layout for the wind farm, according to information provided by ENERNOVA.

The wind farm is located along the top of a ridge with heights above sea level between 975 m and 1310 m. This ridge is almost perpendicular to the direction $330° - 150°$ (being 0°, the "North to South" direction). The terrain around the wind farm site is complex,

Table 3.1: UTM29, ED50, coordinates for the locations under study.

Site	Easting	Northing	altitude
T1	609723	4457557	962
T2	609859	4457741	980
T3	610061	4457851	991
T4	610252	4457942	1019
T5	610464	4458027	1063
T6	610710	4458100	1114
T7	610927	4458181	1131
T8	611135	4458265	1158
T9	611370	4458408	1205
T10	611561	4458526	1214
PORT094-*Bulde*	609343	4456859	975
PORT329-*Fojo*	610858	4458112	1129
PORT095-*Bugalheira*	612234	4458743	1310

Figure 3.1: Alvoaça Wind Farm: photo of the site.

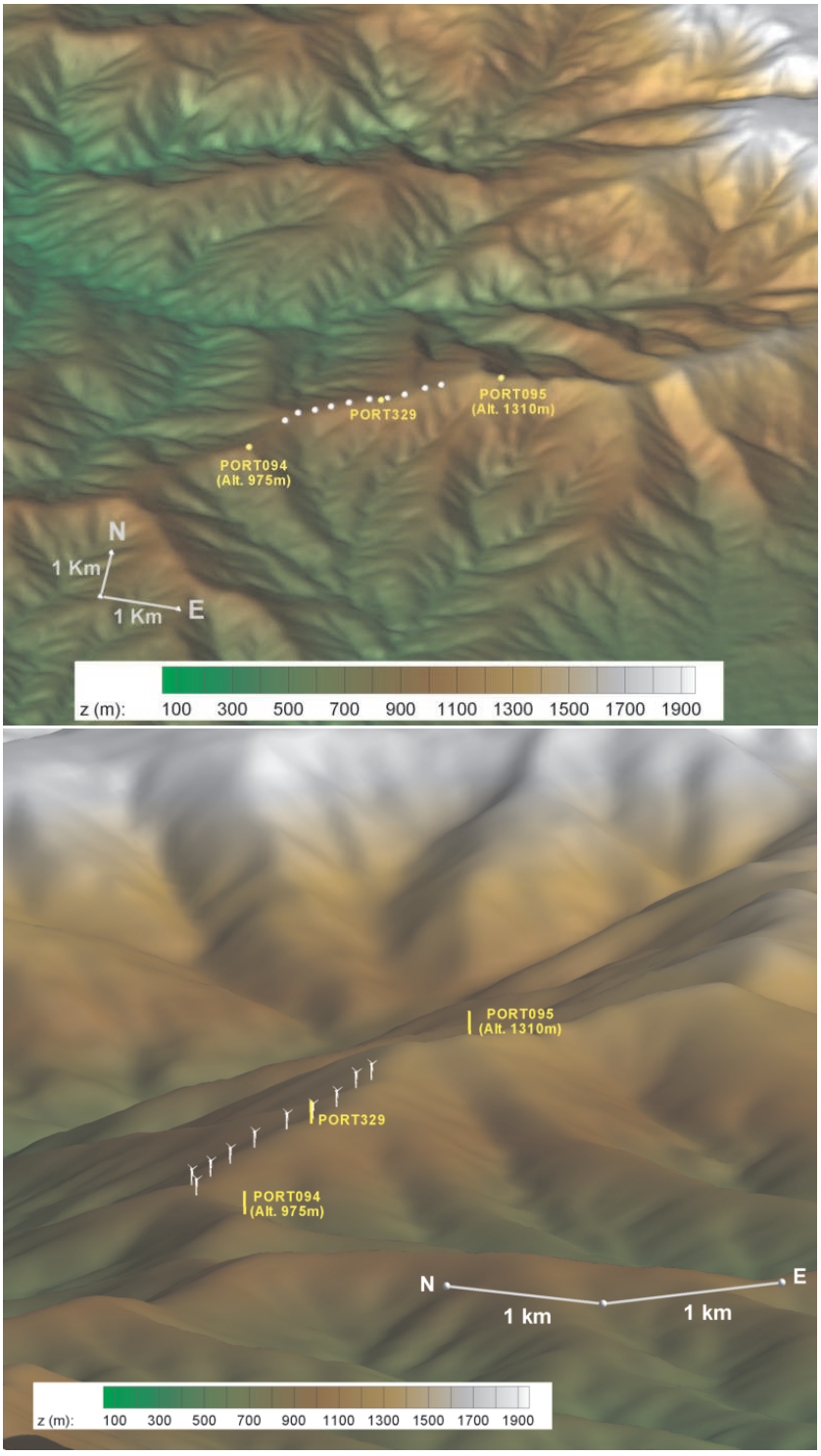

Figure 3.2: Three-dimensional representations of the site.

with highest slopes in the range of 20° to 30°, reaching 40° at north of PORT095. The ground is covered with different type of vegetation, from scarce patches of eucalypti and pine trees in the valley to almost no vegetation (short grass) in the area where the wind farm is being planned.

3.3 Physical and Numerical Parameters used in the Computer Flow Simulations

3.3.1 Wind conditions

Calculations were made based on measured wind conditions presented on the technical report made by INEGI (Silva and Rodrigues, 2005). The mean wind velocity at 60 m above ground level (*agl*) was between 7.0 and 8.0 ms^{-1}, increasing around 0.2 ms^{-1} at 80 m *agl*. It is also said that by far the most important wind directions for wind energy production are those belonging to $0° \pm 15°$, $330° \pm 15°$ and $120° \pm 15°$ directions (figures 3.3 and 3.4).

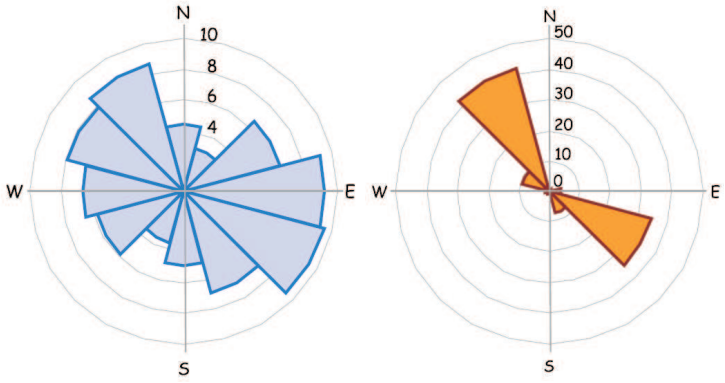

Figure 3.3: Field measurements for wind velocity (in $\mathrm{m\,s}^{-1}$) and energy available (%) per wind rose sector at PORT094.

According to this, we have decided to simulate these three different wind directions: 0°, 330° and 120°. The inlet conditions were tuned in order to obtain wind velocity values between 7.0 and 8.0 $\mathrm{m\,s}^{-1}$ at 60 m *agl*, over the *Alvoaça* park location.

3.3.2 Inlet conditions

The inlet flow consisted of a logarithmic velocity profile below $\delta = 2500$ m, using a roughness length of $z_0 = 0.05$ m and $u^* = 0.4\ \mathrm{m\,s}^{-1}$. This yielded $U_\infty = 10.8\ \mathrm{m\,s}^{-1}$, the

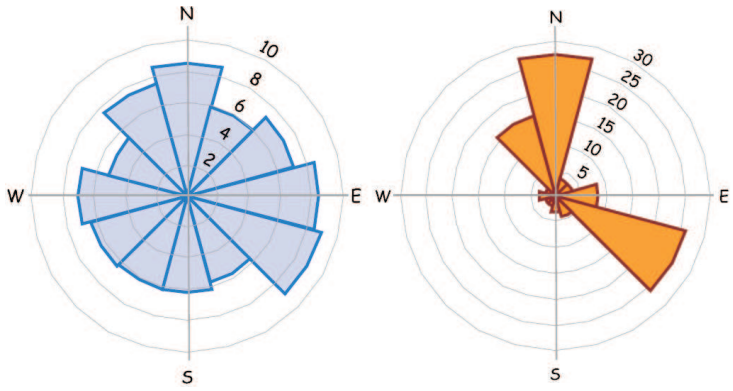

Figure 3.4: Field measurements for wind velocity (in $\mathrm{m\,s^{-1}}$) and energy available (%) per wind rose sector at PORT095.

velocity outside the boundary layer[1]. The inlet conditions were tuned in order to obtain wind velocity values around 9.0 $\mathrm{m\,s^{-1}}$ at 60 m *agl*, over the *Alvoaça* wind farm location.

In order to compare its transient behaviour with the previous results, simulations with twice the velocity magnitude were also tested ($u^* = 0.8\ \mathrm{m\,s^{-1}}$; $U_\infty = 21.6\ \mathrm{m\,s^{-1}}$ for 330º wind direction).

3.3.3 Time dependent formulation

During the first stage of the flow calculations, it was noticed that the solution could not be stationary. The computer code was used in transient formulation (URaNS), with a time step $\Delta t = 1.0$ s.

3.3.4 Numerical mesh

A numerical mesh was used with $82 \times 57 \times 31$ grid nodes covering an area of $11 \times 8 \times 4$ km in the horizontal and vertical directions, respectively. The domain was centred at coordinates $(610700, 445800)$ UTM29. For each case, the numerical grid was rotated to align with the incoming flow, defined by the flow direction at the inlet boundary.

The mesh was refined at the centre of the domain, with $\Delta x = \Delta y = 50$ m. In the vertical direction, control volumes were concentrated near the surface, with $\Delta z = 12.5$ m.

[1]Note that $U = \frac{u^*}{\kappa} \ln\left(\frac{z+z_0}{z_0}\right)$

3.3.5 Computational details

Calculations were made using a Dell Precision™ Workstation 650 based on two Intel® Xeon™ CPU at 2.80 GHz. The calculations reached a periodic state after 80 to 100 hours of computing time, which corresponds to a model time between 4×10^4 s and 5×10^4 s (11 to 14 hours), approximately.

3.3.6 Presentation of results

Results are presented in two sections.

In section 3.4 – Results for Masts and Turbine Layout – all major features that one needs to consider when evaluating a wind farm site are addressed. Turbulence intensity, and both the horizontal and the vertical velocity are shown at mast and turbine locations, as a function of the distance above ground level (time averaged values). This will enable the analysis of the wind behaviour at turbine locations.

Section 3.5 – The Wind in the Vicinity of the Wind Farm – tries to go beyond the initial objective of the present work. Here we present a larger set of results, in a way that can facilitate future analysis by an interested reader and guide the wind farm designers in possible future changes to the proposed layout, in case they are needed in late stages of the project or during the wind farm erection. This will enable the identification of the best places for turbine location and, above all, the identification of those places where turbine siting should not be considered. Comments are scarce and analysis of results is limited, since this section was organised with no specific question in mind.

3.4 Results for Masts and Turbine Layout (0°, 330° and 120° winds)

In this section we present numerical results for the three most energetic wind directions found in the experimental campaign (Silva and Rodrigues, 2005) at the PORT095 measurements station, namely 0°, 120° and 330°.

3.4.1 Wind conditions at PORT094, PORT095 and PORT329

3.4.1.1 Velocity profiles

The information here is restricted to the locations of the masts: PORT095, PORT094 and PORT329. Each of the three figures, 3.5, 3.6 and 3.7, is concerned with one wind direction.

Masts measurement locations above ground level are indicated: 30 m for PORT094 mast, 40 m for PORT095, and 30 m and 60 m for PORT329.

Northerly (0° and 330°) winds

(Figures 3.5 and 3.6)

1. The wind horizontal velocity profile shape above 30 m is nearly uniform for the three masts locations.
2. Vertical component of wind velocity and turbulence intensity are acceptable on masts PORT094 and PORT329. The worst conditions are those associated with PORT095, namely in the case of northerly winds (0°). At this location one can find:
   - the lowest horizontal velocity (V_h can be up to 2 $\mathrm{m\,s^{-1}}$ lower than at PORT094 or PORT329);
   - the highest turbulence intensity (TI). It reaches values above 15%;
   - the highest vertical to horizontal velocity ratio (W/V_h), up to 7× higher than at PORT094.
3. In case of 330° winds, the wind velocity is higher and the turbulence intensity is slightly lower, but the ratio (W/V_h) increases, up to the twice the value of 0° direction.
4. Regarding northerly winds (0°), the location of PORT095 is the least appropriate for wind turbines, due to its higher turbulence intensity and vertical component of wind velocity.

South-easterly (120°) winds

(Figure 3.7)

Wind characteristics did not improve in the case of south-Easterly winds.

1. Wind velocity tends to be lower and its profiles above 30 m *agl* in PORT095 and PORT329 are not as uniform as in case of northerly winds.
2. At PORT094, the ratio between vertical and horizontal velocities reaches almost 15%, but this value still does not exceed the recommended value of about 10° of wind velocity inclination.
3. The levels of turbulence intensity are as high as for northerly winds. Nevertheless, its value is below the recommended limit of 16% for sub-class B wind generators at the turbine axis height (above 60 m).

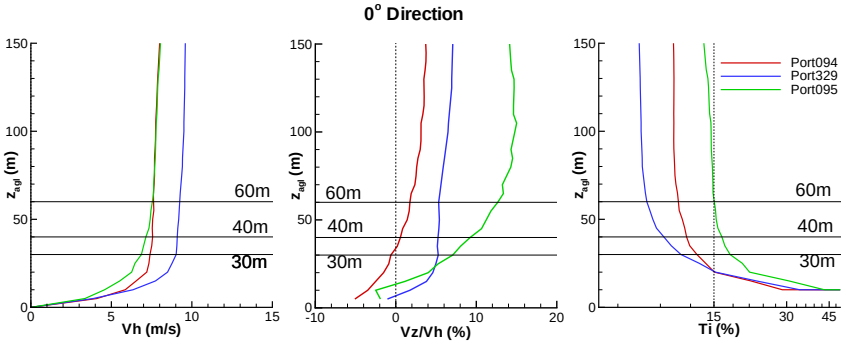

Figure 3.5: Horizontal velocity (V_h), vertical and horizontal velocity ratio (W/V_h) and turbulence intensity (TI) at masts PORT094, 095 and 329, for northerly (0°) wind

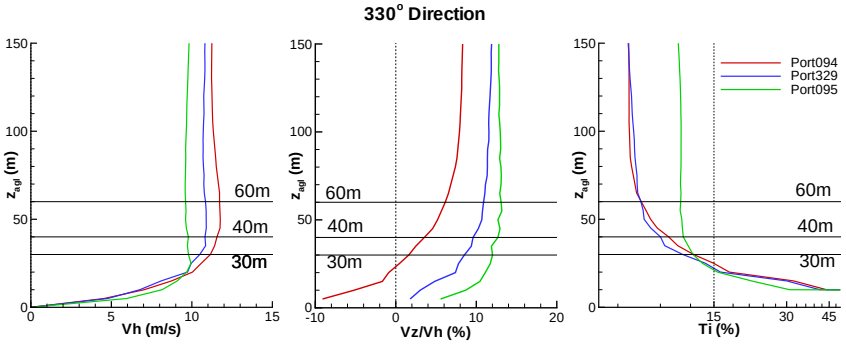

Figure 3.6: Horizontal velocity (V_h), vertical and horizontal velocity ratio (W/V_h) and turbulence intensity (TI) at masts PORT094, 095 and 329, for north-westerly (330°) wind

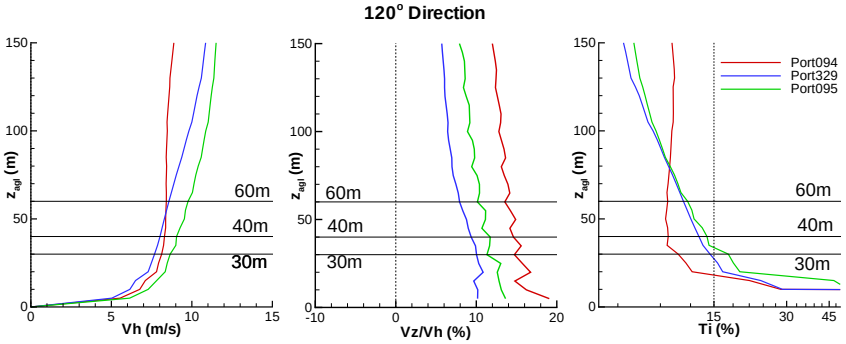

Figure 3.7: Horizontal velocity (V_h), vertical and horizontal velocity ratio (W/V_h) and turbulence intensity (TI) at masts PORT094, 095 and 329, for south-easterly (120°) wind

3.4.1.2 Velocity contours and velocity vectors in North-South longitudinal planes containing PORT094, PORT095 and PORT329

The figures 3.8, 3.9 and 3.10 are plane sections following the 0° wind direction (from North to South), passing through the masts. The colour intensity is associated with the magnitude of the horizontal wind velocity, and the vector length is proportional to the plane projected wind velocity. These figures complement the three previous ones (Figs. 3.5, 3.6 and 3.7). Here one can have a global view of the wind flow pattern in a wider region covering 3.0 km around the meteorological masts.

1. In the lee-side of the mountain, recirculating wakes are generated. Those wakes are not stable, producing turbulence and an unsteady flow, typical of these regions.

2. It is very important to note that the acceptable locations for turbines are very narrow areas at the top of the ridge: any small displacements upwind and the vertical velocity component may become excessive; any small displacements downwind and we may enter a highly turbulent region with separated flow, in the wake of the mountain.

3. As we move towards the top of the mountain (passing each of the three masts, from top to bottom figures), one can see that the terrain becomes increasingly steeper, with inclinations of 13, 19 and reaching a slope of 33° in the case of PORT095 (Fig. 3.10).

4. This increasingly steep slope is the reason for lower horizontal velocities in PORT095 compared to the other locations, in case of northerly winds. At PORT095, the wind reaches the top of the hill with a significant vertical component and, obviously, once the wind momentum is directed into the vertical direction, its horizontal component is reduced.

3.4.2 Wind conditions at turbine locations

A preliminary turbine layout was proposed, as described in subsection 3.2.1. The turbines are numbered from T1 to T10, starting from the lower height of the ridge (near mast PORT094), climbing up towards mast PORT095.

Figures 3.11, 3.12 and 3.13 show the vertical profiles of the three major variables ($V_h, W/V_h$ and TI) for all 10 turbine locations, respectively for winds blowing at 0°, 330° and 120°. The information here is analogous to that in figures 3.5, 3.6 and 3.7, though focused on the turbine locations. Here it becomes obvious that south-easterly (120°) winds are the most demanding in terms of wind turbine operation: the profiles are less uniform compared with 0° and 330° winds, and the turbulence intensity is close to 15% for lower distances above ground level.

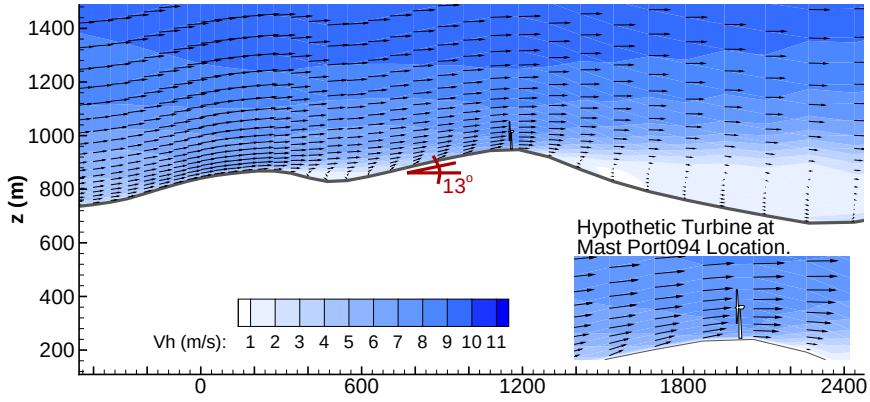

Figure 3.8: Velocity vectors and horizontal velocity contours in a longitudinal plane on the 0° direction, through PORT094.

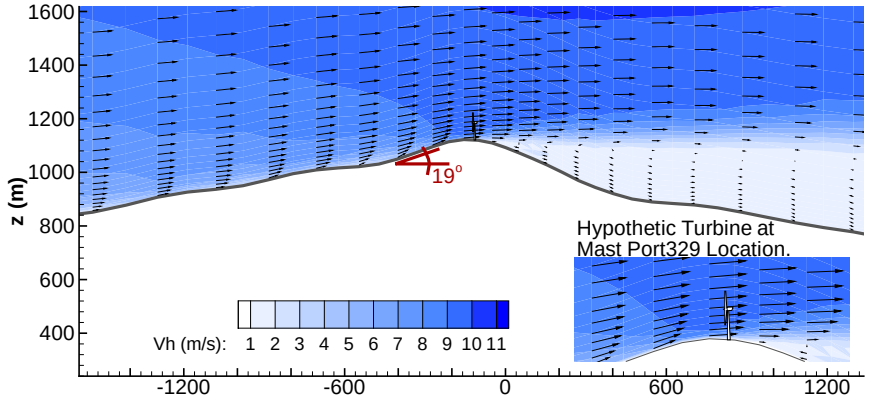

Figure 3.9: Velocity vectors and horizontal velocity contours in a longitudinal plane on the 0° direction, through PORT0329.

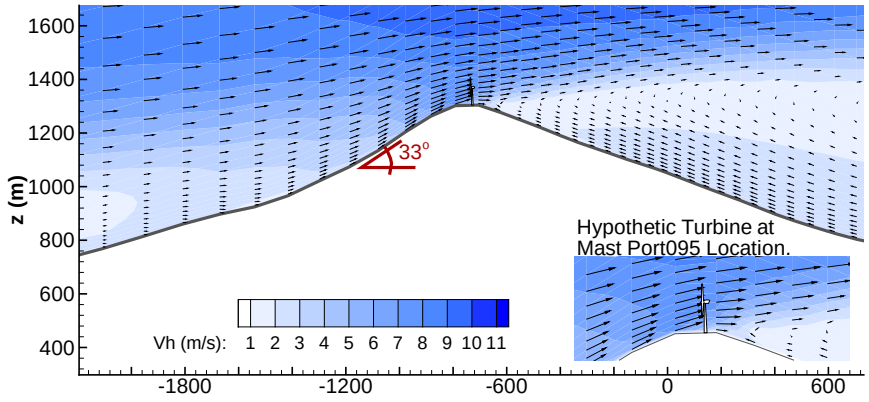

Figure 3.10: Velocity vectors and horizontal velocity contours in a longitudinal plane on the 0° direction, through PORT095.

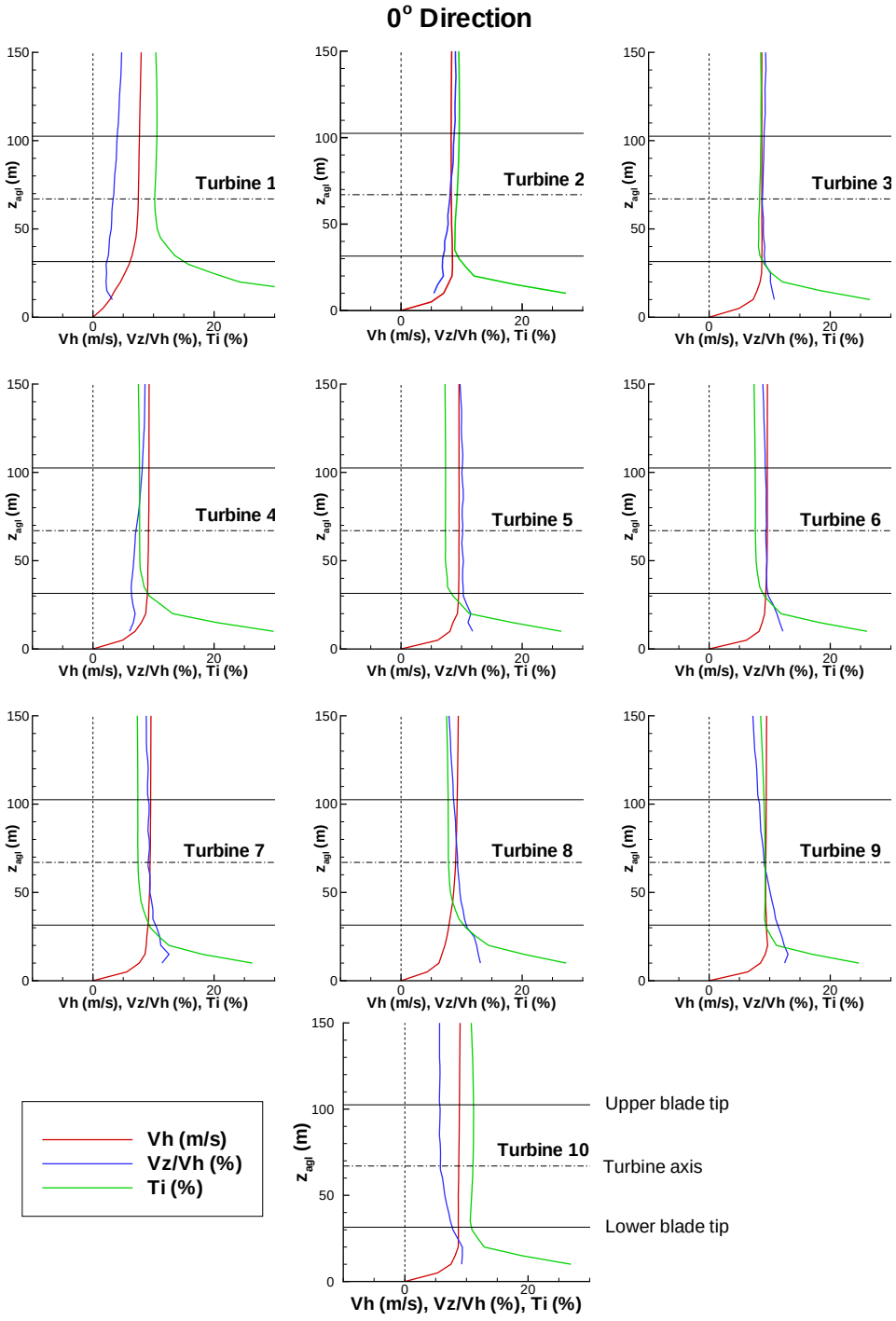

Figure 3.11: Horizontal velocity, vertical to horizontal velocity ratio and turbulence intensity at turbine coordinates, in case of northerly (0°) wind. Time averaged results using a time interval of 5600 s.

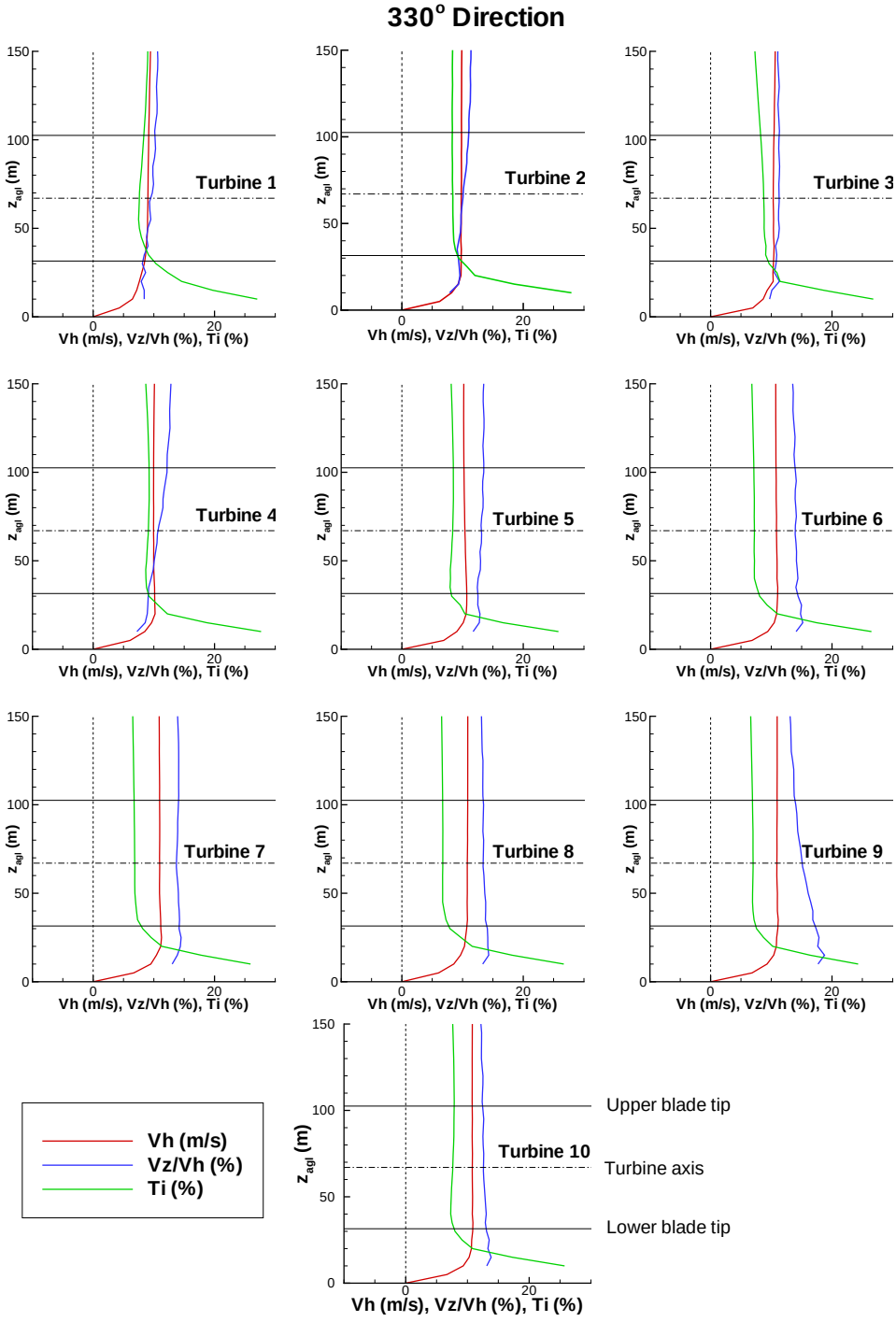

Figure 3.12: Horizontal velocity, vertical to horizontal velocity ratio and turbulence intensity at turbine coordinates, in case of north-westerly (330°) wind. Time averaged results using a time interval of 5600 s.

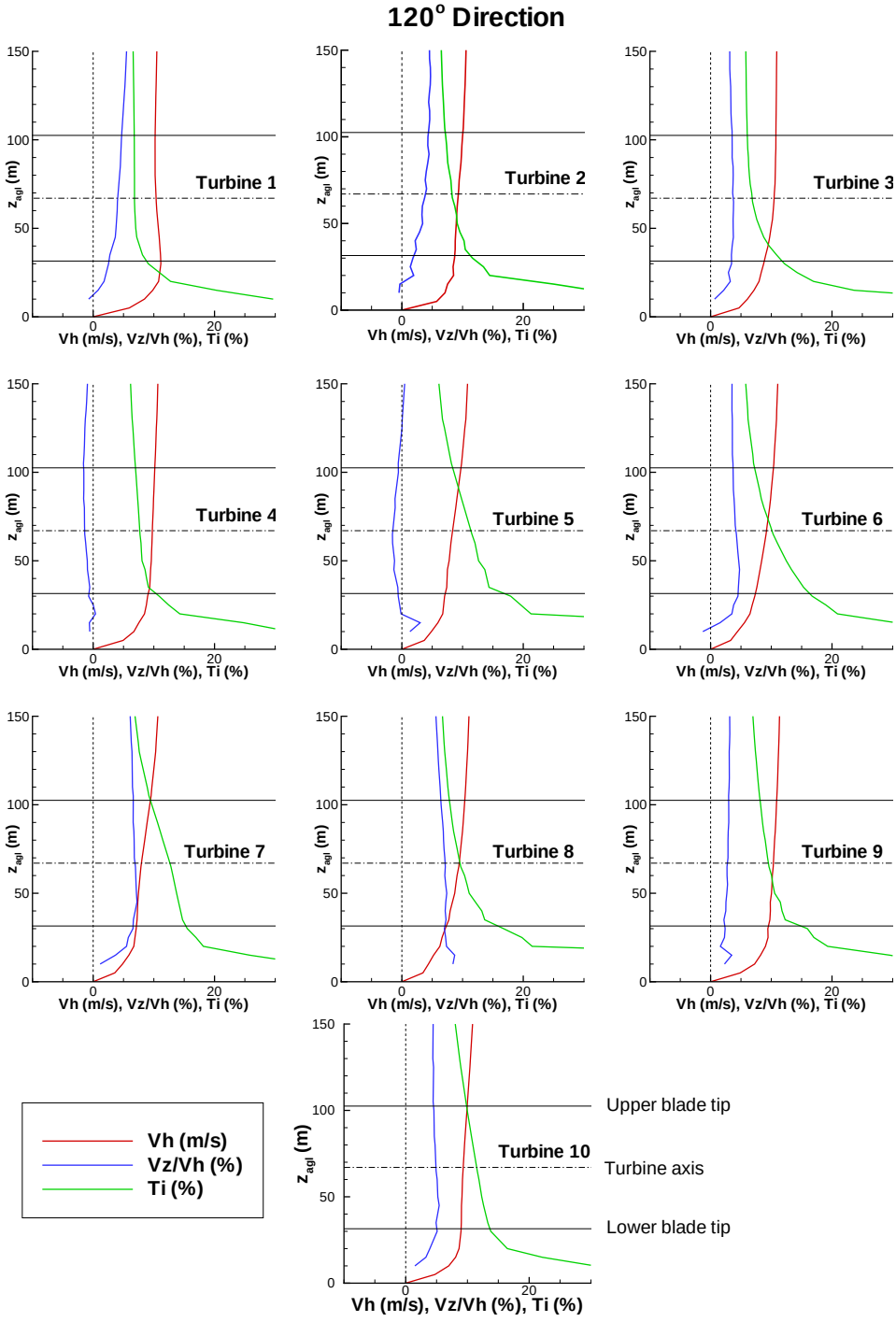

Figure 3.13: Horizontal velocity, vertical to horizontal velocity ratio and turbulence intensity at turbine coordinates, in case of south-easterly (120°) wind. Time averaged results using a time interval of 5600 s.

The quantitative information for all 10 turbines at a reference distance of 67 m *agl* and the 3 meteorological masts is included in Table 3.2, with comments on page 29.

Table 3.2: Horizontal velocity (V_h), vertical to horizontal velocity ratio (W/V_h) and turbulent intensity (TI) at 67 m *agl* for the turbine locations under study for the three incoming flow directions. Time averaged results using a time interval of 5600 s.

site	0° Northerly			330° North-westerly			120° South-easterly		
	V_h [ms^{-1}]	W/V_h [%]	TI [%]	V_h [ms^{-1}]	W/V_h [%]	TI [%]	V_h [ms^{-1}]	W/V_h [%]	TI [%]
Turbine T1	7.5	3.3	10.2	9.0	9.5	7.6	10.4	4.1	6.8
Turbine T2	8.3	8.1	9.2	9.8	10.1	8.4	9.4	3.9	8.3
Turbine T3	8.7	8.8	8.3	10.3	11.2	8.7	10.5	3.7	6.8
Turbine T4	9.2	7.1	7.7	10.0	10.7	9.1	9.7	−1.4	7.7
Turbine T5	9.6	10.1	7.3	10.4	13.1	8.4	8.4	−1.5	11.4
Turbine T6	9.6	9.4	7.6	10.9	13.9	7.2	9.2	4.2	10.1
Turbine T7	9.4	9.1	7.4	11.0	13.7	6.9	8.0	6.9	12.6
Turbine T8	9.0	9.3	7.8	10.8	13.4	6.7	9.4	7.1	9.6
Turbine T9	9.3	9.1	9.2	10.9	15.1	7.0	10.3	2.8	9.5
Turbine T10	8.7	5.8	11.0	10.8	12.6	7.6	9.3	4.9	11.5
PORT094 (30 m *agl*)	3.5	−0.6	12.8	11.1	1.5	12.4	8.1	14.8	10.7
PORT329 (30 m *agl*)	9.0	5.3	10.9	10.4	8.5	11.2	7.7	10.0	14.5
PORT329 (60 m *agl*)	9.2	5.3	7.9	10.8	10.9	7.5	8.6	7.9	11.2
PORT095 (40 m *agl*)	7.1	9.2	16.2	9.8	12.7	11.2	9.1	11.7	14.0
				Sonic anemometer measurements					
PORT329 (30 m *agl*)							7.18	−5.2	9.8
PORT329 (60 m *agl*)	9.36	−5.5	4.7	7.75	−4.5	6.2			

1. The 330° case is the one that yields the higher horizontal velocities, followed by the 0° and the 120° cases.

2. For northerly winds (0°), the most favourable locations tend to be those in the middle (T4, T5, T6 and T7); as one goes towards the edges of the layout, the horizontal velocity decreases and turbulence becomes higher. For north-westerly winds (330°), this contrast between central turbines and those on the edges is smaller, mainly for the turbulence intensity values.

3. In the case of south-easterly winds, the situation is the reverse of the northerly winds case. Positions T4, T5, T6 and T7 are the ones with lower wind speed and higher turbulence intensity.

4. Northerly winds produce high vertical velocity components, namely for direction (330°), perpendicular to the ridge. In this case, W/V_h is always higher than 10%, with the Turbine 1 (T1) exception. On the contrary, the 120° direction produces low vertical velocity components, expecialy at the centre of the farm locations (T4 and T5).

5. None of the cases studied here evidences turbulence intensities above 15% at turbine axis height, and therefore there are no reasons for concern.

The results of field measurements, at the bottom of the table 3.2, show the following:

- The velocity vector points downwards (negative W/V_h), opposed to the computational results that point upwards. These differences should not be emphasised too much, because of the very low values of about 5%, i.e. 3° or a vertical velocity of about 0.5 $\mathrm{m\,s^{-1}}$ only.

  Both the field measurements and the computational results show a vertical component of a magnitude that is much lower that design values and there is no reason for concern in terms of the wind turbine operation.

- In the case of northerly and north-westerly winds, the turbulence intensity predicted by the computer simulations exceeds the measured values by a factor of 1.7 (7.9 against 4.7).

- In the case of south-easterly winds, sonic measurements and computational results are closer to each other and differ by a factor of 1.5 (14.5 against 9.8).

Both the measurements and the computational results show that northerly winds present the most favourable conditions, as shown already when analysing the computational results alone.

The modelling and determination of the turbulence variables (turbulence intensity) is a whole area of active research. Many turbulence models are available beyond the one ($k - \varepsilon$) used here. The turbulence intensity predicted by the computer model can be taken only as indicative. The good news is that neither the measured (sonic) nor the computational values exceed the 16% turbulence intensity, considered as the threshold for selection between sub-class A and sub-class B wind turbines, set by the IEC 61400-1 (IEC, 1999). This is another indication of the appropriateness of the wind farm layout.

3.5 The Wind in the Vicinity of the Wind Farm (0°, 330° and 120° winds)

In this section, the results of wind behaviour around the wind farm are presented. Here we observe the wind transient behaviour around *Serra de Alvoaça*, and at masts and turbines locations. Time averaged wind conditions at turbine axis height are also shown.

3.5.1 Unsteady features of the wind flow (Velocity contours)

Previous studies have shown that terrain induced flow instabilities may preclude the convergence of computer flow simulations based on steady state formulation of the fluid flow equations (Castro et al., 2003). This was found to be the case also of the present wind flow simulations around *Serra de Alvoaça*. In this section we try to convey the transient nature of the wind flow.

Figure 3.14 shows a sequence of plots of the horizontal velocity at 67 m *agl*, in the case of 330° wind calculations, within a time window equal to 25 min and with steps of 5 min. The vectors indicate the local wind direction.

The wake of the ridge is the most unsteady zone. Here, we can find low velocities (blue contours) and vortices, whose intensity grows with altitude and proximity to the mountain summit. Upstream of the ridge, in the valley (top of the figures), we can also observe some unsteadiness, produced by the mountains located upstream, i.e. NW.

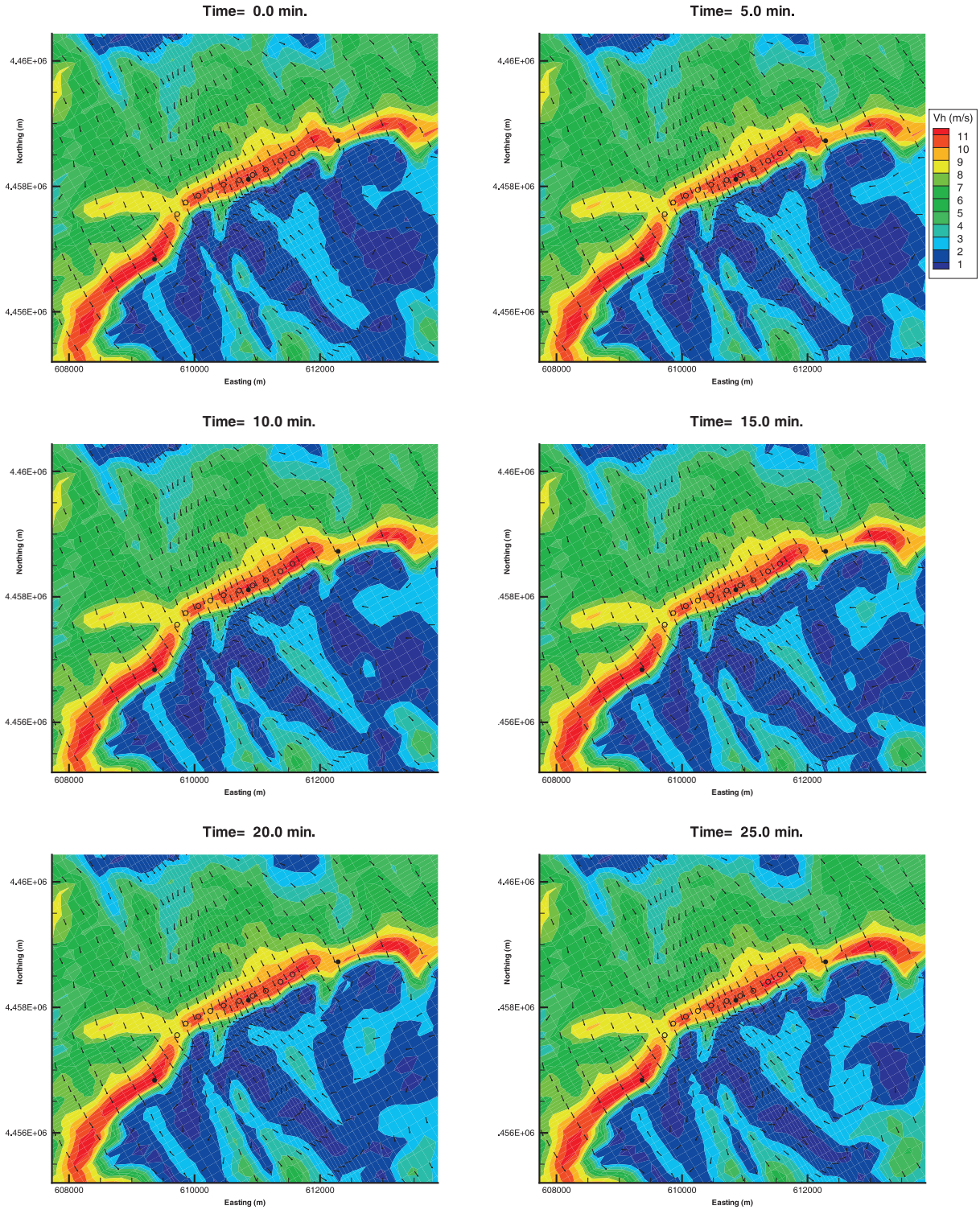

Figure 3.14: Time sequence of horizontal velocity at 67 m *agl* - 330° direction.

3.5.2 Unsteady features of the wind flow (Time series)

Flow unsteadiness at the turbine level can be best seen as time series, as shown in figures 3.15 for the horizontal velocity (V_h) for the thirteen sites (listed in Table 3.1). In all the cases (0°, 120° and 330°), the flow presented an almost periodic behaviour, with the longer time scales in the order of tenths of minutes.

1. The largest amplitudes were found for the 0° incoming flow.

   The results for 330° showed lower amplitudes, which were even lower (the lowest) in the case of 120° winds.

2. It is important to note that the highest locations (turbine T10 and mast PORT095) have higher oscillation amplitudes than the rest.

3. The larger amplitudes found in the 0° and 330° directions are associated with a large recirculation region placed very near in the downstream side of the wind farm, as showed in the following section.

Velocity conditions of twice the magnitude were also tested for 330° wind direction and its transient behaviour compared in figure 3.16. We found the same unsteady phenomena, amplified in amplitude and frequency by a factor of 2.

As can be seen from simple observation of the time series, and confirmed by spectral analysis, the main period of the time series is of the order of 20 to 40 minutes.

Because at turbine location there is no sign of flow separation (reversed wind direction), neither from the computational results nor the sonic measurements, and the wind velocity amplitude is relatively low (about 10% maximum) these features do not affect the decisions made concerning turbine siting.

The results shown here can be useful for the turbine manufacturer when assessing the stress and vibrational loads of a given wind turbine and setting the operating conditions for a particular site. The power spectrum in figure 3.17 is an example of the type of information that can be extracted from the simulated time series.

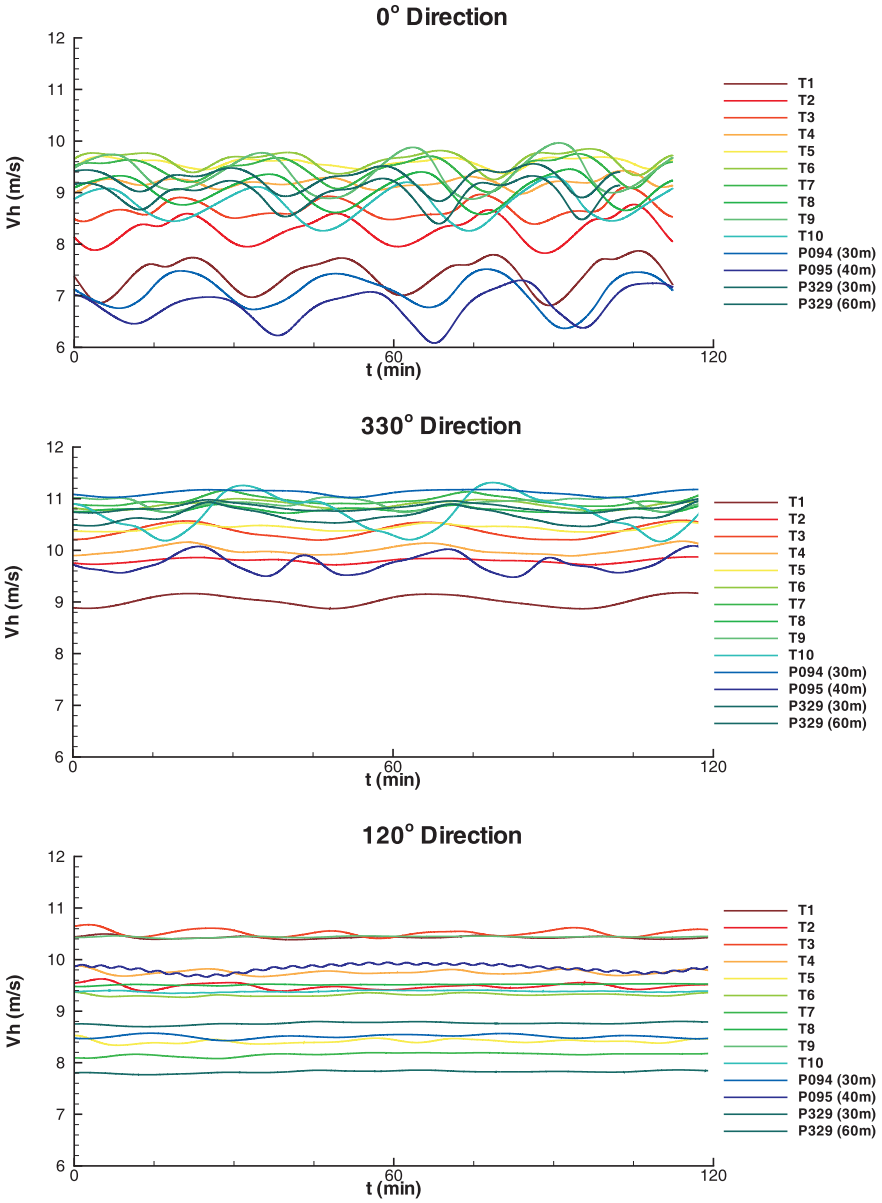

Figure 3.15: Time series for the horizontal velocity.

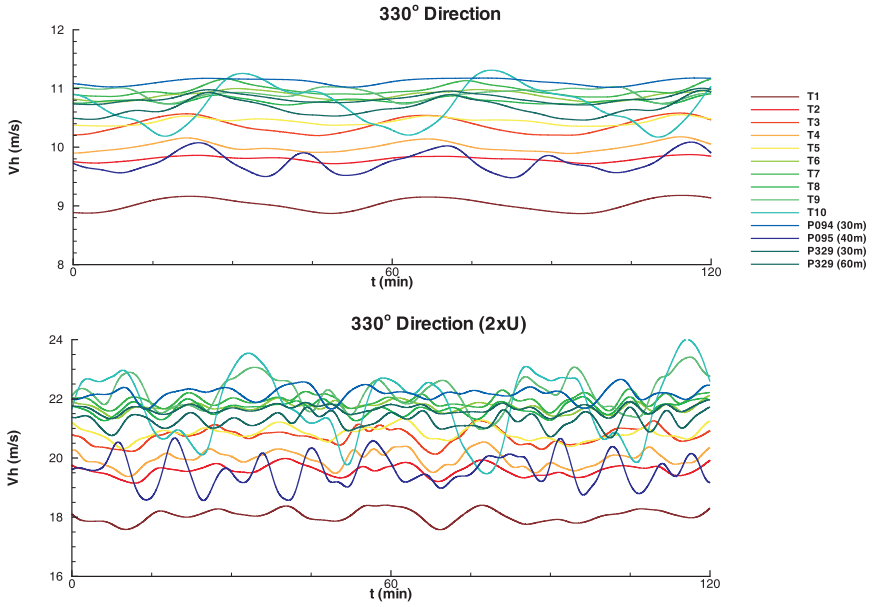

Figure 3.16: Time series for the horizontal velocity, for 330° direction, with $U_\infty = 10.8$ ms^{-1} and $U_\infty = 21.6$ ms^{-1}.

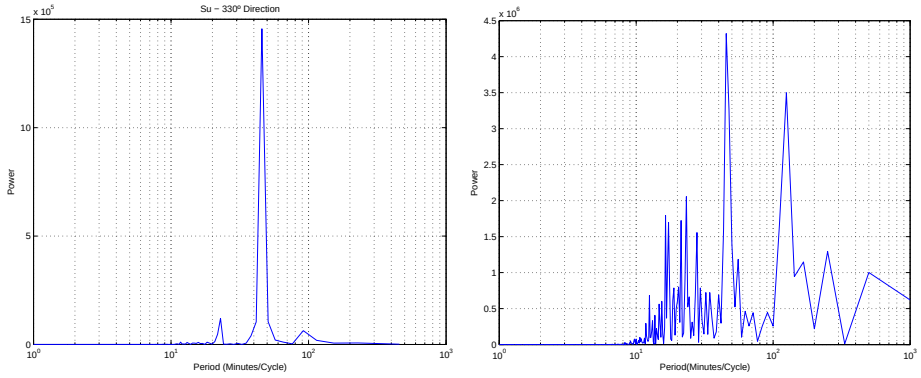

Figure 3.17: Power spectral density at PORT329, 30 m *agl*, for 330° direction, with $U_\infty = 10.8$ ms^{-1} and $U_\infty = 21.6$ ms^{-1}.

Table 3.3: Wind horizontal velocity transient characteristics.

0º Direction (Northerly)

		Max (V_h) m/s	Mean (V_h) m/s	Min (V_h) m/s	Amplitude % Up	Amplitude % Down
PORT329	60 m *agl*	13.4	13.0	12.4	3.1	−4.5
	30 m *agl*	12.9	12.4	11.7	3.8	−6.1
PORT094	30 m *agl*	9.9	9.4	8.6	4.6	−8.4
PORT095	40 m *agl*	10.3	9.6	8.6	7.7	−10.4

330º Direction (North-easterly)

		Max (V_h) m/s	Mean (V_h) m/s	Min (V_h) m/s	Amplitude % Up	Amplitude % Down
PORT329	60 m *agl*	15.5	15.3	15.1	1.7	−1.1
	30 m *agl*	15.5	15.0	14.7	3.2	−2.3
PORT094	30 m *agl*	15.7	15.6	15.4	0.7	−1.2
PORT095	40 m *agl*	14.0	13.4	12.7	4.6	−5.2

120º Direction (South-easterly)

		Max (V_h) m/s	Mean (V_h) m/s	Min (V_h) m/s	Amplitude % Up	Amplitude % Down
PORT329	60 m *agl*	12.2	12.2	12.1	0.5	−0.8
	30 m *agl*	10.4	10.3	10.3	0.5	−0.8
PORT094	30 m *agl*	12.1	12.0	11.9	0.7	−1.2
PORT095	40 m *agl*	13.5	13.4	13.2	0.7	−1.9

330º Direction (North-westerly) - $2 \times U_\infty$

		Max (V_h) m/s	Mean (V_h) m/s	Min (V_h) m/s	Amplitude % Up	Amplitude % Down
PORT329	60 m *agl*	31.5	30.6	29.9	2.9	−2.3
	30 m *agl*	31.6	30.0	28.7	5.2	−4.4
PORT094	30 m *agl*	32.0	31.1	30.2	3.1	−2.7
PORT095	40 m *agl*	30.0	27.0	25.0	11.1	−7.4

3.5.3 Wind conditions contours at 67 m *agl*

Figures 3.18 to 3.23 display contours of horizontal wind velocity, specific wind power ($\mathcal{P}$), vertical velocity component (W), turbulence intensity (TI) and shear factors (α) in horizontal planes comprising the length of the blades above and below the turbine axis. To aid visualisation, wind vectors (not scaled to wind speed) are also shown.

Please note that these figures are time averaged results, and cannot be compared in a point by point basis with figures 3.14.

Northerly wind (0°)
(Figures 3.18 and 3.19)

1. From the first two plots of figures 3.18, one notices that, for given conditions, the proposed layout can hardly be improved. With the exception of turbine T1, where the horizontal velocity falls below 8.0 $\mathrm{m\,s^{-1}}$, the turbines are arranged clearly within the highest wind power area. The same can be said concerning turbulence intensity, with a layout ideally framed inside the zone with the lowest turbulence intensity.

   One remark may be made: this wind farm is placed along a very sharpened mountain ridge; any displacement perpendicular to its line may produce dramatic changes in the local wind behaviour. This is very noticeable on the vertical velocity component graph (in the Fig. 3.18 bottom). The farm location is practically in the limits of a narrow zone of low vertical component.

2. As we can see in the turbulence intensity graph, downstream of the farm, but in its close vicinity, there is a turbulent wake. Here, the main part of the unsteady behaviour of the flow takes place. Obviously, in those locations the wind conditions are unsuitable for wind energy conversion.

3. As discussed previously, the horizontal velocity is nearly uniform at turbine heights, which is desirable. The shear factors graphs (figure 3.19) confirm that at turbine locations, either for the lower blade tip (between 31.5 and 65 m *agl*) or for the upper blade tip (between 65 and 102.5 m), are very acceptable.

North-westerly wind (330°)
(Figures 3.20 and 3.21)

1. The 330° wind direction is nearly perpendicular to the *Serra de Alvoaça* ridge. These are the conditions under which the higher velocities occur. For this direction, the previously defined layout match one of the best locations, as we have concluded in the case of 0° winds (in page 38). Nevertheless, higher velocity locations could be found either side along the ridge, outside the farm. It is also noticed that the highest turbine locations have higher wind velocities (T6 to T10 have horizontal velocities of 11 $\mathrm{m\,s^{-1}}$ - see also Table 3.2).
2. As discussed for 0° direction, the vertical velocity graph shows that turbine locations are in the narrow region of acceptable wind conditions.
3. As in the case of 0° direction, the turbulence intensity inside the wind farm corridor is within acceptable values, but it rises steeply inside the wake zone immediately downstream of the ridge.
4. The shear factors around turbine locations are within standard design values.

South-Easterly wind (120°)
(Figures 3.22 and 3.23)

1. If one observes the upstream topography for the 120° winds, one notices that they should pass over several other ridges before they reach the summit. By contrary, northerly and north-westerly winds cross a large open space (valley) before they reach the farm location.
2. In the case of 120° winds, it is very noticeable that the farm is located in the wake of other mountain ridges. The wind velocity upstream of the farm is not very uniform, and obviously, the turbulence intensity is higher than in the previous cases (we can observe it also on the vertical profile graphs 3.13). Nevertheless, those values do not compromise the farm location. The layout is still within a high horizontal velocity zone and the turbulence intensity is lower than 15% at turbine axis height.
3. It is also remarkable that, for this direction, the vertical velocity component is the lowest for the turbine locations. Finally, the shear factors are also acceptable for this direction.

3.6 Conclusions

The *Alvoaça* wind farm is located along a mountain ridge. As a consequence, the wind characteristics change dramatically from the windward to the leeward side of the ridge.

This terrain complexity is responsible also for a non-stationary wind behaviour, which affects mostly the flow in the lee-side of the mountain.

CFD code predicted worse wind conditions (i.e. lower wind speed and higher turbulence intensity) at the highest mast (PORT095) than those obtained for the one located at the bottom of the farm location (PORT094). These results agreed with the field measurements, contrary to the results obtained with linear models (WAsP code). The current results also showed that the larger slope of the terrain upstream of PORT095 deflects the wind vertically, with a consequent reduction of the horizontal wind velocity. It can also be concluded that at higher locations, outside the farm area, the wind conditions are unsteady and with high turbulence intensity, which makes them less suitable for turbines siting.

Turbine locations are planned along a narrow corridor, where the wind conditions are the best in terms of wind speed, and do not suffer from high turbulence or wind shear. Nevertheless, relatively high wind vertical components are expected for northerly and northwesterly winds, but not reaching unacceptable values.

Finally, we must remark that, especially for northerly winds, the surrounding topography induced transient wind conditions, with fluctuations of a low frequency (periods of 20 to 30 minutes), which are not expected to cause any major problems to the turbines.

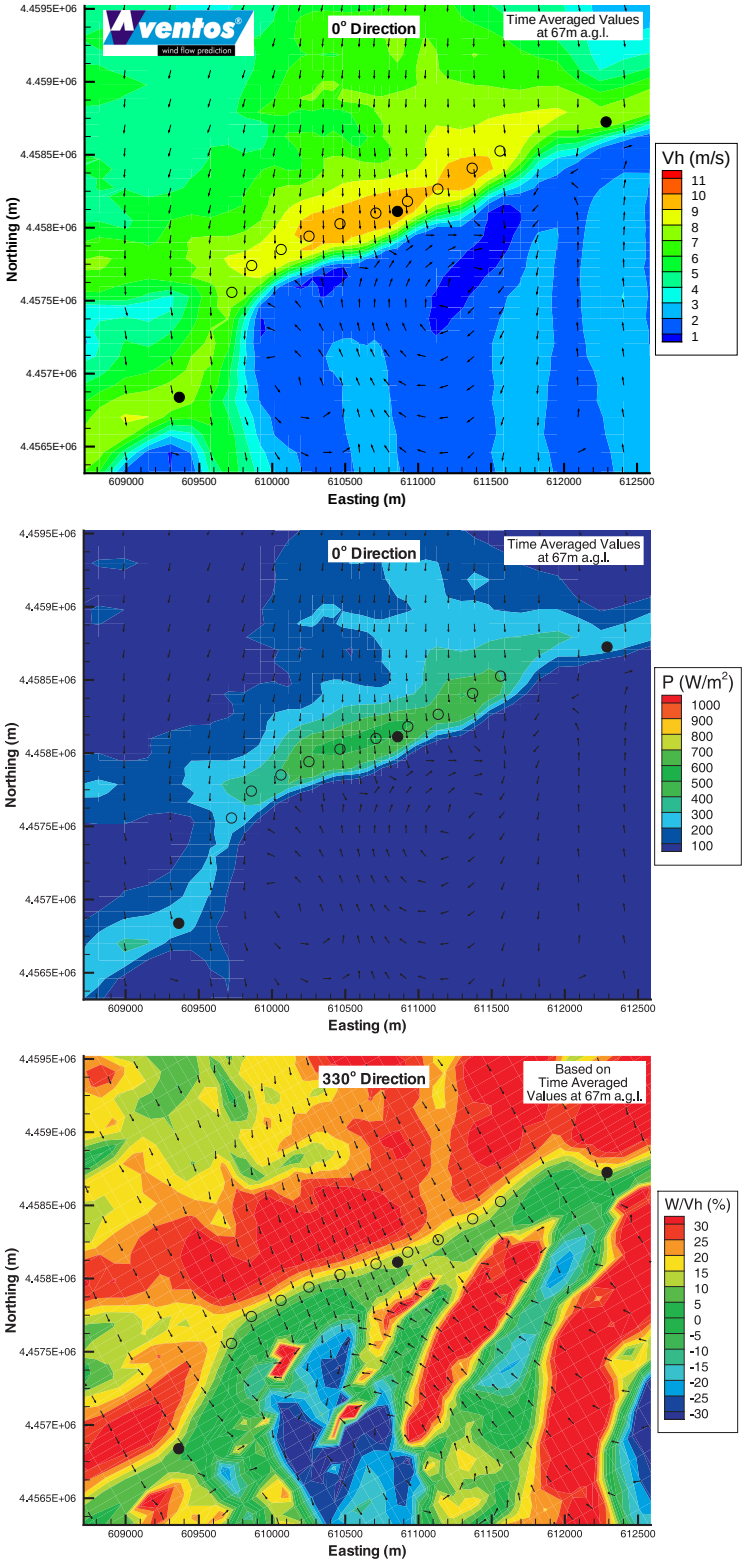

Figure 3.18: Horizontal wind velocity, specific wind power and ratio between vertical and horizontal component of wind velocity - 0° direction.

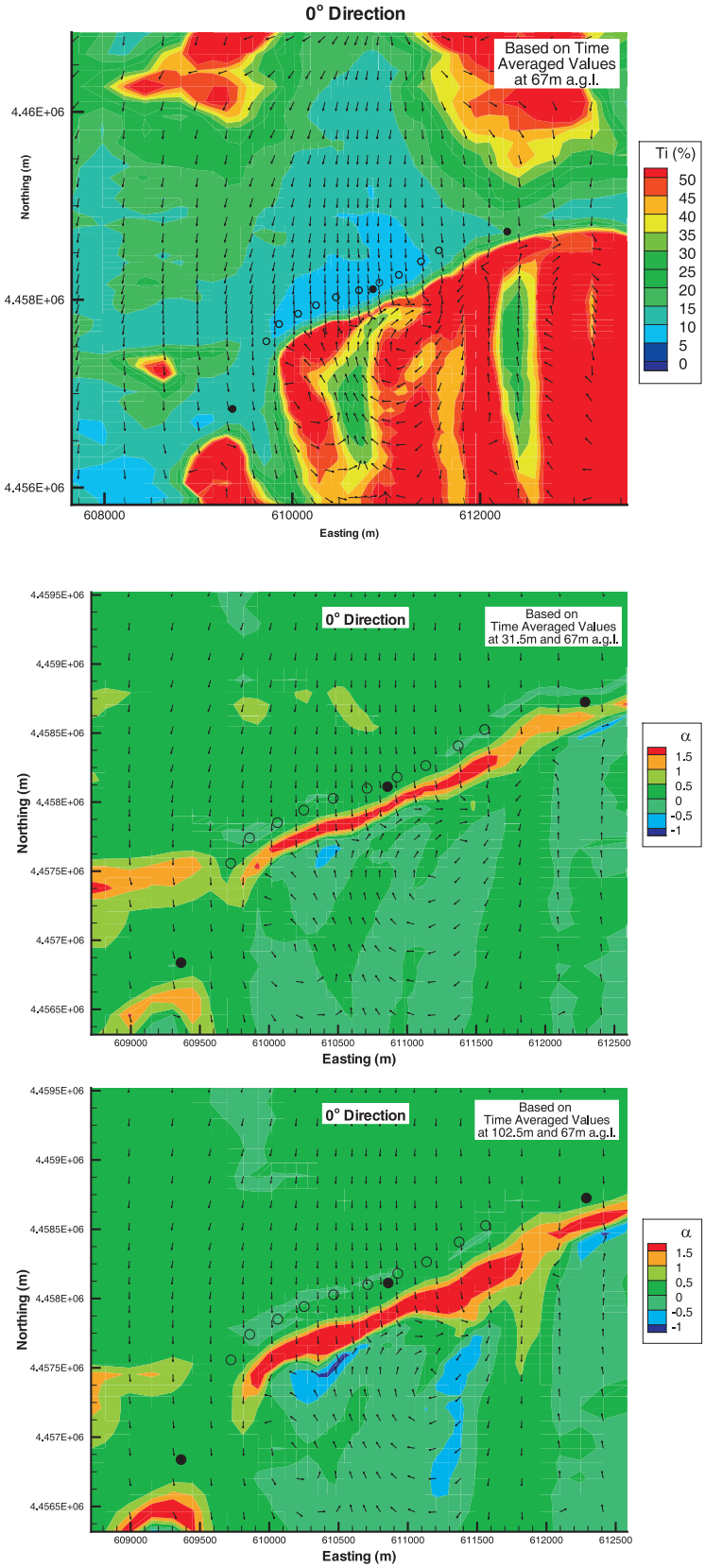

Figure 3.19: Turbulent intensity and shear factor - 0° direction.

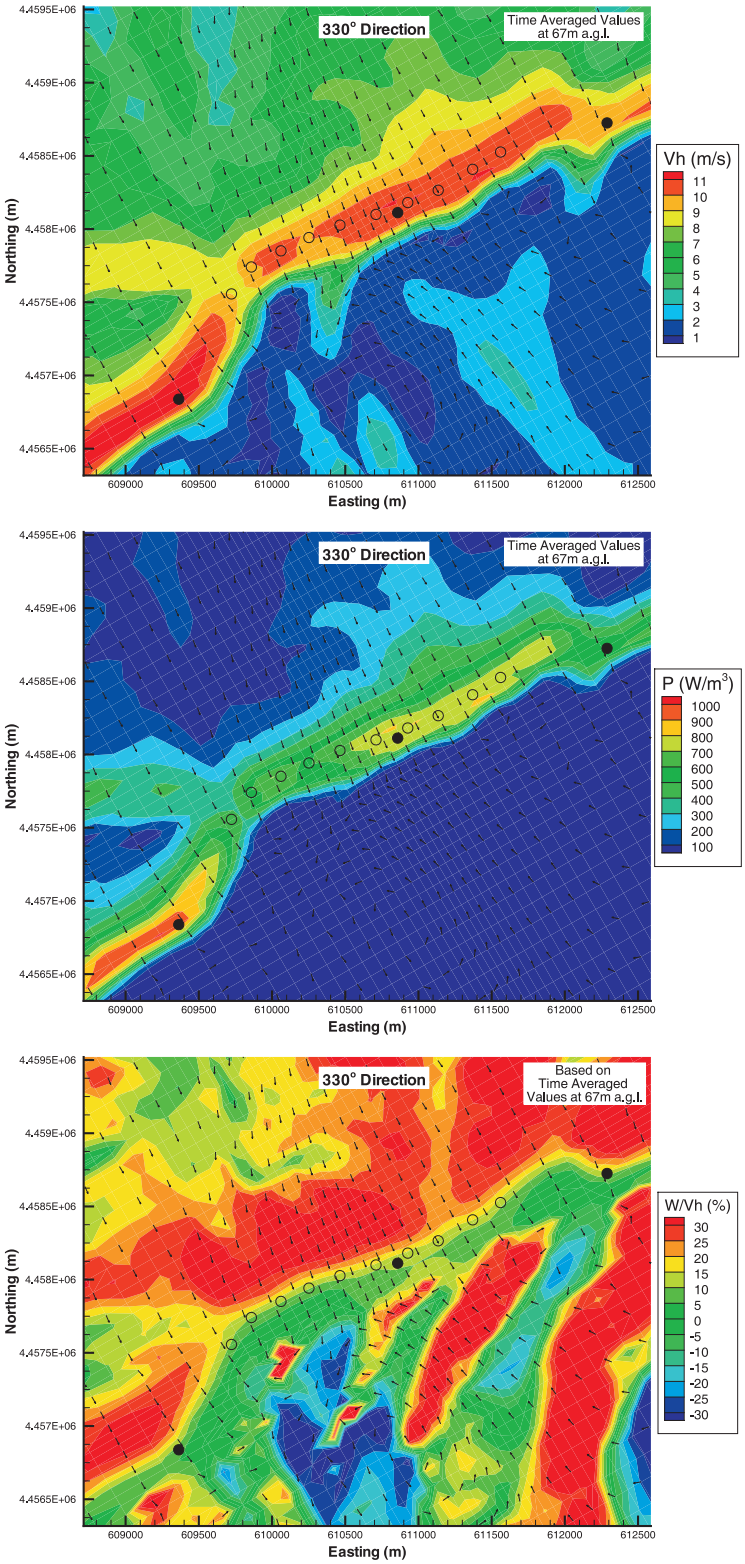

Figure 3.20: Horizontal wind velocity, specific wind power and ratio between vertical and horizontal component of wind velocity - 330° direction.

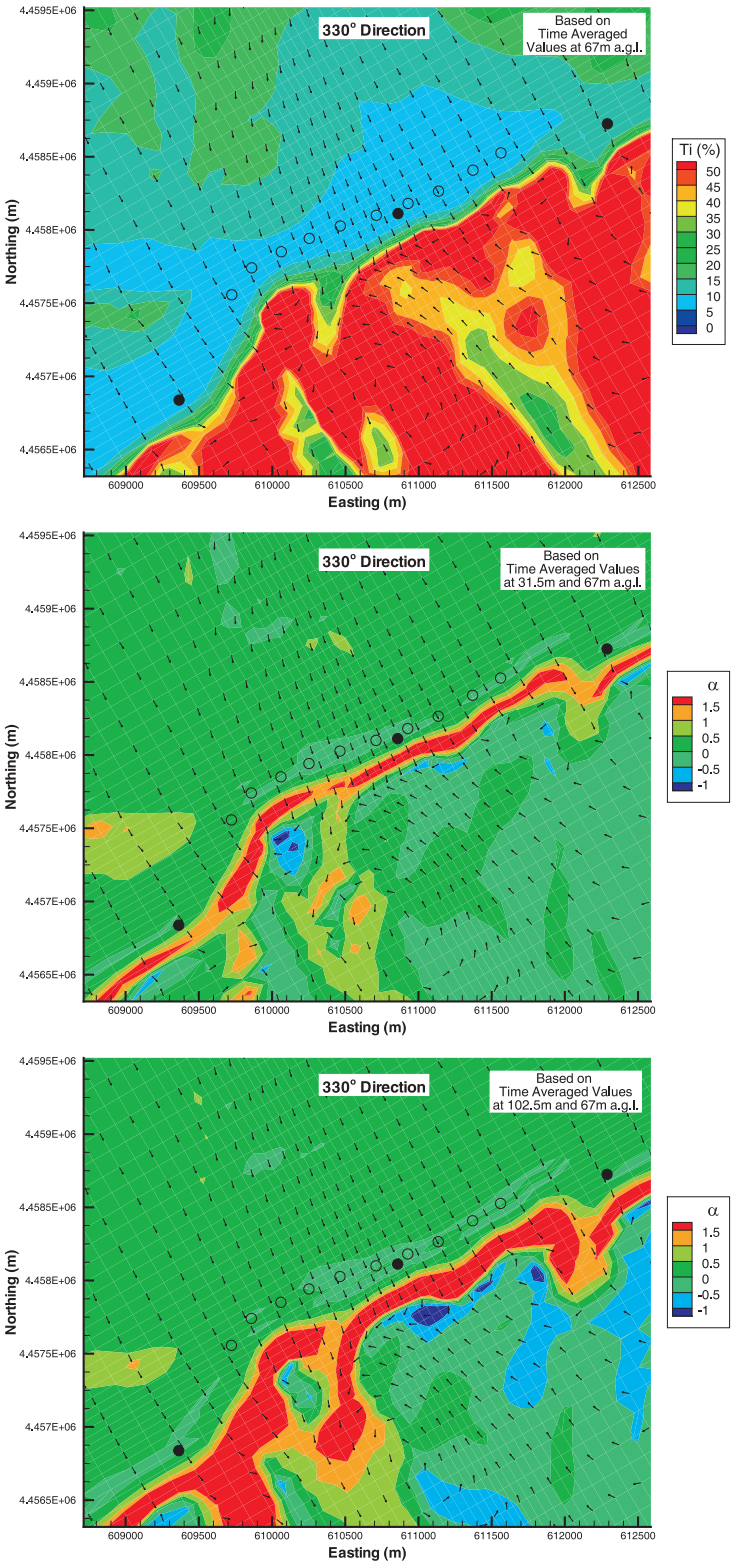

Figure 3.21: Turbulent intensity and shear factor - 330° direction.

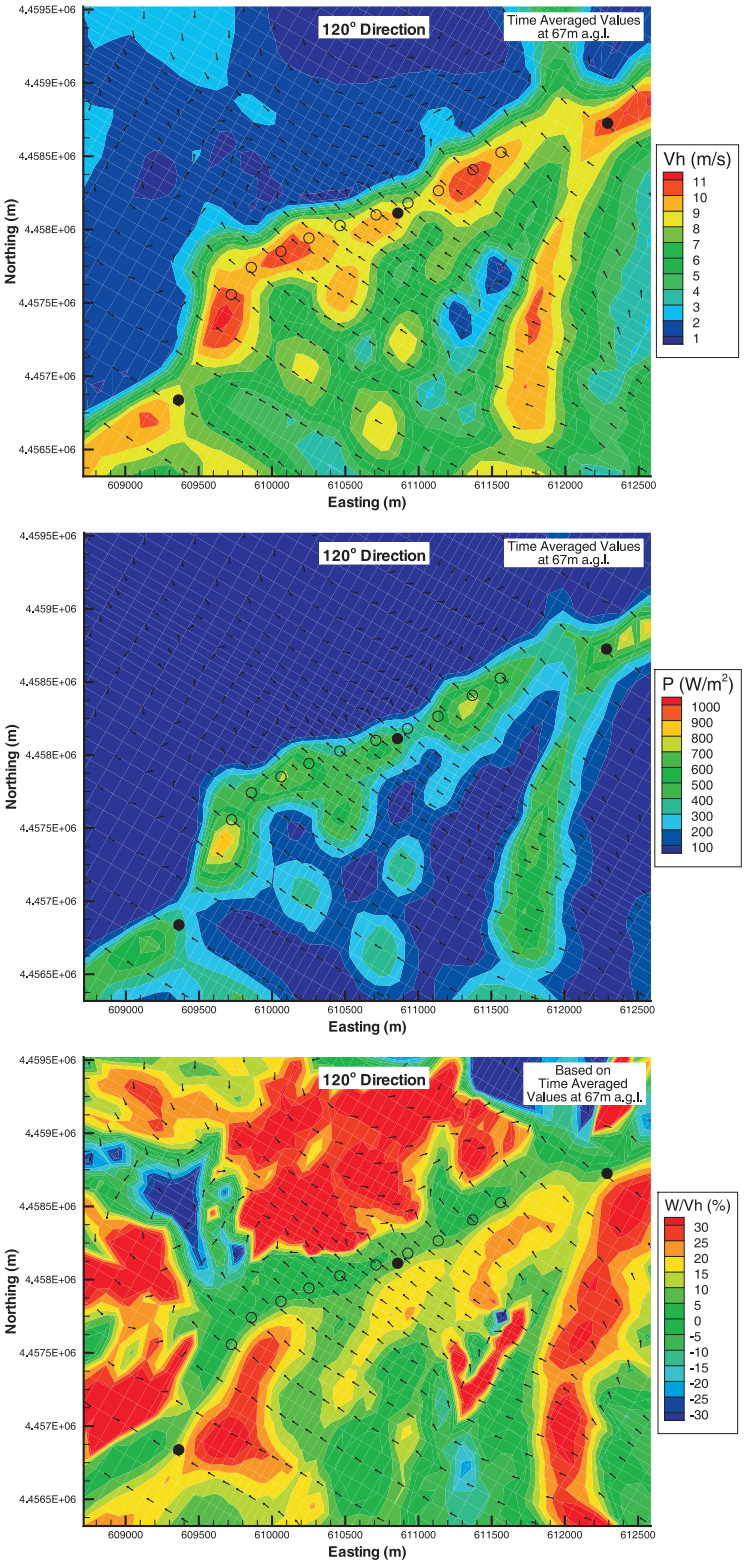

Figure 3.22: Horizontal wind velocity, specific wind power and ratio between vertical and horizontal component of wind velocity - 120° direction.

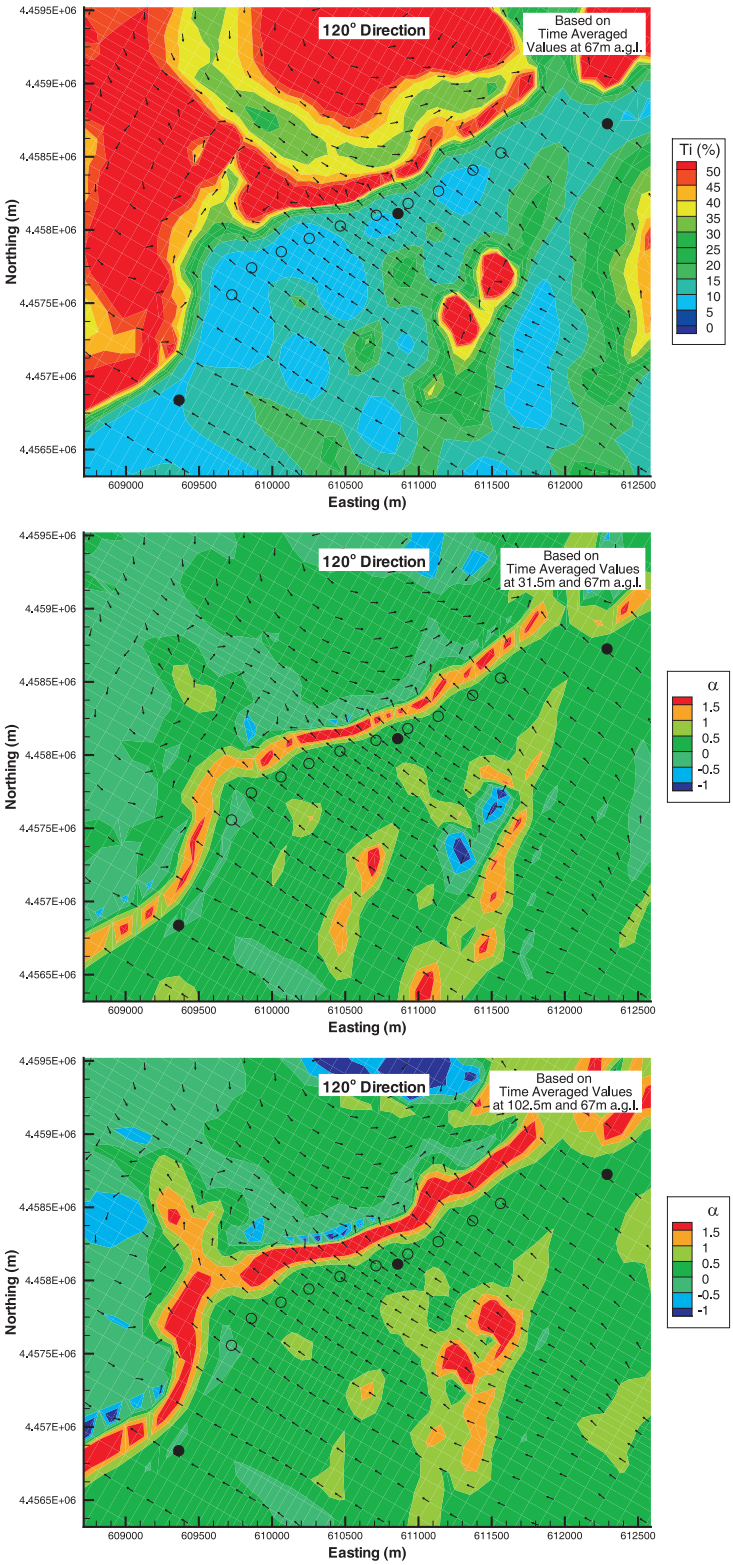

Figure 3.23: Turbulent intensity and shear factor - 120° direction.

Chapter 4

The Wind Flow over Forested Regions (Scottish and French Cases)

Abstract

Measured wind data at two potential wind farm sites, in Scotland and in France, were used for appraisal of a computer model of the wind flow over forested regions, where the trees are mimicked by momentum sinks. The results of the Scottish case were an improvement over previous computer simulations without the canopy model, and showed the difficulties of comparing detailed three-dimensional computer simulations with field data point measurements. In case of the French site, agreement was excellent between mean velocity field measurements at 7 heights above the ground, between 40 and 100 m, and computer results. It was found that the presence of the canopy could increase the turbulence levels by almost two orders of magnitude, when compared to the results obtained without the canopy.

4.1 Introduction

The presence of trees can affect the wind flow in a region to an extent that can make it unsuitable for a wind farm, and in the past forested areas were simply ruled out as candidates for wind energy production. However, the expansion of the wind energy production and the shortage of sites without topographical obstacles, has forced engineers to consider the possibility of installing wind farms in the vicinity of forests, adding an additional value to the land with a minor impact on the surrounding environment.

The very beginning of this work was a wind farm location study, initiated at RES (Renewable Energy Systems Ltd. - UK). Initially, that was a benchmark study (Stuart,

2003) on the prediction capabilities of the non-linear model VENTOS® and the linear model MS3DJH (Walmsley et al., 1982), applied to the wind flow over a potential wind farm site, in Scotland. The level of agreement between field data and the computational results was higher in case of VENTOS®, particularly when there was a region of separated flow between hills. However, for some other wind directions, it was found some discrepancies between field data and computer results; those discrepancies were attributed to the presence of the forest patches in the vicinity of the masts, which the computer model could not take into account. This work was then induced by a wind energy engineering need on having computation numerical tools for simulate wind flow among forested regions.

As a immediate approach to study this problem, a simple canopy model Svensson and Häggkvist (1990) was implemented in VENTOS® code.

Later on, the same code was tested to simulate the wind flow over a potential wind farm site in France, also purposed by RES. This site, located on a very complex orography vicinity, was completely surrounded by extensive forested areas. For this location, we disposed a more complete field data measurements that allowed us, not only to compare wind velocity vertical profiles, but also the wind turbulent effects induced by the forest canopy.

This chapter is based on the published article Lopes da Costa et al. (2006).

4.2 Scottish Case

4.2.1 Case Study Description

This location is a moderately complex terrain site, mainly farmland, with isolated forest patches (mainly Sitka spruce) and small hills, around 300 m height (figure 4.1 and 4.2). Meteorological masts were installed to measure wind speed and direction at 5 locations (M080, M081, M082, M083 and M101), 47 m above ground level (agl), except in case of M080, which was at 40 m agl.

For data analysis, we used the speed-up parameter defined by,

$$S(i,\theta) = \frac{V_h(i,\theta)}{V_{h_{Ref}}(\theta)}, \tag{4.1}$$

where $V_h(i,\theta)$ is the horizontal velocity at mast location i and $V_{h_{Ref}}(\theta)$ is the reference horizontal velocity at reference mast M081, both functions of the wind flow direction θ. Because the reference velocity is not free of the effects of the canopy, the speed-up definition (4.1) is not the best parameter for comparing results of calculations with and without the canopy model, as will be shown later in the text. However, based strictly on the experimental data, there was no better alternative, because there were no masts away from the forested regions for all wind directions.

Figure 4.1: Scottish case: photo of the location.

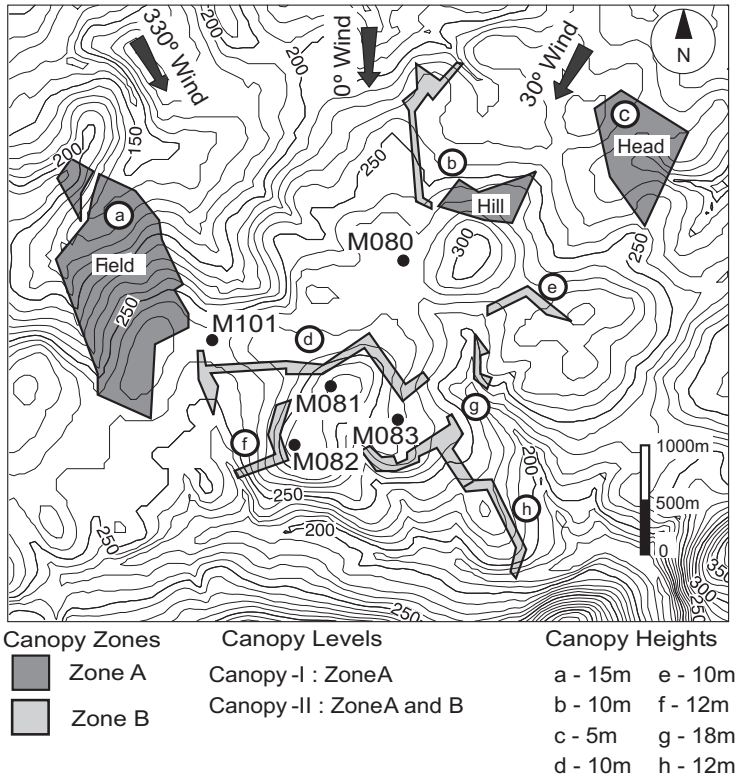

Figure 4.2: Scottish case: Topography, mast locations and canopy zones considered in calculations (contour heights at every 10 m).

Table 4.1: Numerical meshes and flow conditions

Mesh	Grid nodes	Grid nodes NI×NJ×NK	Δz_{min}	Δx_{min} or Δy_{min}
1×	136 059	$77 \times 57 \times 31$	0.60	50.0
2×	268 593	$97 \times 71 \times 39$	0.45	40.0
4×	538 020	$122 \times 90 \times 49$	0.45	32.0
6×	815 360	$140 \times 104 \times 56$	0.45	27.5

4.2.2 Numerical Implementation

Calculations were all performed on an integration domain of 11000 m × 8000 m, centred on the M081 station (figure 4.2), and extended to an altitude of 2000 m. The canopy model we used was the proposed by Svensson and Häggkvist (1990), applying the following canopy model constants: $\beta_p = 1.0$, $\beta_d = 0$, $C_{\varepsilon 4} = 1.95$ and $C_{\varepsilon 5} = 0$ (see section 2.3). The drag coefficient was $C_D = 0.25$ and it was adopted an uniform leaf area density $a = 0.125$ m^{2}m^{-3} (Finnigan, 2000), with a tree height h as in figure 4.2. This canopy model acts in the domain on discrete volumes, corresponding to forest patches and tree windbreaks locations. The inlet flow was a logarithmic wind profile with $u_* = 0.4$ ms^{-1} and a characteristic roughness length of 0.03 m. The inlet boundary layer height was $\delta =$ 150 m. Calculations without the canopy model were also made, considering a characteristic roughness length of 0.03 m over the whole domain. The shadow effect of the masts over the anemometers was removed using the empirical corrections as in Saba (2002).

Later on, several calculations were made, with increasing mesh density (see table 4.1), for -90º, -60º and -30º winds. Three numerical meshes (2, 4 and 6×) with two, four and six times more grid nodes than the reference calculation were used; the number of nodes in each direction was increased by factors of $\sqrt[3]{2}$, $\sqrt[3]{4}$ and $\sqrt[3]{6}$, respectively.

4.2.3 Results

In his benchmark study, Stuart (2003) performed a large set of computer simulations without canopy model for wind directions covering the whole wind rose in small increments of 1º. The agreement with measurements was good, except when the masts were downstream of forest patches, mostly for winds between 270º and 60º. In the current study, we performed one single calculation for each 30º sector, centred in the 270º, 300º, 330º, 0º, 30º and 60º directions. This is different from the experimental speed-up, which is an average of all wind directions within each 30º sector; however, re-analysis of the field data restricted to 5º sectors showed that this had no consequences.

The terrain around the five meteorological masts (figure 4.2) is covered with a few tree patches and wind breaks, and it was not obvious whether some of them could be neglected. In a first attempt (canopy-I), only *Field*, *Head* and the forest area near *Hill* were considered. These were also the three major areas covered with trees, most likely to influence the wind speed on masts and directions mentioned above. Later, a more detailed level of canopy representation was tested (canopy-II), including the thin wind breaks near the masts.

The effects of the canopy over the region are presented in figure 4.3 for the -60º (or 300º) wind, at a constant distance of 47 m from the ground, at which most of the anemometers have been placed. Comparing this with figure 4.2, we can see the limitations of the numerical grid to replicate the exact shape of the tree patches, in particular the thin fences. Each tree patch develops a momentum wake, which, though depending mainly on the shape of the associated tree patch, is also a function of the terrain shape, the upstream flow and the nearby wakes.

The wake caused by the trees in *Field* can be seen as made up of almost two independent wakes, because of its advanced north-west edge. Two spots of lower wind speed (higher deficit of about 40%) occur: first at the top north and within the tree region (A1), and a second spot (A2), further south, outside the tree region and around the mast M101. We also note the following features: the thin region B1 of undisturbed wind crossing almost the whole width of *Field* and close to A1; a second region (B2) of low deficit, located above the wind break "d" (in figure 4.2); and a third region (B3), also of low deficit, which appears downstream of wind break "f", around mast M082. The effect of wind break "f" at this distance from the ground (47 m) seems to accelerate the wind flow in front (region C) and most surprisingly, it leads to the low deficit region downstream denoted B3. The high deficit region downstream of "f" that could be associated with this wind break, is shifted towards the south, most likely as a consequence of the orography and the following wind break "h". Though being complex, because this is a plane view at one single distance to the ground it is still a limited view of the whole complexity of the wind flow over the region, and a good example of how unrealistic the computer simulation of the wind flow over real forests can be, if based in simpler models.

Figure 4.4 shows the experimental speed-up at 4 masts, and the computational results under three different conditions: no canopy, canopy-I and canopy-II. Considering first the ability of the computational model without canopy model to mimic the experimental field data, we can see that the computer results exceeded the field data by a maximum of 14% (at mast M080 for wind directions between 0º and 60º). Because the larger discrepancies occurred at masts M080 and M101, this is most likely a consequence of their proximity to forests, respectively at *Hill* and *Field* (figure 4.2). See, for instance that at M101, the over-prediction of the speed-up parameter occurred for directions -90, -60 and -30 (270, 300 and 330), i.e. when the wind blows over the *Field* forest before reaching mast M101 (cf. figure 4.3). The objective was to improve the agreement between field data and computational results, via a more accurate physical modelling, namely taking into account

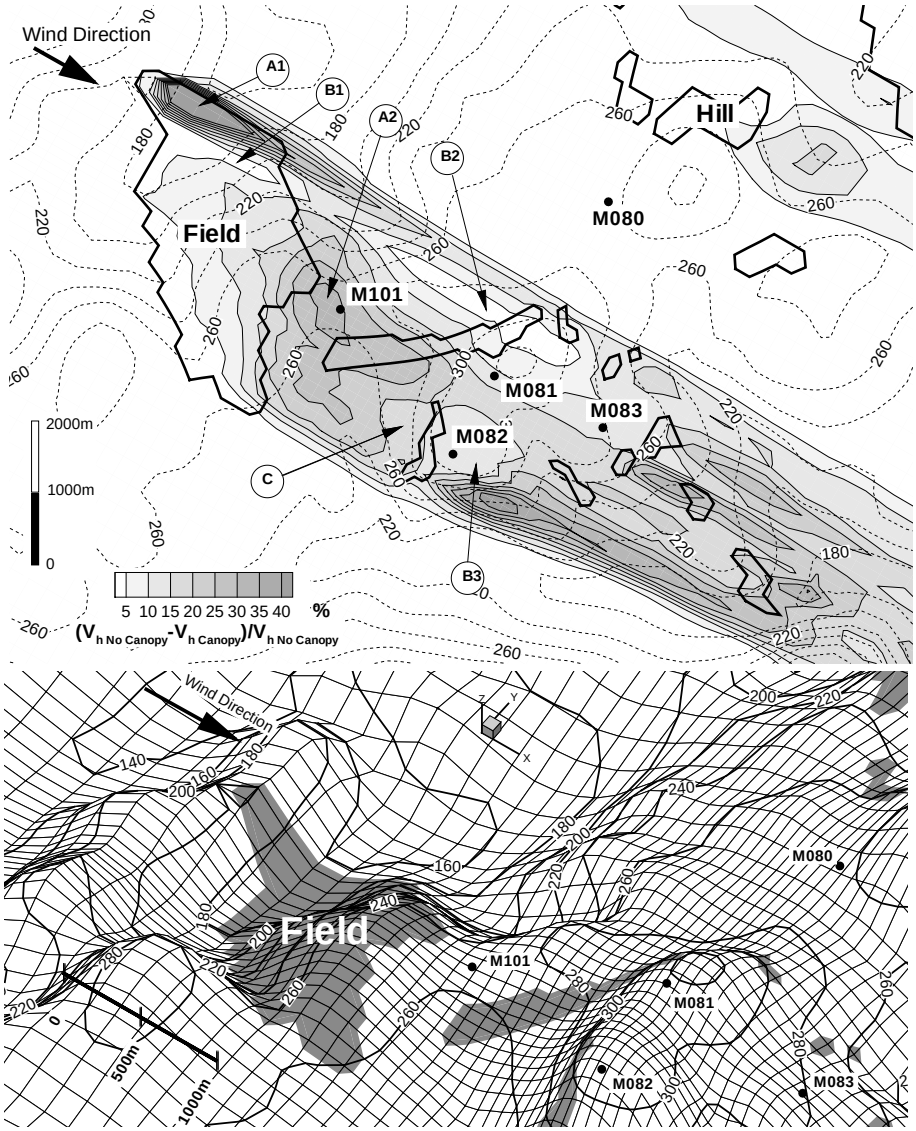

Figure 4.3: Velocity deficit at 47 m agl due to the forest regions, in case of -60º winds and a detailed representation of the trees (canopy-II) also in a perspective view (the vertical scale was magnified 5× with respect to the horizontal scale). Contour heights at every 20 m.

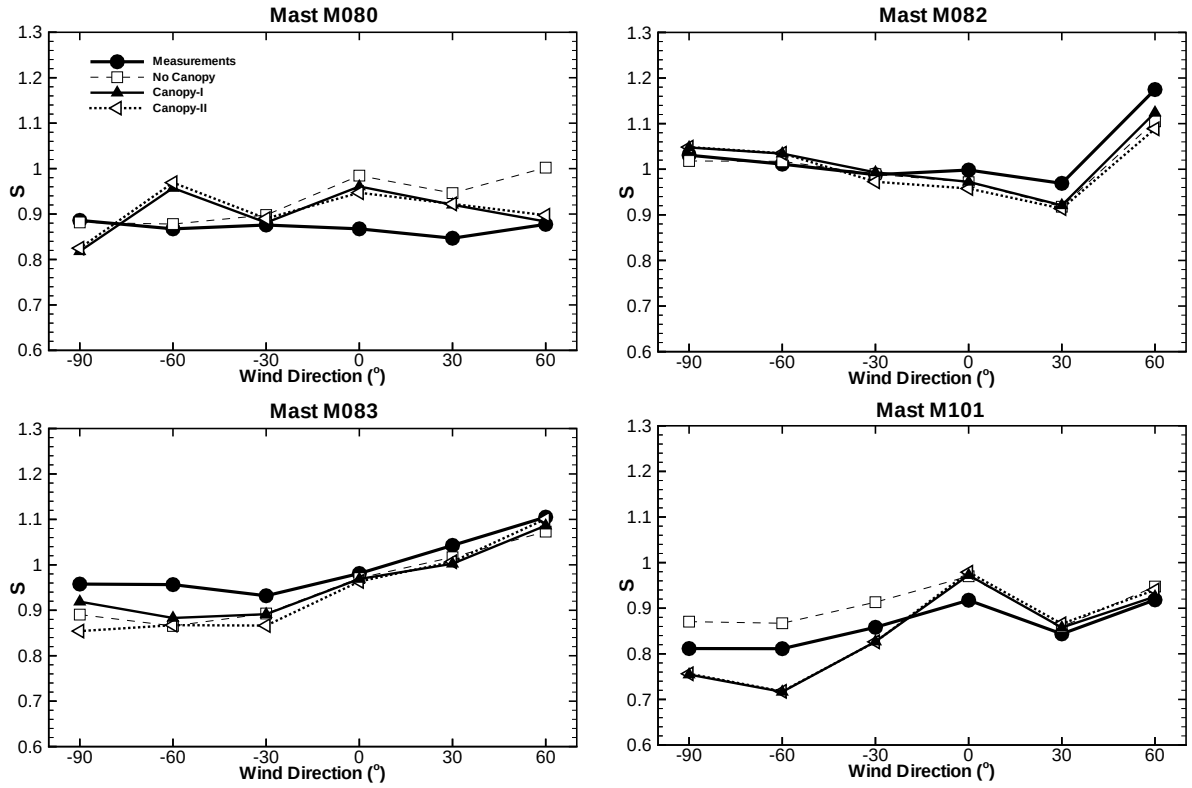

Figure 4.4: Speed-up S at 4 masts as a function of the wind direction. Velocity at mast M081 was used as reference. 0º corresponds to northerly winds.

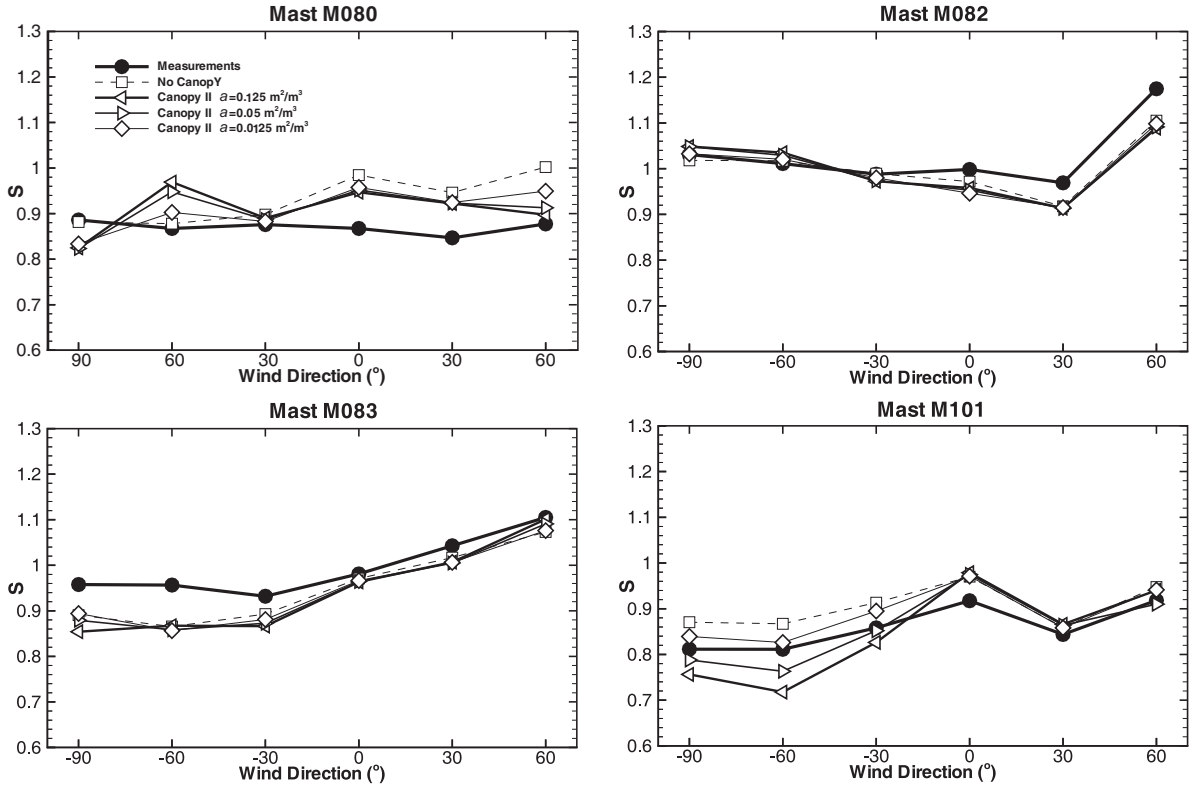

Figure 4.5: Speed-up S at 4 masts as a function of the wind direction and foliage density. Velocity at mast M081 was used as reference. 0° corresponds to northerly winds.

the presence of the trees, and particularly after an *ad-hoc* adjustment of the characteristic roughness (Stuart, 2003) proved to be insufficient.

Comparing now, the results with canopy model (canopy-I and canopy-II) with the field data in figure 4.4, in general (for all masts and directions), one cannot say that the canopy model has improved the agreement with the field data; changes due to the canopy model could be too high (directions -90 and -60 at M101), too low (directions -90 to -30 at M083), or even went in the wrong direction (for instance, the -60 direction at M080). Concerning the two levels of canopy area representation, we can see in figure 4.4 that the results were almost identical; the larger differences between canopy-I and canopy-II cases occurred in mast M083 for wind directions from west to north (-90° to 0°), where the agreement with the field data was worse when using canopy-II.

Because the speed-up (equation 4.1) is a ratio between two variables (V_h and $V_{h_{Ref}}$), if the two variables are affected in the same proportion, or because they refer to locations close to each other, V_h changes little, the speed-up may not show any differences. This can be observed, for instance in figure 4.3, where M082, M083 and the reference mast M081 apart from being within the same contour level region, are also very close to each other.

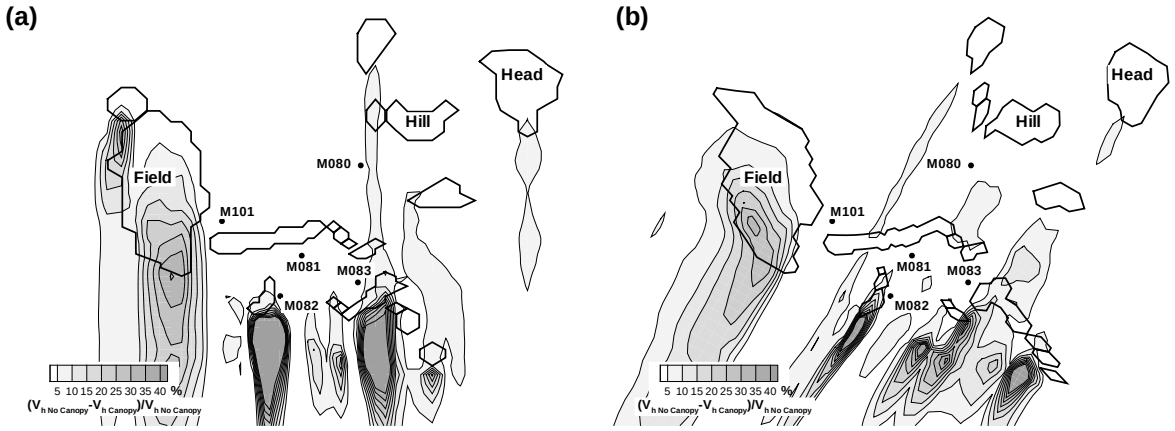

Figure 4.6: Velocity deficit at 47 m agl due to the forest regions, in case of (a) 0° and (b) 30° winds.

For these reasons, we may focus our discussion on masts M101 and M080.

The effect of the canopy model at mast M080 for the 60° wind direction, and at mast M101 for −90°, −60° and -30° wind directions was as expected, i.e. decreasing the speed-up parameter. From figure 4.3 and the discussion above on the use of the speed-up parameter for computer model appraisal, we may conclude that the effect of the canopy model at M080 occurs only in case of 60° winds. For any other directions this location is not downstream of forests either at *Hill* or at *Head* and speed-up changes are only due to different wind speeds at M081, the reference velocity. The over-prediction of the speed-up at M080 in case of -60° winds was not the result of wind speed too high at M080, but a wind speed prediction which was too low at M081. Because of similarities between canopy-I and canopy-II results pointed out above, we may conclude that this was mostly due to the computer modelling of forest at *Field* rather than to the neighbouring wind break "d" (figure 4.2). The same reasoning applies to results at M101, which show that this over-prediction of the wake effect downstream of the forest was even larger nearer *Field*; this also explains why the speed-up at mast M101 for winds at -90° and -60° was lower than the experimental results.

This situation could be improved if lower values of a or C_D were chosen for parametrisation of the *Field* forest. As pointed out in the introduction, and according to Pinard and Wilson (2001), a large uncertainty is associated with setting the canopy model parameters tree type and foliage density. Figure 4.5 is a counterpart to figure 4.4, but showing the effects of reducing the foliage density a from 0.125 as above, to 0.05 and 0.0125 m^2m^{-3}. Comparing the two figures one can see that values of a between 0.05 and 0.0125 m^2m^{-3} seem to be more appropriate to describe the foliage density of trees at *Field*. Setting the a can be an ad-hoc way of correcting for the model deficiencies and may not be acceptable. On the other hand, it can also be seen as a model parameterisation to a particular type of tree in the region, whereby forcing the agreement between the mast data and the model results, one increases the confidence on the model results in nearby regions where

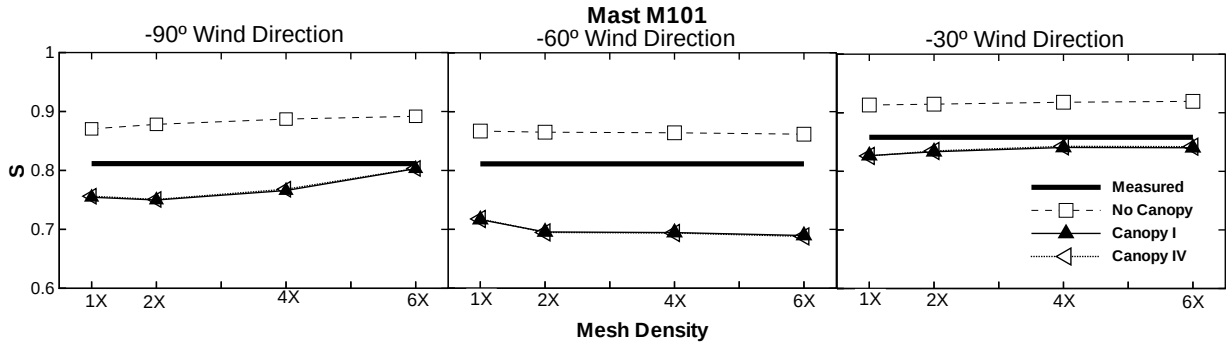

Figure 4.7: Speed-up S at mast M101 for different discretization of the canopy and more refined meshes ($a = 0.125$ m^{2}m^{-3}).

no measurements are available.

The wind speed predictions for -30º winds at M080 and 0º winds at M101 do not show any sensitivity to the canopy model (in figure 4.4) or to the foliage density (in figure 4.5), simply because under those conditions those masts are outside the influence of nearby forests (figure 4.6a). The model results must be seen jointly with the geometry of the canopy and masts may, or may not, be influenced by the presence of the trees, either because the upstream forest is not in their line of sight (M101 in Figure 4.6a); being in the line of sight the wake is not wide enough to reach them (M080 in figure 4.6a); or the impact of upstream trees is not strong enough (M081, M082 and M083 in figure 4.6a). Figure 4.6b shows what we consider an extreme and very illustrative case, where although expected to be affected by the presence of upstream forests, all 5 masts are located in low deficit corridors valid only for this combination of wind direction (30º winds) and canopy topography.

Because canopy representation differs with wind direction, i.e. mesh orientation, cf. figures 4.6a and 4.6b, to remove any doubts that the conclusions reached so far could be due to insufficient terrain discretization and different discretization of the forest, several calculations were made, with increasing mesh density (see table 4.1), for -90º, -60º and -30º winds. The greatest improvement was found (figure 4.7) in case of -90º winds, and for the finest mesh of all only, whereas the -60º wind became worse.

To bring this section to an end, we may note that though, none of the test cases in the present work is appropriate for turbulence model validation, and in spite of all the arguments raised above, one may not ignore the well-known limitations of the $k - \varepsilon$ turbulence model (cf., Pope, 2000), particularly in the case of wake flows. This may account also for the difficulties of the computational model in predicting the velocity at M101 for directions -90º, -60º and -30º, in the wake of *Field*.

4.3 French Case

In the Scottish case (section 4.2), the code validation suffered from shortage of field data, restricted to one height above ground level. The field data in the French region, near Carcassonne, in the South of France (figure 4.8), with measurements up to 100 m, is free from this limitation.

4.3.1 Case Study Description

Figure 4.8: French case: photo of the location.

Figure 4.9 shows the integration domain and an aerial view of forested hills, where the trees are predominantly Douglas fir between 15 and 20 m of height. The terrain height decreases from north to south with a relatively gentle slope of only 2.3°; the maximum and minimum altitudes within the integration domain are 900 and 400 m. Higher slopes occur along the 90° and 120° directions, with a series of valleys and peaks and local slopes that can reach 20°.

The wind originated mainly from the fourth quadrant (westerly to northerly winds), with dominant sectors at 300° and 330°, which were our first choice of wind directions for computer simulation. Directions 120° and 150° were also studied, because they came on

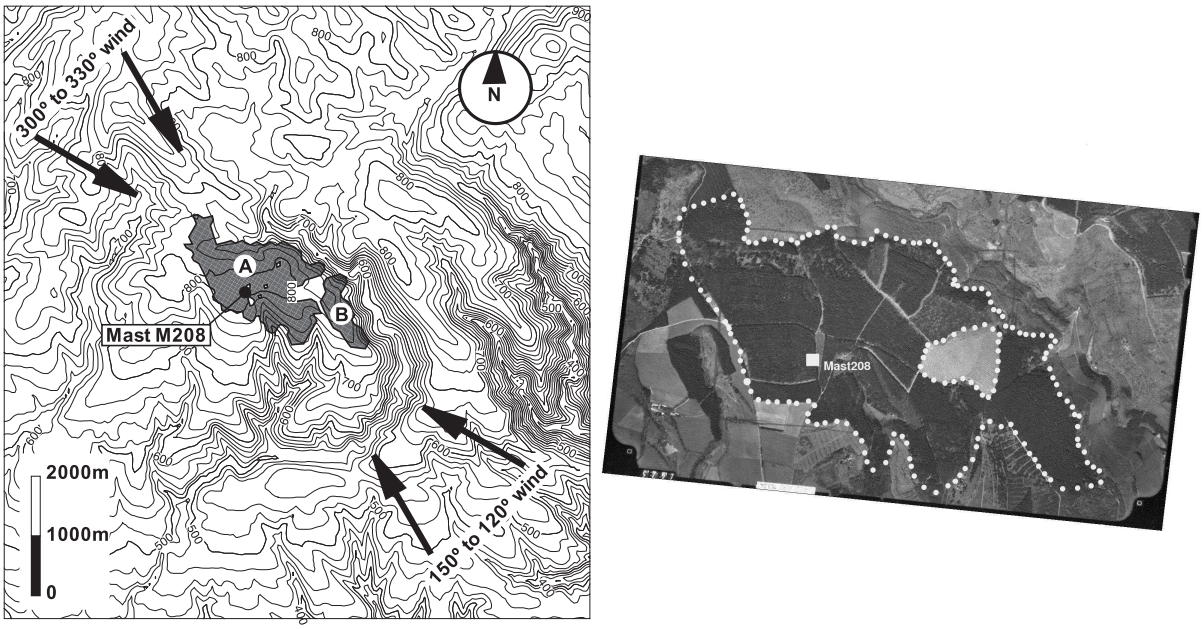

Figure 4.9: French case: (a) Topography, mast locations and canopy region (contour heights at every 10 m). (b) Aerial view with canopy edges

second place in terms of dominant wind sectors, and because of a more complex terrain upwind of the instrumented mast (figure 4.9b).

4.3.2 Numerical Implementation

The calculations were performed on numerical meshes $77\times57\times31$ for an integration domain height of 2000 m, and covering a rectangular region of 11000 m $\times$8000 m, centred on mast M208 (figure 4.9). The minimum grid size was 60 m in the horizontal plane (Δx_{min} and Δy_{min}), and 0.6 m was the height of the first vertical node close to the ground (Δz_{min}).

The height of the inlet boundary layer was set to 150 m and the friction velocity varied between 0.4 and 0.6 ms^{-1}, tuned to replicate the velocity obtained at the 100 m agl anemometer in mast M208. The characteristic roughness length was equal to 0.03 m. The canopy model is the same proposed by Svensson and Häggkvist (1990), described in section 4.2.2. The tree height h varies between 15 m (8 grid nodes along the vertical) and 20, and the density foliage is equal to 0.125 $\mathrm{m}^2\mathrm{m}^{-3}$. After a first set of calculations (figure 4.10) with 4 combinations of tree height and foliage density showed that that was the best combination. The canopy drag coefficient C_D was equal to 0.25. In the case the roughness length and zero-displacement model (RM-roughness model, subsection 2.3.1), z_0 and d were equal to $0.1h$ and $0.75h$.

4.3.3 Results

4.3.3.1 North-Westerly Winds (330° and 300°)

Figure 4.10 shows the vertical profile of horizontal wind speed for 330° winds, compared with computational results of the canopy model (CM) for two tree heights h equal to 15 and 20 m, and two foliage densities a equal to 0.05 and 0.125 m^2m^{-3}. The best agreement with field data was obtained in case of $a = 0.125$ m^2m^{-3}. The results without canopy model, also included for reference, were in poor agreement with the observations, showing the need for a canopy model. A tree height of 15 m and $a = 0.125$ m^2m^{-3} were chosen as canopy parameters.

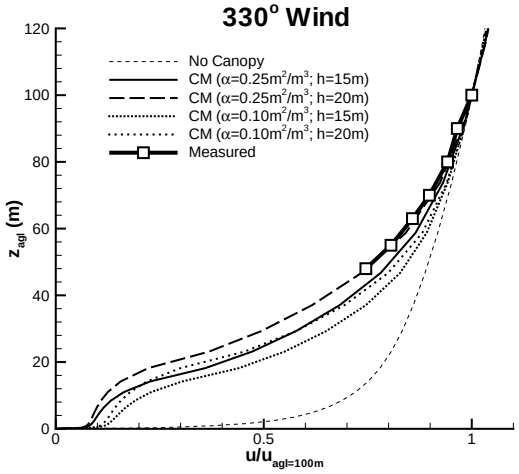

Figure 4.10: Velocity profiles in the case of 330° winds, for two tree heights (h = 15 and 20 m) and foliage density (a =0.10 and 0.25 m^2m^{-3}).

The results using the roughness length and zero-plane displacement model (RM) are in good agreement for the 330° wind direction (figure 4.11a) but slightly below the experimental results for 300° (figure 4.11b). The agreement between the CM and experimental results was again excellent for the 300° direction.

The standard deviation of the 10-min data measured by the cup anemometers are the only turbulence measurements available. Although the cup anemometer measurements are affected to a certain extent by the vertical velocity component, the turbulence field data is made up mostly of the turbulent fluctuations in horizontal planes. The turbulent kinetic energy was modified accordingly, removing its vertical component (w'^2), yielding the computational analog of the measurement data,

$$k_h = \frac{2}{3}k + \nu_t \frac{\partial W}{\partial z}. \tag{4.2}$$

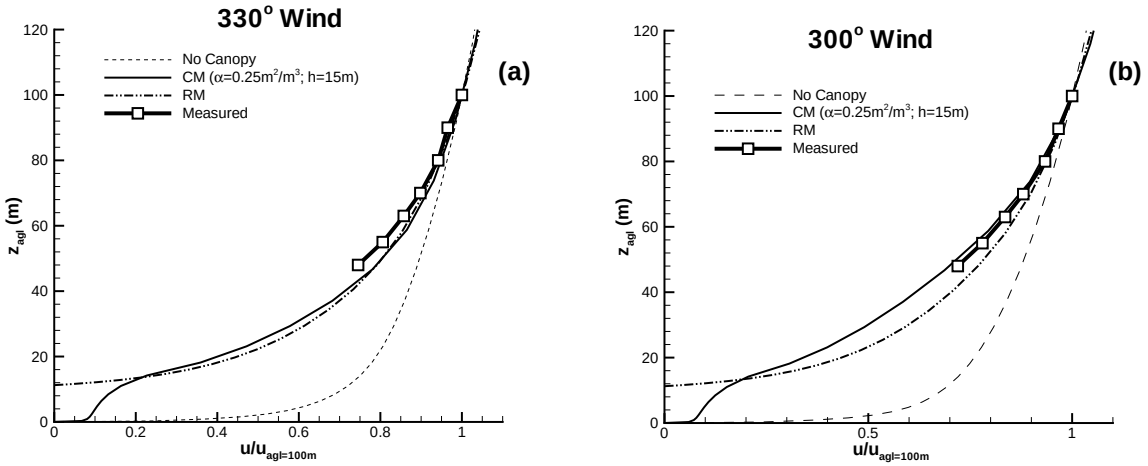

Figure 4.11: Velocity profiles in the case of 330° (a) and 300° (b) winds.

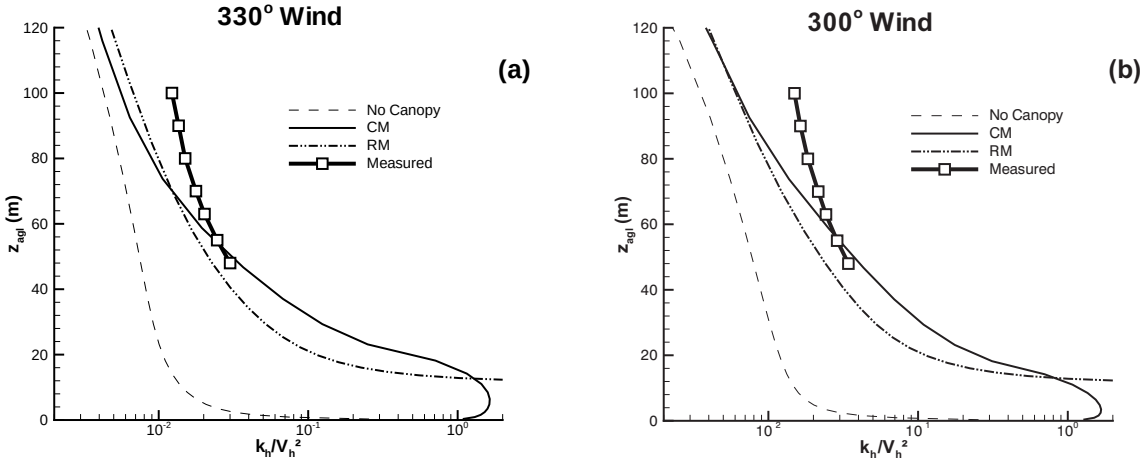

Figure 4.12: Turbulent kinetic energy profiles in the case of 330° (a) and 300° (b) winds.

The turbulence levels at the top of the canopy (z_{agl} = 15 m) for 30º and 300º wind directions (figures 4.12a and 4.12b) are predicted by both the CM and RM models to be two orders of magnitude higher than without canopy model, decreasing to one order of magnitude at 40 m agl. A more accurate measure of how much has the turbulence actually increased in locations closer to the canopy is not possible, because there is no experimental data in this region. Obviously, the RM model cannot resolve the flow within the forest, which is not a serious limitation, at least in case of wind energy, where one is concerned with the vertical profile for locations well above the top of the trees. For both 300º and 330º winds, the simulations yielded an identical decay rate for k_h as the distance from the ground increased, in agreement with the experimental results, though the actual field values were under-predicted. It is difficult to improve these results even further, since the turbulent field 10 or more tree heights above the canopy depends mainly on fields advected from upstream, on which there is no information available.

4.3.3.2 South-Easterly Winds (120º and 150º)

Figure 4.13 shows the horizontal velocity for 120º and 150º winds. The 120º case displayed an S-shape profile, opposed to the linear trend of the field data (figure 4.13a), which could be replicated by the computer model, if the canopy region was replaced by a simple rectangular canopy. This was true for both the canopy and the roughness model, as shown in figure 4.13 by lines labelled RRM and RCM.

Until now one single computer simulation (one single direction) was compared against field data within 30° sectors; however, as shown in figure 4.14a, this is not valid in case of the sector centred at 120º, for which computer simulations were performed at every degree between between 105° and 135° (for clarity, 1 out of 4 profiles is represented in figure 4.14a). The velocity profile is very sensitive to the wind direction and at, for instance 40 m agl, the velocity ratio $U/U_{\text{agl=100m}}$ varies between 0.4 and 0.9. Based on the profile shape and the agreement with the field data, one can identify three main sets: set 1, for 108° and 112° winds, where the velocity is lower than the field data; set 2, for 116°, 120° and 124° winds, all with an S-shape profile; and set 3, for dominant winds at 128° and 132°, that exceeds the experimental values. Recurring to figure 4.9, we can see that easterly winds (108° and 112° , set 1) go through canopy patch "B" and therefore suffer additional drag and wind reduction, compared with set 3. The velocity profiles in set 2 are between these two extreme situations.

We need still to compare the computational results with the field data, and a simple arithmetic mean of all computer simulations (solid line in figure 4.14a) shows a level of agreement between the computational and field data, similar to that achieved in the case of 330º and 300º winds, in subsection 4.3.3.1. Taking advantage of the measured data, one can do weighted averages; however, the 15° rotation of the wind vector between 40 m and

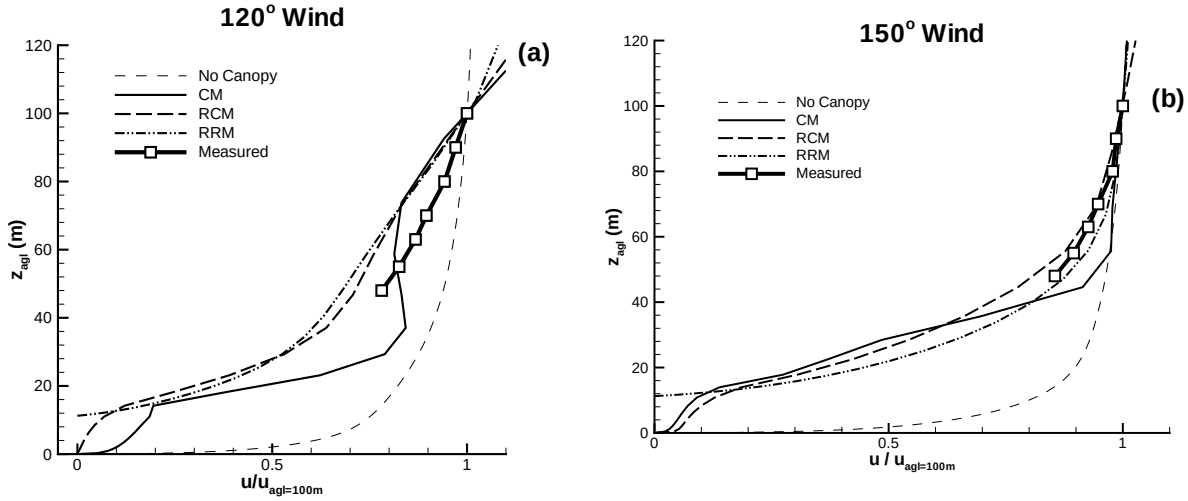

Figure 4.13: Wind velocity profiles for 120° (a) and 150° (b) wind directions. CM, canopy model in a discretized region based on the aerial view; RCM, as above, but applied in a regular (rectangular) region encompassing the canopy as in the aerial view; RRM, canopy region as above, but based on the roughness model

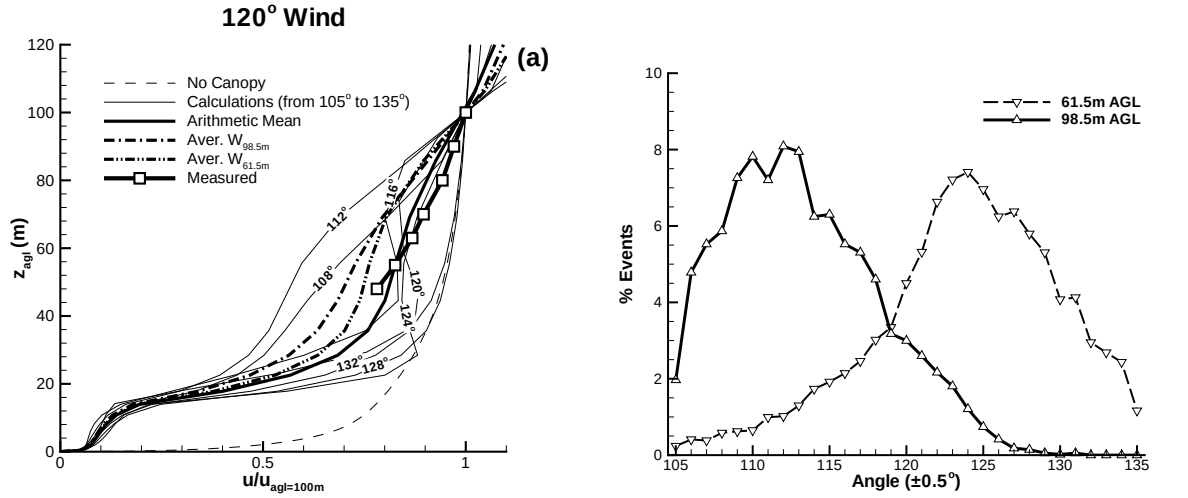

Figure 4.14: Velocity profiles for dominant winds in sector 5 (between 105° and 135°). Average profiles were determined by arithmetic mean, and weighted average based on field data at 61.5 m and 98.5 m agl.

100 m agl (cf. figure 4.14b) provides no clear option for a weighted average, hence we show two additional velocity profiles in figure 4.14a any of which with a better agreement between computational results and field data than in figure 4.13a. Concerning the turbulence

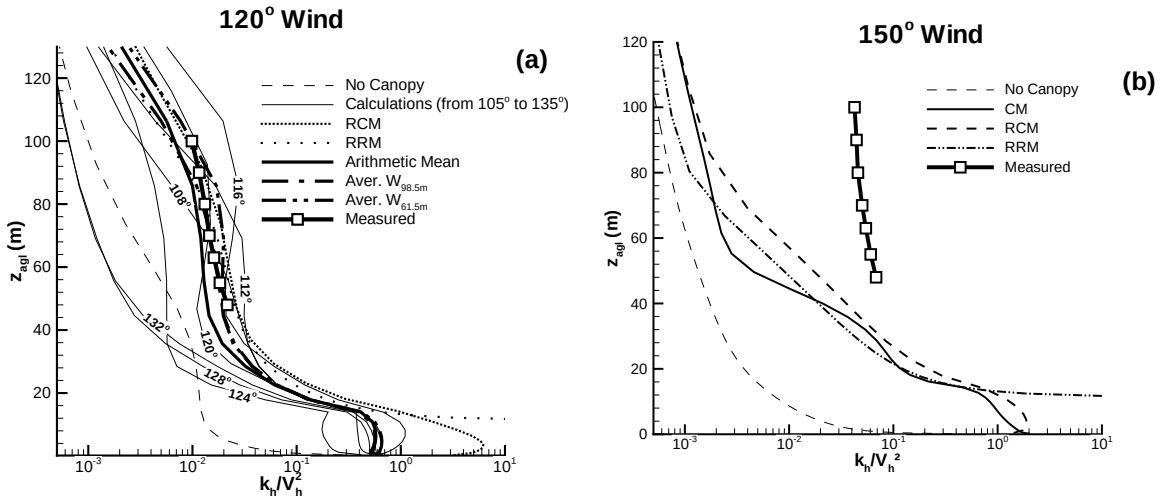

Figure 4.15: Turbulent kinetic energy for 120° (a) and 150° (b) wind directions obtained using the CM and RM canopy models and without canopy model.

intensity (figure 4.15), good agreement was obtained between field data and numerical results in case of the 120° winds, as opposed to the 150° winds, where all models failed to predict the turbulence levels by one order of magnitude.

From all vertical profiles shown above, we may conclude that the cruder one-dimensional model, (RM) in section 2.3.1, also yielded good results and can be a viable alternative in case of uniformly distributed forests, without flow separation, and when the details of the flow near the forest edges are irrelevant.

More information on the effects of the canopy can be obtained by analysing the speed-up and the fractional turbulent kinetic energy at several heights above the ground level, in figures 4.16. Those quantities are defined by $V_h(z)/V_{hinlet}(z)$ and $k(z)/k_{inlet}(z)$, where inlet indicates quantities taken at the inlet boundary. The presence of the canopy decreases the speed-up at all distances above the trees, whose effects can be seen 2000 m downstream of the canopy trailing edge, i.e. about 130 tree heights, cf. figure 4.16a for 20 and 40 m agl. Details of the geometry of the canopy as the presence of small clearings are quickly attenuated with increased distance to the ground.

In case of the turbulent field (figure 4.16b), the results with canopy model presented higher turbulence ratios everywhere above the canopy. Downstream of the canopy at 60 m agl the turbulence ratio is still about 3× larger. Turbulence peaks at 60 m and 10 m agl are associated respectively with the leading and the trailing edges of the canopy.

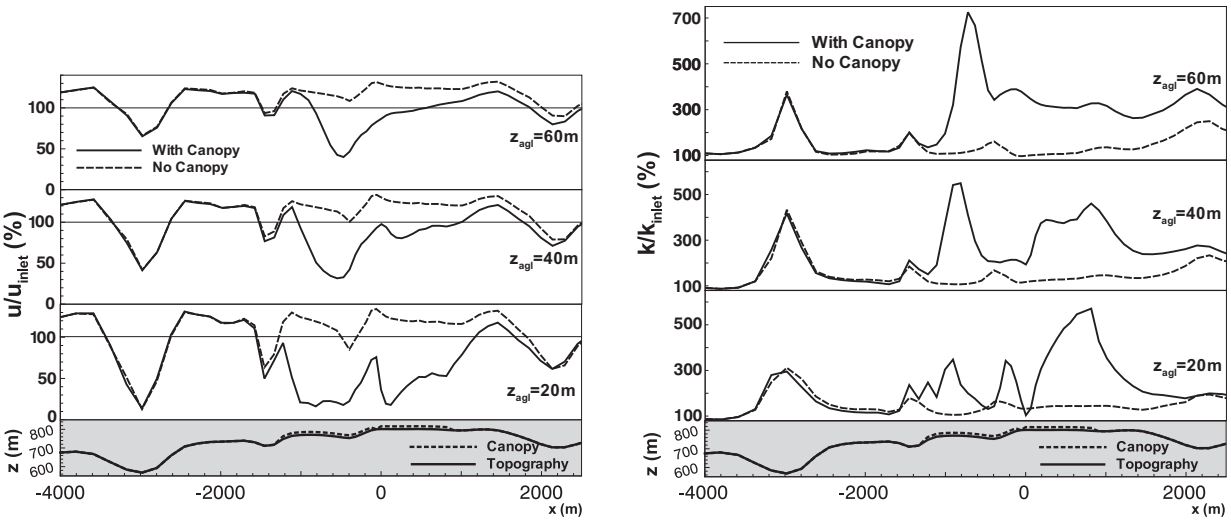

Figure 4.16: Wind velocity ratio (speed-up) and turbulence ratio for a 120° wind at 3 distances above the ground.

4.4 Conclusions

The present study reported the computer simulations of wind flow over forests at two real sites, in Scotland and in the South of France. The canopy model used was that suggested by Svensson and Häggkvist (1990), which is an extension of the $k - \varepsilon$ model.

Previous computational results at the Scottish site, without a canopy model, were unable to replicate the field data for all wind directions. After the canopy model was added, the agreement between the computational results and the field data was much improved. Computer flow simulations highlighted the wind flow structure caused by the trees; strongly depending on the wind direction, there is a complex interplay among the wind direction, the terrain shape and additional wakes due to different forest patches distributed over the region of interest. Calculations with different values of canopy density showed the importance of this parameter, and a major source of uncertainty in real canopy flows.

Results in the French region evidenced the need for a canopy model even more. Only with the canopy model was it possible to replicate the vertical profile of the horizontal velocity. In case of 300 and 330° winds, the agreement was excellent between computational results of horizontal wind speed and the field data. The winds at 120° were a more difficult challenge; because of the influence of the canopy shape upstream, one single direction was not representative of the whole sector. The average of computer simulations 1° apart, for winds between 105° and 135°, also agree with the measurements and revealed many of the detailed features of the wind flow and the importance of resolving all the geometrical details of both the forest and the orography.

The presence of canopy regions can augment the turbulence levels as much as two orders of magnitude, when compared with simulations performed without the canopy model.

Chapter 5

The Performance of Four RaNS k-ε Based Canopy Models Compared to LES

Abstract

The RaNS $k-\varepsilon$ based canopy models available in the literature typically differ in the number of terms used for modelling the canopy flow physics, being available models with one and two terms, in the setup of the model constants. The two terms model class seem to become the established one, due to the increased quality of the predictions produced by the modelling of the turbulent spectral short cut, which turns out to enhance the turbulent dissipation process. Nevertheless, its performance is largely dependent on the constants being used and the present work contributes to the clarification of this feature by systematically testing some of the available models, recurring to the Large Eddy Simulation technique for the establishment of benchmark solutions.

5.1 Introduction

As discussed before, there are some canopy models used in RaNS calculations, such as Svensson and Häggkvist (1990), and some work concerning the study of wind energy potential of a site is done in Lopes da Costa et al. (2006), but its utility and reliability should be improved.

After a bibliographical research, apart from Svensson and Häggkvist (1990), other three models were found: Green (1992), Liu et al. (1998) and Sanz (2003) (this one with some adjustments made by Katul et al. (2004) for atmospheric flows). Those models were chosen

because, differently from Svensson and Häggkvist (1990), they presented a negative contributions in the two source/sink canopy terms for the k and ε equations. This potentially could mimic the "spectral short cut" in the TKE cascade described by Finnigan (2000). Other canopy model constant sets arrived to our knowledge but, briefly tested, did not showed better results than the previous list (Foudhil et al., 2005), or are too recent to be introduced in this study (Sogachev and Panferov, 2006).

The departure of the present chapter is the appraisal of four existing RaNS canopy models and also understand the phenomena involved in a flow among and above a forested region. For this purpose, good data is required, based on very simple conditions, such as a stationary flow over a flat and continuous (infinite) forest. Experimental data of atmospheric flows in those conditions are almost impossible to obtain, for obvious reasons. On the other hand, the complexity and scales of the flow make DNS (Direct Navier-Stokes) calculations not practical to implement.

As a result, LES over a flat and continuous ideal forest was used to provide a basis for comparison with different RaNS canopy models on the same conditions. The comparison will be made on its velocity, TKE and turbulent viscosity results. These parameters are the more representative of the characteristics of the atmospheric flow when one is studying a wind farm. Other important issue are the turbulent mechanisms among a forest and its correct reproduction by the RaNS models. To validate the model behaviour, we will compare the vertical profiles of the k equation terms with LES equivalents, obtained after a statistical treatment of the results.

Almost all wind farm simulations in the vicinity of forests, deal with non-continuous forest areas. It is important that the models deal adequately with the forest edges. This forces us to also simulate wind flow over non-continuous forest, and study the transient behaviour of the models when the flow enters or exit from a forest edge. Simulations were made on a periodic domain with half of the longitudinal direction covered by forest canopy. In those conditions, the several RaNS models will be compared with LES mean velocity and TKE field.

5.1.1 Canopy Models Tested

As discussed in section 2.3, in the k and ε equations, the source/sink terms S_k and S_ε model the mechanisms of turbulence production and destruction due to the canopy foliage. The following framework for the representation of the source/sink terms, used for example by Sanz (2003), can accommodate all the formulations in the published literature:

$$S_k = \rho C_z \left(\beta_p \left| \mathbf{U} \right|^3 - \beta_d \left| \mathbf{U} \right| k \right) , \tag{5.1}$$

$$S_\varepsilon = \rho C_z \left(C_{\varepsilon 4} \beta_p \frac{\varepsilon}{k} \left| \mathbf{U} \right|^3 - C_{\varepsilon 5} \beta_d \left| \mathbf{U} \right| \varepsilon \right) , \tag{5.2}$$

where $C_z = C_D a(z)$. The canopy model constants, $C_{\varepsilon 4}$, $C_{\varepsilon 5}$, β_p and β_d, are presented in table 5.1 for the four configurations used here: Svensson and Häggkvist (1990), Liu et al. (1998), Green (1992) or Sanz (2003) and Katul et al. (2004). The second terms in equations (5.1) and (5.2), those affected by the β_d constant, have the objective of modelling the "spectral short cut" in the turbulent energy cascade, enhancing the dissipation of k Finnigan (2000).

Table 5.1: Constants set used in the different canopy models.

Author	Abbreviation	β_p	β_d	$C_{\varepsilon 4}$	$C_{\varepsilon 5}$
Svensson and Häggkvist (1990)	"Svensson CM"	1.0	0.0	1.95	0.0
Green (1992)	"Green CM"	1.0	4.0	1.5	1.5
Liu et al. (1998)	"Liu CM"	1.0	4.0	1.5	0.6
Sanz (2003) / Katul et al. (2004)	"Sanz CM"	1.0	5.1	0.9	0.9

CM - *Canopy model.*

Two sets of k-ε model constants ($C_{\varepsilon 1}$, $C_{\varepsilon 2}$, C_μ, σ_k, and σ_ε) are presented in table 2.1. The standard constants were used in all works except in Katul et al. (2004), which recommends the "atmospheric constants". Because preliminary tests showed that the atmospheric set yielded an improved agreement with LES results, all calculations presented here were based on the "atmospheric constants" set.

5.1.2 Numerical Parameters

5.1.2.1 Numerical Parameters for the Homogeneous Forest

LES were first made to compare with the results of Shaw and Shumann (1992) and Patton (1997). Following the work of Shaw and Shumann (1992), the domain was set up to 192m $\times$ 96m $\times$ 60m along the longitudinal, transversal and vertical directions, respectively, using a mesh of $96 \times 48 \times 30$ nodes equally spaced in all directions.

To produce a benchmark result for the appraisal of the RaNS canopy models, a LES of higher spatial resolution was performed, with twice the number of the nodes, i.e. $192 \times 96 \times 60$ grid nodes.

The RaNS results were obtained in a domain of 40m $\times$ 10m $\times$ 60m using a mesh of $20 \times 5 \times 60$ nodes. This mesh was equally spaced in both horizontal directions with a vertical mesh spacing increasing linearly from 0.1 m near the ground till 2.0 m at the top of the domain.

All calculations were performed using longitudinal and lateral periodic boundary con-

Table 5.2: Values used for the interpolation of the vertical distribution of foliage area density $a(z)$.

z/h_{can}	0.0	0.1	0.2	0.3	0.4	0.5	0.6	0.7	0.8	0.9	1.0
$\frac{a(z).h_{can}}{LAI}$	0.43	0.45	0.56	0.74	1.10	1.35	1.48	1.47	1.35	1.01	0.00

ditions and with a symmetry condition at the top of the domain. At the surface a non-slip condition was used and wall-laws were specified to obtain the shear stress at ground level with a roughness length $z_0 = 0.02$ m. In all cases the flow had a longitudinal mean velocity $U_{mean} = 2$ m/s.

An integral parameter that is used to characterize a canopy is the Leaf Area Index (LAI),

$$LAI = \int_0^{h_{\rm can}} a(z)dz \ , \tag{5.3}$$

where $a(z)$ is the vertical distribution of foliage area density and h_{can} the canopy height. In the present work we have used values of $LAI = 2$ and $LAI = 5$ for validation of the LES formulation and $LAI = 5$ for the study of the RaNS canopy models. The canopy height was always $h_{can} = 20$ m and the $a(z)$ distributions was similar to Shaw and Shumann (1992) (Table 5.2).

The LES were made using time steps of approximately $\Delta t = 0.2$ s and 0.1 s, for the coarse and fine grid meshes respectively, corresponding to an imposed mean longitudinal Courant numbers of $U_{mean}\Delta t/\Delta x = 0.2$. All simulations were run for 6000 s. In section 5.2.1, for the validation of the LES procedure, statistics where generated using only spatially averaging, accordingly to the reference works of Shaw and Shumann (1992) and Patton (1997). In all other sections, statistics were calculated using spatial horizontal averaging of time averaged results, taken from the last 3000 s of simulation.

With exception of the Liu canopy model simulations, all the results were obtained using the more traditional RaNS approach, where the time derivatives are dropped from the fundamental equations and the results are time averaged quantities. The URaNS simulation used for the Liu canopy model was performed using a time step of $\Delta t = 0.25$ s. The simulation was conducted during almost 11000 s and spatial horizontal averaging was performed over time averaged quantities taken from the last 2500 s of the simulation.

Table 5.3: Distribution of leaf area density used in the flow across forest edge simulations.

z/h_{can}	Leaf area density (m^{-1})
0 - 0.2	0.13
0.2 - 0.4	0.21
0.4 - 0.6	0.36
0.6 - 0.8	0.40
0.8 - 1.0	0.25

5.1.2.2 Numerical Parameters for the Forest Clearing simulation

To study the wind behaviour across canopy edges, we carried out simulations of a periodical canopy zone, based on Yang et al. (2006), using the previous LES and the RaNS canopy models. We considered a canopy height of $h_{can} = 7.5$ m, with a leaf area density distribution as presented on table 5.3 (its vertical integration yields a LAI - leaf area index - of 2, for a canopy height of 7.5 m). We considered a domain height of $6.2h_{can}$ and a length of $38.4h_{can}$, with canopy extended over the second half of this length. The boundary conditions were periodic on the horizontal directions; a non-slip condition was imposed on the lower boundary (roughness: $z_0 = 0.028$ m), while a free-slip condition was placed at the upper boundary.

On LES, we used the previous calculation set. We have considered a domain with a regular mesh of $192 \times 96 \times 31$ grid points, with a grid spacing of $0.2h_{can}$ (which yields 288m×144m×46.5m). Further simulations were made using finer mesh on longitudinal and vertical directions, which yield similar results.

On RaNS calculations, the domain was narrower (288m×4.5m×46.5m), with less grid points ($192 \times 3 \times 48$), for the sake of obtaining quicker solutions; the mesh was regular on the longitudinal and transversal directions (grid spacing of $0.2h_{can}$) and expanding linearly from 0.1 m next to the ground, to 1.5 m at the top of the domain.

5.2 Flow Across Homogeneous Forest

In this section we perform the validation of our LES formulation and discuss the behaviour of the four RaNS canopy models.

Results are presented in dimensionless form, based on the reference quantities, U_{mean} and u^* at the canopy top, and the canopy height h_{can}. The friction velocity at the canopy top, u^*, was calculated from the shear stress at the top of the canopy,

$$u^* = \sqrt{\frac{\tau^*_{xz}}{\rho}}, \tag{5.4}$$

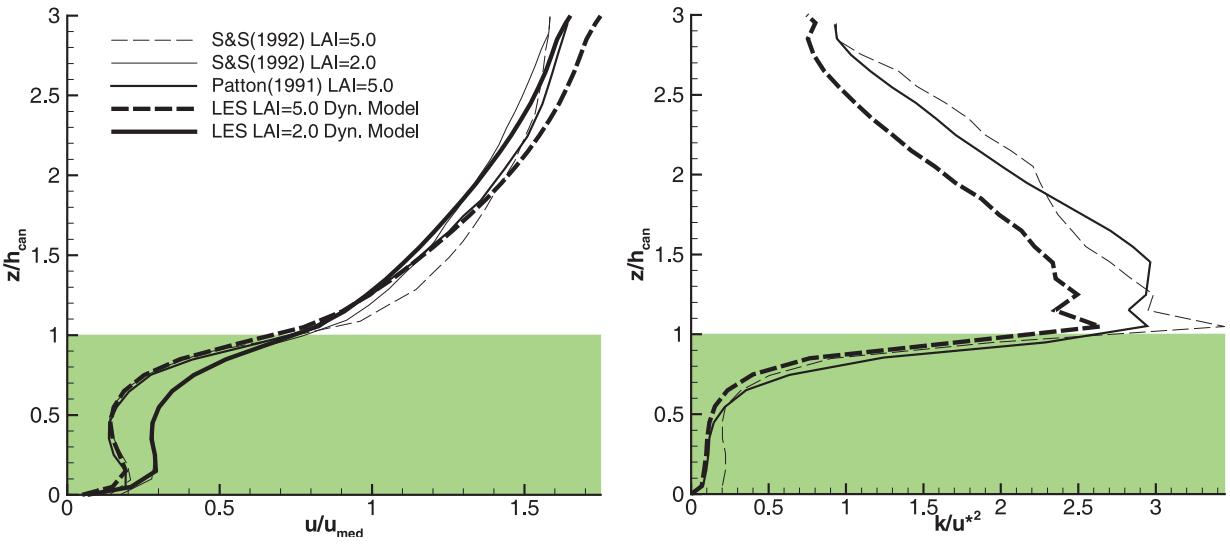

Figure 5.1: Mean longitudinal velocity and total turbulent kinetic energy profiles using LES.

where τ_{xz} is in the case of LES,

$$\tau^*_{xz} = -\rho\overline{u'w'} - \rho\left(\overline{u'w'}\right)_{sg} + \mu\frac{\partial\overline{u}}{\partial z}, \tag{5.5}$$

with $-\rho\left(\overline{u'w'}\right)_{sg}$ representing the sub-grid scale shear stress; whereas for the RaNS results,

$$\tau^*_{xz} = (\mu + \mu_t)\frac{\partial U}{\partial z}. \tag{5.6}$$

5.2.1 LES Validation

The LES code used here was already validated for the simulations of atmospheric flow over topography (Lopes et al., 2007), and here the validation is restricted to the canopy drag force term.

Large eddy simulations of a horizontally homogeneous and neutral flow above and within a forest were made, based on the works of Shaw and Shumann (1992) and Patton (1997). In both of these works no results are presented for a neutral stratification case, so comparisons are made with their weakly unstable cases. Numerical noise was removed from our results, during the post-processing of the results, using a three-point average filter with double weight on central point. Shaw and Shumann (1992) use a two-point average filter.

Figures 5.1 show the vertical profiles of longitudinal velocity and turbulent kinetic energy. The velocity profiles are very similar inside the canopy, where the canopy drag

dominates the flow behaviour. Far from the canopy, near the top of the domain, the velocity results of Shaw and Shumann (1992) and Patton (1997) present lower vertical gradients than the present ones, which can be partially attributed to weakly unstable stratification used in their models. Nevertheless the common behaviour of the results of Shaw and Shumann (1992) and Patton (1997), the present results are in better agreement with the ones of Patton (1997).

The turbulent kinetic energy peaks just above the canopy top, with the present results showing less energy. This may be due to the absence of the thermal production of turbulence in the present simulations. However, in the upper half of the canopy, where the canopy drag dominates the flow over buoyancy mechanisms, all results are in good agreement.

To conclude, we can say that the agreement between our results and those in the published literature is good, and our code can certainly be used to create a data basis for appraisal of RaNS results.

5.2.2 Comparing LES with RaNS Results

5.2.2.1 Vertical Profiles of Velocity, TKE and Turbulent Viscosity

Longitudinal velocity component and turbulent kinetic energy are presented in figure 5.2. The LES profiles were obtained using a mesh with twice the node density in section 5.2.1, yielding smoother profiles and better results at canopy top (as we will see in section 5.2.2.2). Apart from Liu et al. (1998), all k-ε canopy models converged to a steady-state solution. The periodic ensemble average results from the Liu et al. (1998) model simulations were time averaged over 2500 s.

In the case of the models by "Sanz" and "Svensson", the agreement between longitudinal velocity profiles with the LES results was good in the canopy and its near vicinity (5.2); "Liu" averaged profile and "Green" profile present larger deviation. Due to mass conservation, the differences in longitudinal velocity observed inside and in the vicinity of the canopy has impact on the rest of the profile, justifying some of the differences found with the results from "Sanz" and "Svensson" models above $z/h_{can} = 2$.

Major differences between the different model results could be found in the kinetic energy profiles, here normalized by friction velocity (u_*) at the canopy top. All RaNS canopy models overestimated the turbulent kinetic energy. The peak value predicted by "Svensson" exceeded, by a factor of 3, the LES peak value; "Liu" model was similar to "Svensson" in the region above the canopy, whereas within the canopy region its results were close to the LES results. The "Sanz" model presents the second best result of k inside the canopy, but near the canopy top overestimates the turbulent kinetic energy by a factor of almost 1.7×.

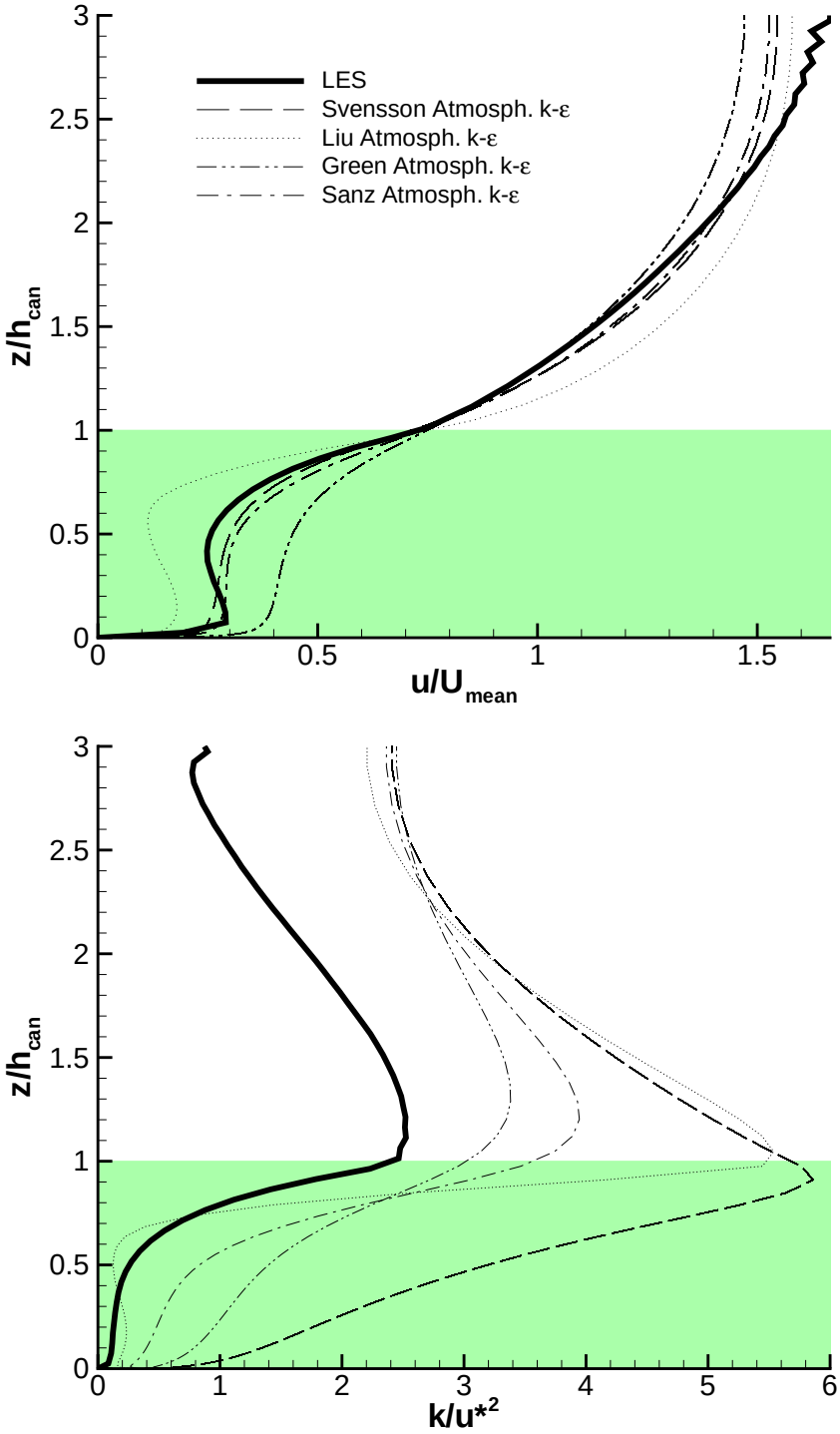

Figure 5.2: Longitudinal velocity and turbulent kinetic energy vertical profiles, obtained by LES and k-ε calculations, using different canopy models. All calculations considered LAI=2.0. Results for "Liu Canopy Model" were time averaged.

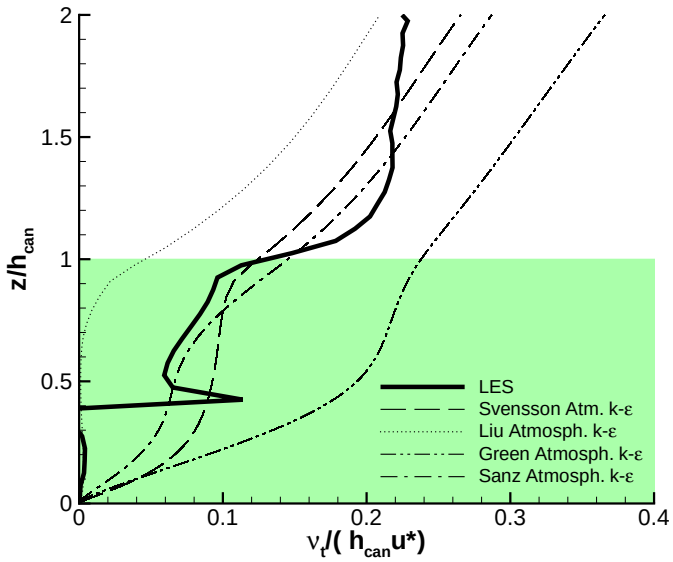

Figure 5.3: Viscosity vertical profiles, obtained by LES and k-ε calculations, using different canopy models (CM). Values normalised by canopy height (h_{can}) and friction velocity at canopy height (u^*).

Another form of analysis can be established in figure 5.3, comparing the calculated RaNS eddy viscosity profiles with the one implied in the LES results,

$$\nu_t = \frac{\tau_{xz}}{\rho \partial \overline{u}/\partial z}. \tag{5.7}$$

We have smoothed the $\overline{u}$ profile with a centred three points average in order to sweep out some numerical noise and obtain a smooth turbulent viscosity graph. Negative eddy viscosities associated to counter-gradient momentum transport were also removed, as they are beyond the capabilities of the actual RaNS turbulence model.

The low eddy viscosity of the "Liu" model precluded the achievement of a steady state flow. This is a consequence of low $C_{\varepsilon 5}/C_{\varepsilon 4}$ relationship (see table 5.1), which promoted the build up of large ε values, as will be seen in the following section. The "Svensson" model ignores the enhanced dissipation mechanism that results from the spectral short cut experienced by the turbulence inside the canopy, leading to an over prediction of both turbulent kinetic energy and its dissipation. Nevertheless, the eddy viscosity produced by this model was of adequate magnitude for the purpose of velocity prediction, as can be seen in figure 5.3.

The "Green" model seems to under-estimate the short cut of turbulent kinetic energy (small β_d), and therefore over-predicts k inside the canopy, resulting in large eddy viscosity (figure 5.3) and an exaggeration of downward momentum flux, visible in the large longitudinal velocities inside the canopy (figure 5.2).

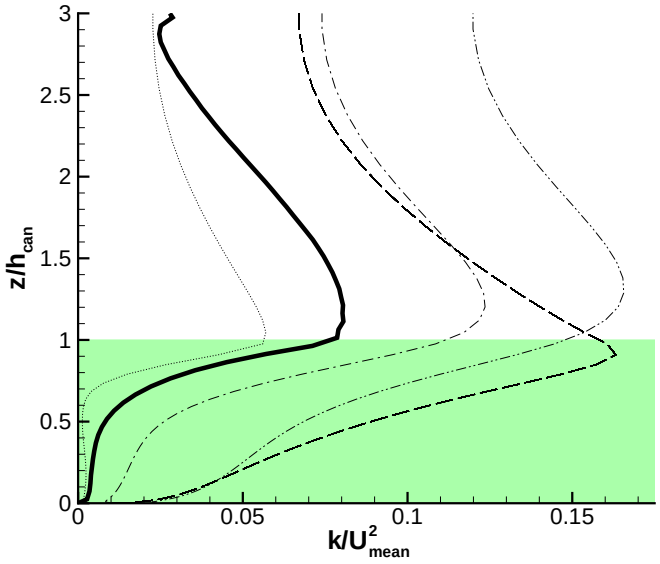

Figure 5.4: Turbulent kinetic energy vertical profiles made dimensionless with U_{mean}, obtained by LES and k-ε calculations, using different canopy models (CM). Key caption as in figure 5.3.

We have also found the need to compare absolute values of turbulent kinetic energy, which was made dimensionless taking $U_{mean} = 2$ m/s as the velocity scale, since U_{mean} was equally imposed in all simulations. Those results are presented in figure 5.4.

This representation, to be compared with that in figure 5.2, evidences the over-prediction of k by "Svensson", "Green" and "Sanz" models, as opposed to the under-prediction of "Liu".

In qualitative terms, "Sanz" seams to be the best model, with a trend that closely follows the LES results.

5.2.2.2 Turbulent kinetic energy (TKE) budgets

For the analysis of the turbulent kinetic energy budgets, the terms in the transport equation were grouped as follows:

$$\underbrace{div\left(\rho k \mathbf{U}\right)}_{\text{Convection}} = \underbrace{div\left(-\overline{p'\mathbf{u}'} + 2\mu\overline{\mathbf{u}'s'_{ij}} - \rho\frac{1}{2}\overline{u'_i.u'_iu'_j}\right)}_{\text{Diffusion}} - \underbrace{2\mu\overline{s'_{ij}.s'_{ij}}}_{\varepsilon} - \underbrace{\rho\overline{u'_iu'_j}.\overline{S}_{ij}}_{\text{Production}} + \underbrace{S_k}_{\text{Canopy Source Term}}, \tag{5.8}$$

where $\overline{S}_{ij} = \frac{1}{2}\left(\frac{\partial \overline{u}_i}{\partial x_j} + \frac{\partial \overline{u}_j}{\partial x_i}\right)$ and $s'_{ij} = \frac{1}{2}\left(\frac{\partial u'_i}{\partial x_j} + \frac{\partial u'_j}{\partial x_i}\right)$. The canopy TKE production term, S_k, is an out of balance term, requiring no definition, which can be accurately determined.

For the RaNS results we used,

$$\underbrace{div\,(\rho k \mathbf{U})}_{\text{Convection}} = \underbrace{\frac{\partial}{\partial x_j}\left[\left(\mu + \frac{\mu_t}{\sigma_k}\right)\frac{\partial k}{\partial x_j}\right]}_{\text{Diffusion}} - \underbrace{\rho\varepsilon}_{\varepsilon} + \underbrace{\mathcal{P}_k}_{\text{Production}} + \underbrace{S_k}_{\text{Canopy Source Term}} . \tag{5.9}$$

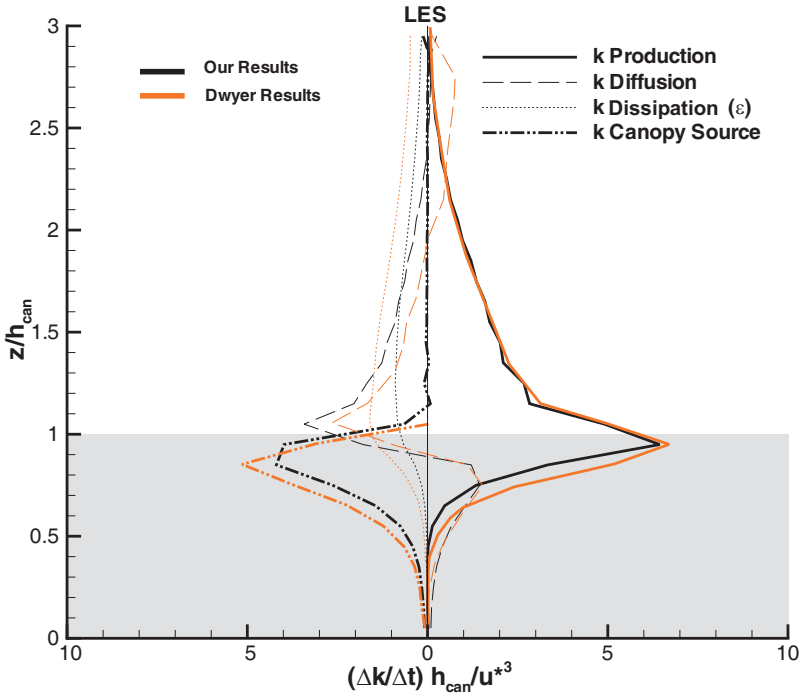

Figure 5.5: LES TKE budget terms. Values normalised by canopy height (h_{can}) and friction velocity at canopy height (u^*).

A comparison in figure 5.5 of our coarse mesh LES turbulent kinetic energy budgets with the ones of Dwyer et al. (1997) which is identical to similar to those by Patton (1997), showed similar energy distributions, but also some numerical discontinuities. The benchmark results for appraisal of the RaNS budgets were based on a finer mesh, with twice the number of nodes, and are presented in figure 5.6.

In figure 5.6 we can see, as expected, the highest gradients around the forest top, where we can find the highest values for the TKE production. Here, the shear generated TKE (production term) is balanced above the canopy, almost until $z/h_{can} = 2$, mainly by the diffusion term. The local equilibrium, a balance between local production and dissipation, can only be reached for higher locations, outside the roughness sublayer which typically extends to heights around $z/h_{can} = 3$ (Finnigan, 2000). Inside the canopy there is no

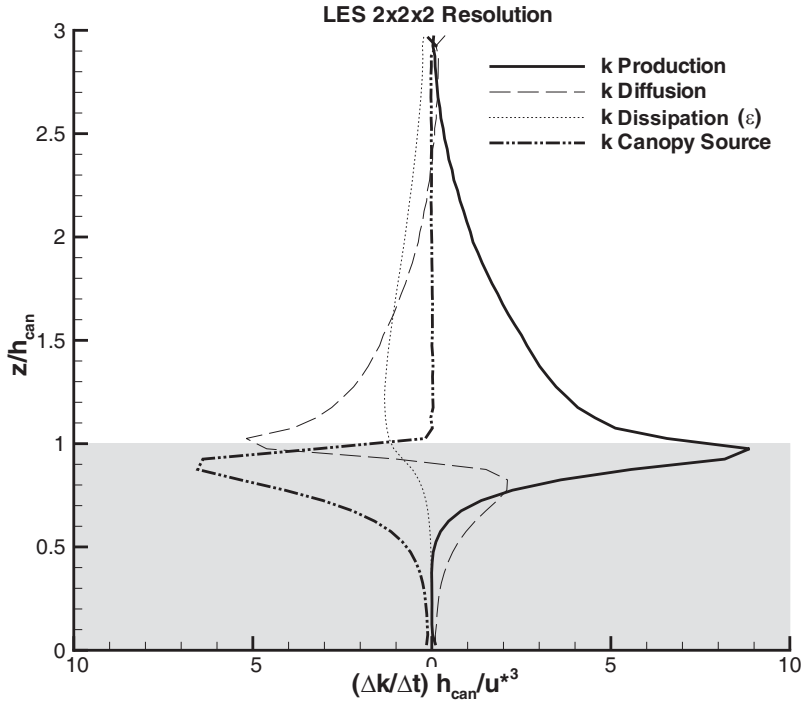

Figure 5.6: LES TKE budget terms on a finer mesh. Values normalized by canopy height (h_{can}) and friction velocity at canopy height (u^*).

local equilibrium and the canopy drag term leads the dissipation of turbulent energy. The turbulent diffusion transports energy from the top of the canopy, where there is large production, to inner locations.

The TKE budget terms obtained by LES are presented in figure 5.6, and the equivalent for the different RaNS model are presented in figures 5.7 and 5.8. Accordingly with the Svensson and Häggkvist (1990) model, the contribution of the canopy term is positive, opposed to the LES results (figure 5.6) that showed a negative contribution throughout the whole canopy heigh. As a consequence, the diffusion term is negative, where it should be positive, and the dissipation term is too large. This is, in general terms, the behaviour also evidenced by the "Liu" model, in figure 5.7, although it also displays a local equilibrium within the canopy.

On the other hand, "Green" and "Sans" results (figures 5.8) behave more accordingly to what was found in the LES results. Of these two budgets, "Sanz" follows more closely the LES results, in spite of its difficulty in predicting the correct magnitude of the LES terms around the canopy top.

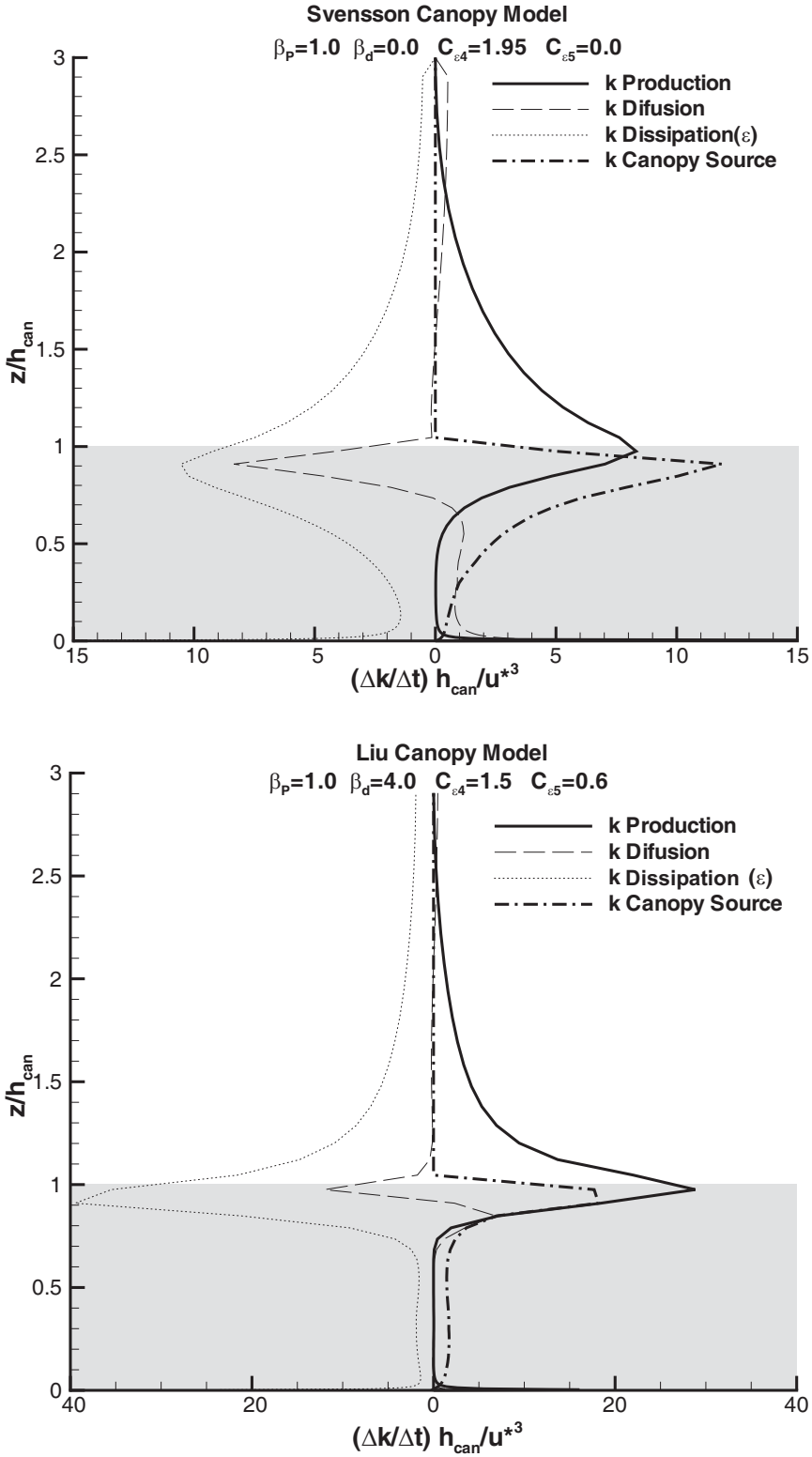

Figure 5.7: RaNS calculations TKE budget terms for the "Svensson CM" and "Liu CM" (space and time averaged values for this case). Values normalised by canopy height (h_{can}) and friction velocity at canopy height (u^*). Note that the horizontal scale range is much wider than in figure 5.6.

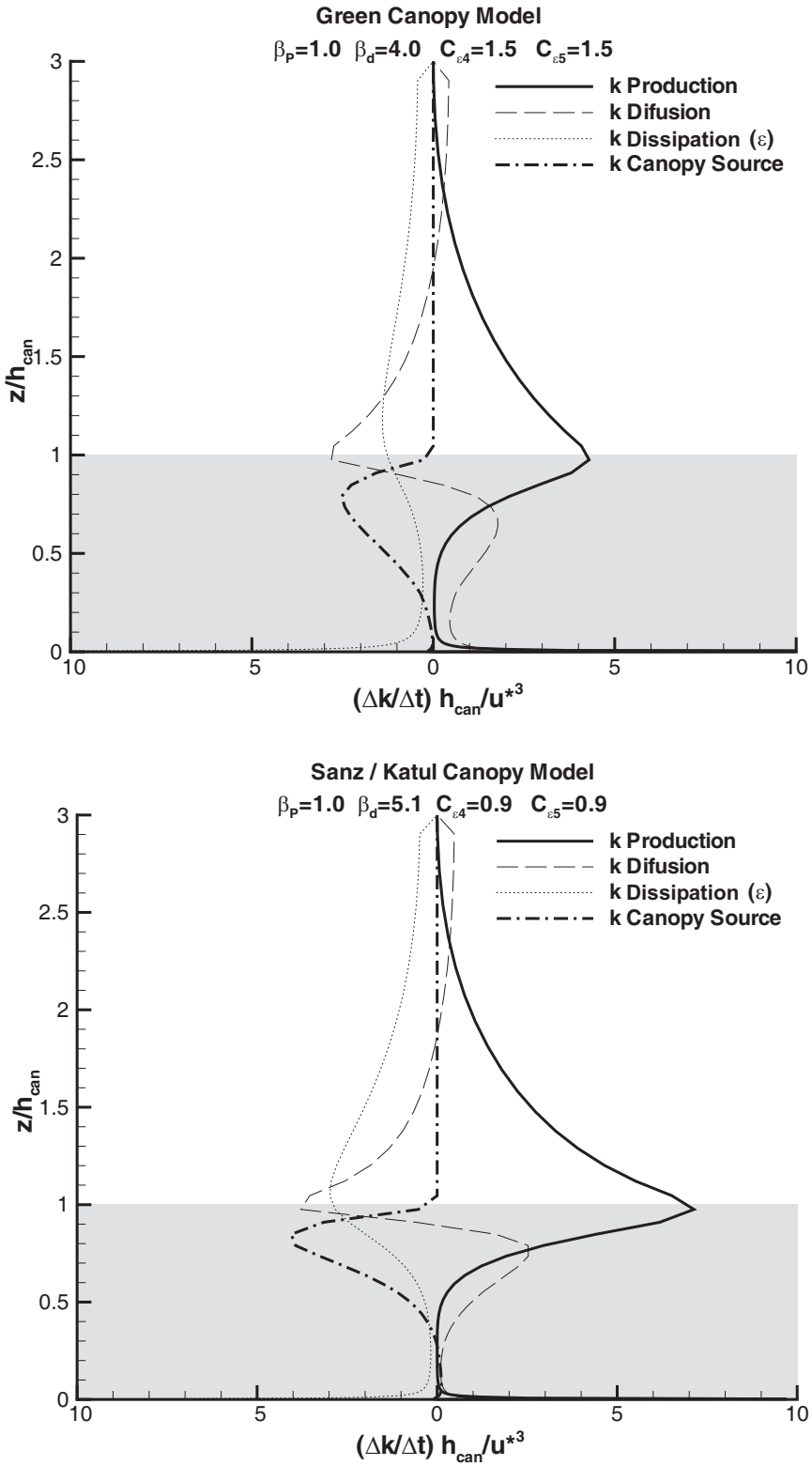

Figure 5.8: RaNS calculations TKE budget terms for "Green CM" and "Sanz CM". Values normalised by canopy height (h_{can}) and friction velocity at canopy height (u^*).

5.3 Flow across a forest clearing

In the previous sections, we have tested the canopy models for an ideal flow over a horizontally uniform and continuous forest, considering no longitudinal perturbations. On real cases, wind flow over forested regions of finite size, and canopy edges and clearings cannot be neglected by a numerical canopy model.

In this study, we simulated a forest clearing, represented by a periodical canopy zone, based on Yang et al. (2006). In this study, results were validated by comparing it with field measurements made by Irvine et al. (1997). The numerical details were presented in section 5.1.2.

5.3.1 Results

The results are presented on figures 5.9, 5.10 and 5.11. We compare LES, with RaNS k-ε atmospheric constants using "Svesson", "Green" and "Sanz" canopy model constants. The "Liu" model was excluded, because of difficulties of numerical convergence.

The velocity shows that RaNS models have a slower response to the effect of the canopy. "Svensson CM" velocity profile reacts more accordingly with LES, to the appearing canopy, as can be seen in figure 5.9, comparing the positions of the "S" shape portion of the 0.4 contour near the edge of the canopy. On the other hand, it has some delay to recover, as shown by the high velocity values in the regions between canopies $x/h_{can} < 0$ (figure 5.11).

The main differences between the different models could be found in the TKE results. In figure 5.10, the LES fields show that TKE is much weaker in all the domain, and namely inside the canopy. Meanwhile, on the top of the canopy the mixing layer acts as a TKE producer. This higher TKE region develops itself in to the canopy wake. Regarding the RaNS results, the predicted TKE fields reach higher values than LES, specially inside the canopy. There are some differences on shape of TKE distribution, particularly with "Svensson CM" which develops a high TKE bubble just after the canopy edge. Its TKE vertical profile shape, in this zone, completely differ from LES and other RaNS models results (figure 5.11).

Once again, "Sanz CM" proved to be the best RaNS canopy model which, in spite of a weaker response to the perturbation caused by the canopy, displayed a higher quality prediction of TKE.

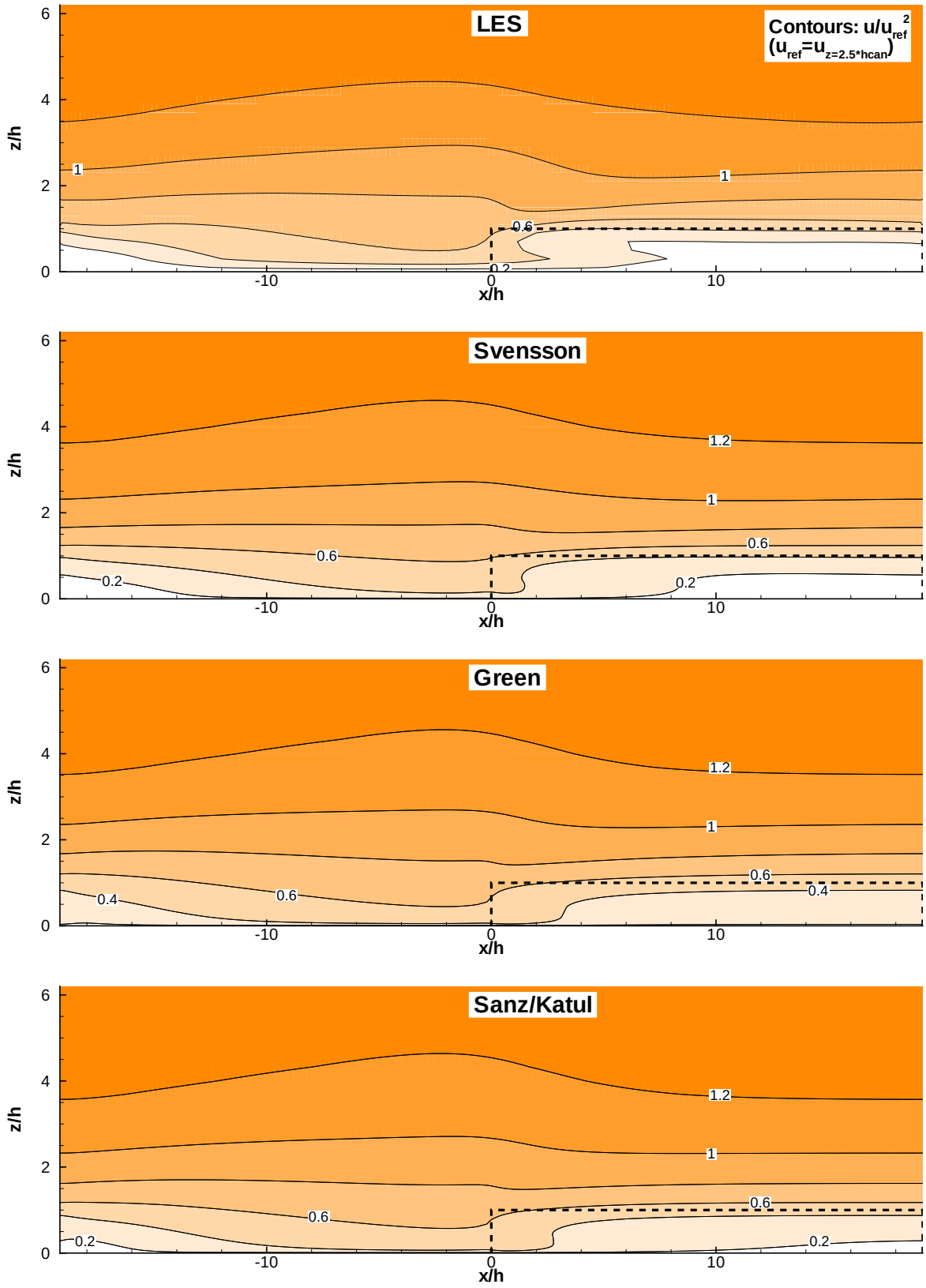

Figure 5.9: Longitudinal velocity contours, on a longitudinal section of the domain. Values normalised by u_{ref}, i. e., space average longitudinal velocity at $z = 2.5h_{can}$.

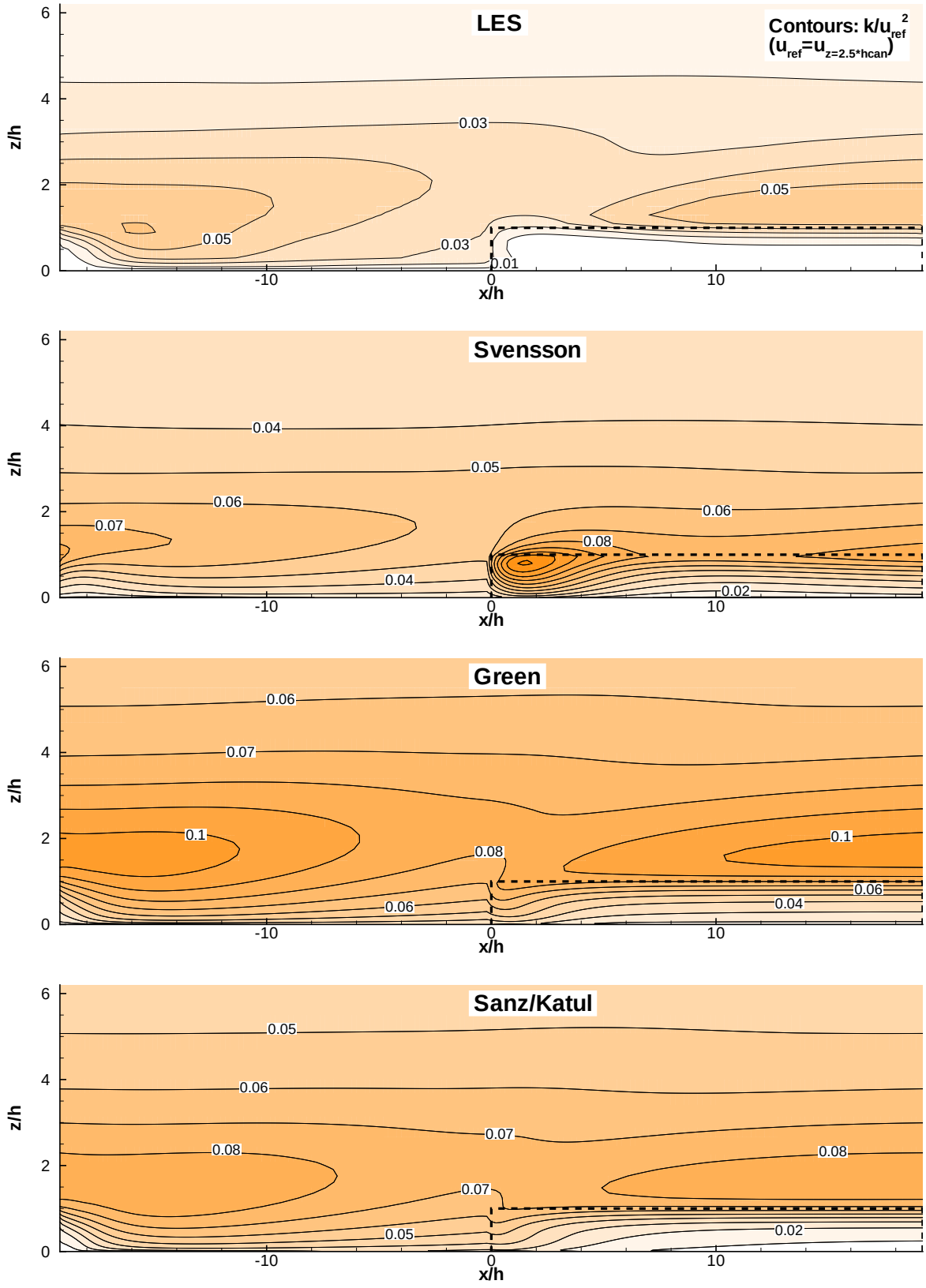

Figure 5.10: Turbulent kinetic energy contours, on a longitudinal section of the domain. Values normalised by u_{ref}, i. e., space average longitudinal velocity at $z = 2.5h_{can}$.

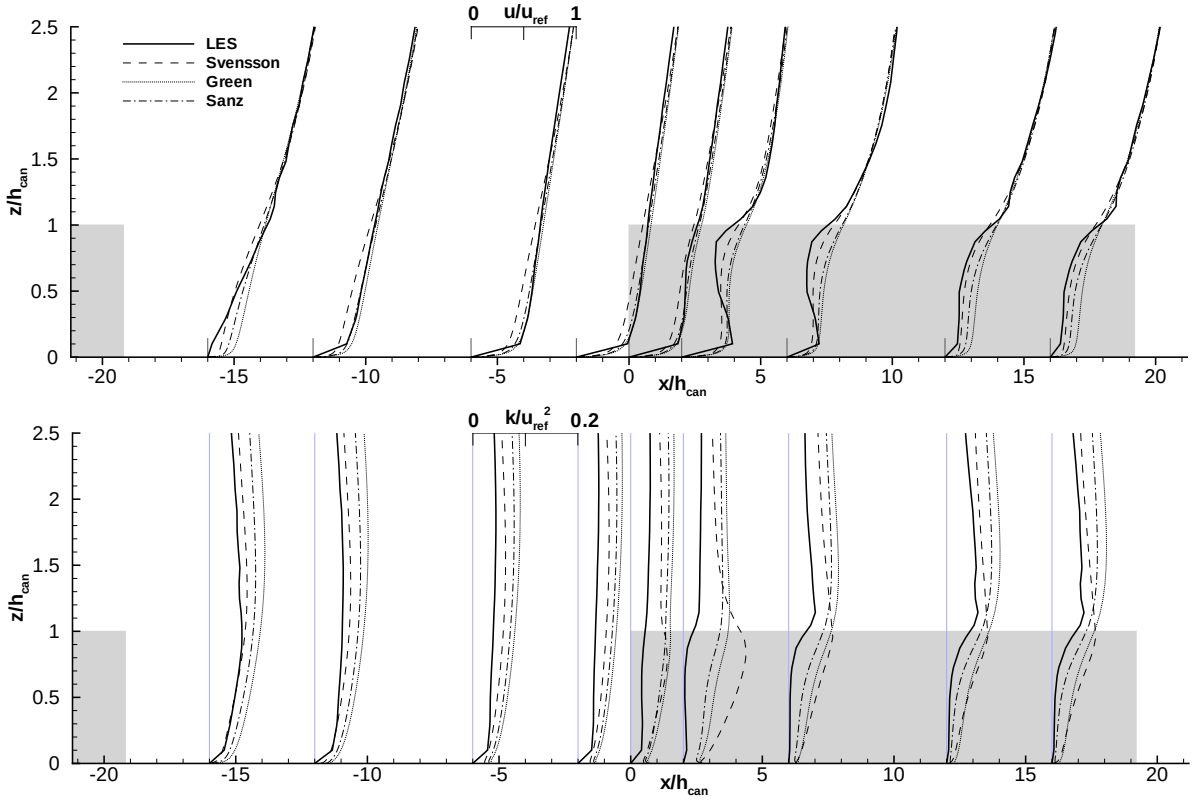

Figure 5.11: Velocity and turbulent kinetic energy profiles, on a longitudinal section of the domain. Values normalised by u_{ref}, i. e., space average longitudinal velocity at $z = 2.5h_{can}$.

5.4 Conclusions

In this chapter, the performance of four RaNS k-ε based canopy models was tested, using LES as a benchmark. From this work we may present the following conclusions:

1. The Sanz (2003) canopy model seems to be the most appropriate, when compared with large-eddy simulation of flows over homogeneous forests and also across a forest edge. Velocity and TKE profiles are similar to those obtained by LES.

2. The budget of turbulent kinetic energy showed that Sanz (2003) canopy model was the one that better described the relative magnitude of the several mechanisms at play inside the roughness sub-layer, using the LES as the benchmark result.

3. The "Svensson" model, used in Chapter 4, performed well in the velocity prediction but fail in the TKE prediction by showing very large k values.

4. Among the four RaNS canopy models tested, although they may produce acceptable results when we observe limited aspects of the flow (velocity or TKE profiles), some of them completely fail to mimic the physics of turbulence as shown by LES. This was evidenced when the budget terms of k equation were compared to LES; only Sanz (2003) and Green (1992) models presented a comparable behaviour to LES on this issue.

5. Models with only one positive canopy TKE equations term, such as Svensson and Häggkvist (1990) model, are not adequate to predict both velocity and turbulent kinetic energy. This model presents a turbulent mechanism that acts on the opposite sense to LES, representing the canopy as a source of k, instead of a sink. This lack of accuracy is unacceptable if we intend to simulate the several aspects of a flow over a wind farm location surrounded by forested areas. It produces excessive k, which confirms the practice established within RES - Renewable Energy Systems Ltd. - that started using the Svensson and Häggkvist (1990) canopy model in their simulations with VENTOS®, and have noticed that it over-predicted the turbulence, on a regular basis (Stuart, private commentaries).

6. It is not a sufficient condition for a model to have a component in the canopy TKE equations term. The Liu et al. (1998) model, although present this component, simulate the canopy as a k positive source. It is also necessary to have an adequately balanced canopy model constant set.

Chapter 6

Canopy Related Constants

Abstract

The Sanz (2003) procedure for determining of the canopy model constants, using k-ε turbulent model, was extended using k-ε-$\overline{v^2}$-f turbulent model. An explicit derivation for the canopy related constants β_p and β_d was established, which became functions of the turbulence models constants.

Several experiments on a channel flow were made, with the intent of adjust the turbulence model constants based on LES results. The various set of canopy constant set obtained were tested using both k-ε and k-ε-$\overline{v^2}$-f turbulence model. A canopy model constant set, named "CM1", proved to satisfactorily mimic the LES results, when used on k-ε turbulent model.

The results were an improvement of Sanz (2003) and Katul et al. (2004) canopy model constant set, observed to be the best model among the ones tested on the previous chapter.

6.1 Introduction

In Chapter 5 several RANS canopy models were tested using LES over a flat and continuous forest and a forest edge as benchmark. Velocity, turbulent kinetic energy (TKE) and the vertical distribution of the terms of the TKE equation (inside and above canopy) were compared to test the ability of the models to reproduce the turbulence mechanisms. Some of them completely failed in this matter, while others reproduce approximately the same TKE terms vertical distribution. This was the case of the models presented by Green (1992) and Sanz (2003).

We will centre our attention on Sanz (2003), that has partially deduced the canopy

model constants combining Kolmogorov's relation in the k-ε canopy model equations, considering a dense and homogeneous canopy where the mixing length does not vary. We will present a more comprehensive set of constants, introducing the same principles in the k-ε-$\overline{v^2}$-f canopy model equations. The two complementary equations of this RANS model should allow us to do that.

6.2 Using k-ε-$\overline{v^2}$-f Turbulence Model to Tune the Canopy Model constants

Following the conclusions of Chapter 5, the canopy model constants used in Sanz (2003) yielded the best results for the simple case of an horizontally homogeneous canopy. These model coefficients β_p, β_d, $C_{\varepsilon 4}$ and $C_{\varepsilon 5}$ were derived on the basis of physical constraints, applied to the k-ε model equations, and arbitrarily estimate values for β_p $(= 1)$ and $C_{\varepsilon 4}$ or $C_{\varepsilon 5}$ $(C_{\varepsilon 4} = C_{\varepsilon 5})$, adding an apparent weakness to the procedure. In an attempt to remove the apparent weaknesses of the Sanz model, we use the k-ε-$\overline{v^2}$-f (Durbin, 1991, 1995) and its four transport equations to enhance the analytical determination of the canopy model constants. Further on, we will conclude that it will only be possible to explicitly determine β_p and β_d.

6.2.1 Canopy Model Constants Relations Based on k-ε Model.

For comprehensiveness and understanding of the additional steps in our procedure, the procedure followed by Sanz (2003), using the k-ε model, is included here.

Assuming a one-dimensional, neutrally stratified and fully developed flow, momentum, k and ε equations (2.12, 2.17 and 2.18), within a dense horizontally homogeneous canopy are simplified as follows:

$$0 = \frac{d}{dz}\left(\nu_t \frac{dU}{dz}\right) - C_z U^2 \ , \tag{6.1}$$

$$0 = \frac{d}{dz}\left(\frac{\nu_t}{\sigma_k}\frac{dk}{dz}\right) + \nu_t \left(\frac{dU}{dz}\right)^2 - \varepsilon + S_k \ , \tag{6.2}$$

$$0 = \frac{d}{dz}\left(\frac{\nu_t}{\sigma_\varepsilon}\frac{d\varepsilon}{dz}\right) + C_{\varepsilon 1} C_\mu k \left(\frac{dU}{dz}\right)^2 - C_{\varepsilon 2}\frac{\varepsilon^2}{k} + S_\varepsilon \ , \tag{6.3}$$

where

$$S_k = \rho C_z \left(\beta_p \left|\mathbf{U}\right|^3 - \beta_d \left|\mathbf{U}\right| k\right), \tag{6.4}$$

$$S_\varepsilon = \rho C_z \left(C_{\varepsilon 4}\beta_p \frac{\varepsilon}{k}\left|\mathbf{U}\right|^3 - C_{\varepsilon 5}\beta_d \left|\mathbf{U}\right| \varepsilon\right) \ . \tag{6.5}$$

In a zone far enough away from a boundary, the mixing length

$$l_m = \frac{\alpha'}{C_z}, \tag{6.6}$$

is considered to be constant. The dimensionless coefficient is $\alpha' = 0.05$, as discussed by Massman (1997). Turbulent eddy viscosity can be defined as

$$\nu_t = l_m^2 \frac{dU}{dz}, \tag{6.7}$$

which replaced in (6.1), yields an exponentially decaying velocity profile, defined by

$$\frac{dU}{dz} = \frac{C_z}{(2\alpha'^2)^{\frac{1}{3}}} U. \tag{6.8}$$

Using this, and equating (6.7) to

$$\nu_t = C_\mu^{\frac{1}{4}} l_m k^{\frac{1}{2}}, \tag{6.9}$$

k follows as

$$k = \frac{\left(\frac{\alpha'}{2}\right)^{\frac{2}{3}}}{C_\mu^{\frac{1}{2}}} U^2. \tag{6.10}$$

From Kolmogorov's relation for high Reynolds number,

$$\varepsilon = C_\mu^{\frac{3}{4}} \frac{k^{\frac{3}{2}}}{l_m}, \tag{6.11}$$

we define ε as

$$\varepsilon = \frac{C_z}{2} U^3. \tag{6.12}$$

Using equation (6.8), the vertical derivatives of k and ε may also be written as functions of the longitudinal velocity:

$$\frac{dk}{dz} = \frac{C_z}{\sqrt{C_\mu}} U^2 \ , \tag{6.13}$$

$$\frac{d\varepsilon}{dz} = 3\frac{C_z^2}{(4\alpha')^{\frac{2}{3}}} U^3 \ , \tag{6.14}$$

and the terms in equations (6.2) and (6.3) can be replaced by

$$\frac{d}{dz}\left(\frac{\nu_t}{\sigma_k}\frac{dk}{dz}\right) = \frac{3}{\sigma_k}\left(\frac{\alpha'}{2}\right)^{2/3} \frac{C_z}{\sqrt{C_\mu}} U^3 \ , \tag{6.15}$$

$$\frac{d}{dz}\left(\frac{\nu_t}{\sigma_\varepsilon}\frac{d\varepsilon}{dz}\right) = \frac{3}{\sigma_\varepsilon} C_z^2 U^4 \ . \tag{6.16}$$

After replacing equations (6.15) and (6.4) into equation (6.2), we can establish the relation

$$\beta_d = \sqrt{C_\mu}\left(\frac{2}{\alpha'}\right)^{\frac{2}{3}}\beta_p + \frac{3}{\sigma_k}. \tag{6.17}$$

Similarly, substitution of equations (6.16) and (6.5) into equation (6.3) yields

$$C_{\varepsilon 5}\beta_d = \sqrt{C_\mu}\left(\frac{2}{\alpha'}\right)^{\frac{2}{3}}\left(C_{\varepsilon 4}\beta_p - \frac{C_{\varepsilon 2} - C_{\varepsilon 1}}{2}\right) + \frac{6}{\sigma_\varepsilon}. \tag{6.18}$$

Equations (6.17) and (6.18) obviously are not enough for determining the four coefficients β_p, β_d, $C_{\varepsilon 4}$ and $C_{\varepsilon 5}$.

6.2.2 Canopy Model Constants Based on k-ε-$\overline{v^2}$-f Model

In this work we propose a procedure based on the "code friendly" variant of the original k-ε-$\overline{v^2}$-f model (Laurence et al., 2004), where the two additional equations of $\overline{v^2}$-f, provide the framework for a more consistent and robust analytical determination of the canopy model constants. For full details on the k-ε-$\overline{v^2}$-f model formulation and its variants see e.g. Durbin (1991) and Laurence et al. (2004).

In addition to momentum, k and ε equation, the k-ε-$\overline{v^2}$-f model has a transport equation for $\overline{v^2}$,

$$\rho\frac{\partial \overline{v^2}}{\partial t} + \rho\frac{\partial U_j \overline{v^2}}{\partial x_j} = k\overline{f} - 6\overline{v^2}\frac{\varepsilon - S_{k\oplus}}{k^2} + \frac{\partial}{\partial x_j}\left(\frac{\nu_t}{\sigma_k}\frac{\partial \overline{v^2}}{\partial x_j}\right), \tag{6.19}$$

and an auxiliary equation for $\overline{f}$,

$$L^2\nabla^2\overline{f} - \overline{f} = \frac{C_{f1}}{T}\left(\frac{\overline{v^2}}{k} - \frac{2}{3}\right) - C_{f2}\frac{\mathcal{P}_k + S_{k\ominus}}{k} - 5\overline{v^2}\frac{\varepsilon - S_{k\oplus}}{k^2}, \tag{6.20}$$

where the turbulent time and length scales, T and L are defined by

$$T = \frac{k}{\varepsilon} \text{ and } L = C_L\frac{k^{3/2}}{\varepsilon}. \tag{6.21}$$

Equations (6.19) and (6.20) differ from the original (2.21) and (2.22) (Laurence et al., 2004); they present the canopy related terms $S_{k\oplus}$ and $S_{k\ominus}$. Being $\overline{v^2}$ a part of k, and looking into the equations of the $\overline{v^2} - f$ model we can imagine several ways to add the contribution of the canopy drag S_k from the k equation. For now, we will split this term in two parts, and later test the ones that conducted in any means to a possible physical solution:

$$S_k = S_{k\oplus} + S_{k\ominus}. \tag{6.22}$$

Based on the same assumptions as in section 6.2.1, in the case of equations (6.1), (6.2) and (6.3), but applied to equations (6.19) and (6.20),

$$\overline{f} = 6\overline{v^2}\frac{\varepsilon - S_{k\oplus}}{k^2} - \frac{1}{k}\frac{d}{dz}\left(\frac{\nu_t}{\sigma_k}\frac{d\overline{v^2}}{dz}\right) , \tag{6.23}$$

$$L^2\frac{d^2\overline{f}}{dz^2} - \overline{f} = \frac{C_{f1}}{T}\left(\frac{\overline{v^2}}{k} - \frac{2}{3}\right) - C_{f2}\frac{\mathcal{P}_k + S_{k\ominus}}{k} - 5\overline{v^2}\frac{\varepsilon - S_{k\oplus}}{k^2} , \tag{6.24}$$

where $\mathcal{P}_k = \nu_t\left(\frac{dU}{dz}\right)^2$.

The turbulent eddy viscosity is now defined as

$$\nu_t = C_\mu^*\overline{v^2}\frac{k}{\varepsilon} . \tag{6.25}$$

where C_μ^* is different from C_μ in k-ε model. After algebraic manipulation, using equations (6.10) and (6.12), equation (6.25) yields

$$\overline{v^2} = \left(\frac{\alpha'}{2}\right)^{\frac{2}{3}}\frac{\sqrt{C_\mu}}{C_\mu^*}U^2. \tag{6.26}$$

Applying the same procedures to the $\overline{v^2}$ transport equation, the $\overline{v^2}$ diffusion term in equation (6.23) now reads

$$\frac{d}{dz}\left(\frac{\nu_t}{\sigma_k}\frac{d\overline{v^2}}{dz}\right) = \frac{3}{\sigma_k}\left(\frac{\alpha'}{2}\right)^{2/3}\frac{C_z\sqrt{C_\mu}}{C_\mu^*}U^3 . \tag{6.27}$$

Before that, we are going to deal with the canopy terms $S_{k\oplus}$ and $S_{k\ominus}$. These two terms can be imaginatively distributed to add/subtract the standard production and dissipation terms of the model equations or, conversely, treated in a single term (making one of them equal to zero). It was also found that the particular way to add these terms to the model equations depended on the choice of the non-canopy model constants. Later, from these several possible approaches to incorporate the canopy terms on the $\overline{v^2} - f$ equations, the ones that conducted in any means to a possible physical solution, all used the splitting of the S_k term in two contributions, as

$$S_{k\oplus} = \rho C_z\beta_p\left|\mathbf{U}\right|^3 , \tag{6.28}$$

$$S_{k\ominus} = -\rho C_z\beta_d\left|\mathbf{U}\right|k . \tag{6.29}$$

A new relation between β_p and β_d, was obtained from replacing the definitions (6.26) and (6.27) in equations (6.23) and (6.24). After proper simplifications[1] led to,

$$\beta_d = \frac{\left(\frac{2}{\alpha'}\right)^{\frac{2}{3}}C_\mu^{\frac{3}{2}} + 6C_L^2}{C_{f2}C_\mu^*}\beta_p + K_3. \tag{6.30}$$

[1]The algebraic and differential manipulation of those equations was made with the help of *Maple 9.5*$^{\text{TM}}$ software.

where

$$K_3 = \sqrt{C_\mu}\left(\frac{2}{\alpha'}\right)^{\frac{2}{3}} \frac{C_{f1}\left(\frac{2}{3}C_\mu^* - C_\mu\right) + C_{f2}C_\mu^* - C_\mu}{2C_{f2}C_\mu^*} + \frac{3\left(C_\mu + C_L^2 - \frac{C_L^2}{\sqrt{C_\mu}\left(\frac{2}{\alpha'}\right)^{\frac{2}{3}}}\right)}{C_{f2}C_\mu^*}, \quad (6.31)$$

is a constant. Equation (6.30) with equation (6.17) allows us to explicitly determine β_p and β_d.

These additional relations provided by the k-ε-v^2-f model are not influenced by the ε equation and so there is no way to establish additional information for the determination of $C_{\varepsilon 4}$ and $C_{\varepsilon 5}$. Because of that we have used the assumption $C_{\varepsilon 4} = C_{\varepsilon 5}$, as in Sanz (2003), where,

$$C_{\varepsilon 4}\,(= C_{\varepsilon 5}) = \sigma_k \left[\frac{2}{\sigma_\varepsilon} - \frac{C_\mu^{1/2}}{6}\left(\frac{2}{\alpha'}\right)^{2/3}(C_{\varepsilon 2} - C_{\varepsilon 1})\right]. \quad (6.32)$$

6.3 RANS Constants

Because the canopy model constants are dependent of the choice of the k-ε-$\overline{v^2}$-f turbulent model constants, it is important chose the most adequate turbulence model constants to use on RaNS canopy flow simulations.

6.3.1 Standard and atmospheric constants

We began by considering two constant sets, based on the k-ε "standard constants" and on the k-ε "atmospheric constants", as presented on table 6.1 ("Constant set 1" and "Constant set 2"). The $\overline{v^2}$-f group of constants were those proposed by Laurence et al. (2004): $C_{f1} = 0.4$, $C_{f2} = 0.3$ and $C_L = 0.23$, that we will call in this work $\overline{v^2}$-f "standard constants". This choice was based on the available literature, and was an first approach to test the canopy model. Some LES and RaNS calculations of channel flow without canopy were carried on in order to choose the most adequate set of RaNS constants. We presumed that those constants must also be the most suitable for the flow over canopy. The results are presented on figures 6.1 and 6.2.

Table 6.1: Constant sets used in the k-ε model (excluding $\overline{v^2}$-f constants) and k-ε-$\overline{v^2}$-f model.

	k-ε constants					$\overline{v^2}$-f constants			
	C_μ	σ_k	σ_ε	$C_{\varepsilon 1}$	$C_{\varepsilon 2}$	C_μ^*	C_L	C_{f1}	C_{f2}
Constant set 1	0.033	1.0	1.85	1.44	1.92	0.22	0.23	0.40	0.30
Constant set 2	0.09		1.11						
Constant set 3								0.13	0.12
Constant set 4							0.25	0.027	0.10

Constant set 1 - Atmospheric k-ε and Standard $\overline{v^2}$-f constants.

Constant set 2 - Standard k-ε and Standard $\overline{v^2}$-f constants.

Constant set 3 - Standard k-ε and $\overline{v^2}$-f Wall Function Corrected constants.

Constant set 4 - Standard k-ε and $\overline{v^2}$-f Wall Function Corrected and Tuned constants.

6.3.2 k-ε simulations

Calculations were made using RaNS k-ε model, testing the first two sets of constants in table 6.1 (only left side). Both horizontal velocity profiles were identical to the one obtained by LES (figure 6.1). On the other hand, the TKE profiles were quite different. Both results over-estimated k and failed to reproduce the peak of TKE near the ground (figure 6.1), with the standard constants set closer to LES results.

6.3.3 k-ε-$\overline{v^2}$-f simulations

The k-ε-$\overline{v^2}$-f model was also tested, considering the to cases of "Constant set 1" and "Constant set 2" (figure 6.2).

Regarding the velocity profiles, the k-ε-$\overline{v^2}$-f results are almost the same and, in comparison with k-ε results, in poorer agreement with the LES results.

In terms of TKE profiles, the results were similar to those obtained by k-ε atmospheric constants. Using the laboratory k-ε-$\overline{v^2}$-f constants set, the k profile was closer to LES profile than any previous RaNS results, namely in the near-wall region. The ability to describe the asymptotic trend of the LES k profile by the $\overline{v^2}$-f model was not observed in the standard k-ε model results. The standard k-ε model results of k are better described saying that they follow an almost linear decay with height (figure 6.1).

However, the $\overline{v^2}$-f model constants tuning was later made, imposing

$$\beta = \kappa^2, \tag{6.33}$$

where κ is the Von Karmann constant and β is defined (P. A. Durbin, personal communi-

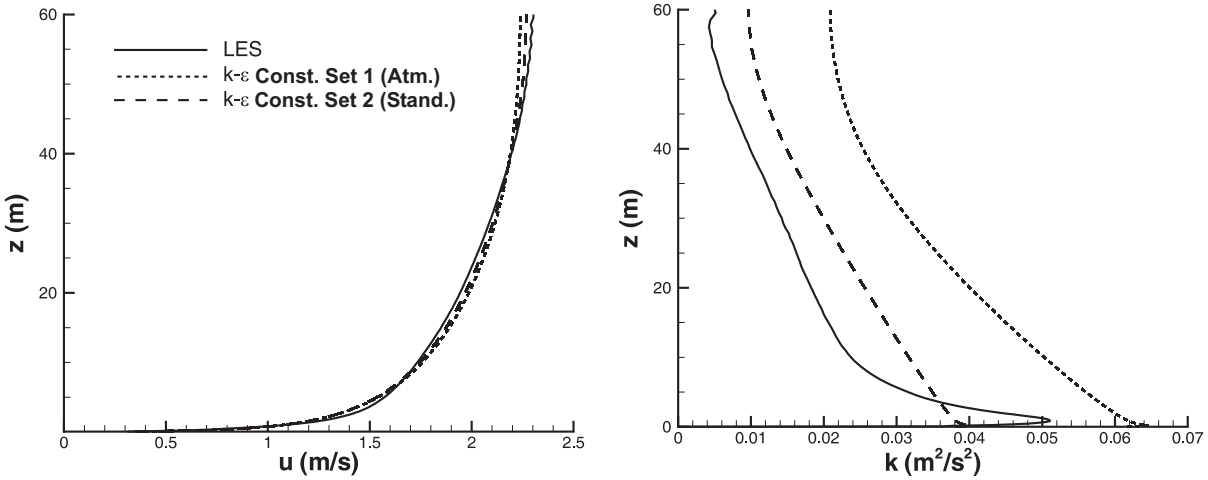

Figure 6.1: No canopy k-ε model results compared with LES. Vertical horizontal velocity and TKE profiles.

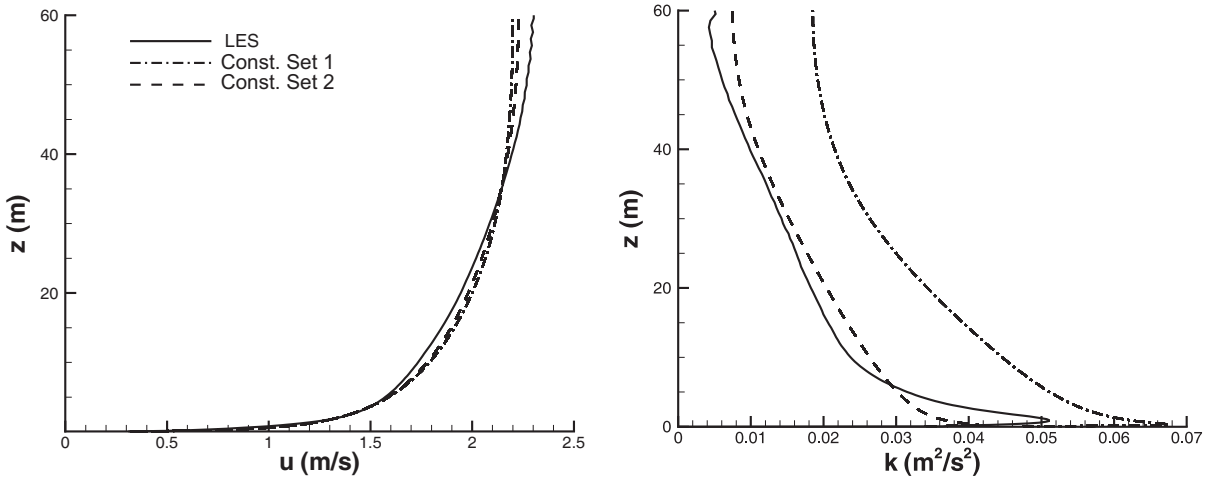

Figure 6.2: No canopy k-ε-$\overline{v^2}$-f model results compared with LES. Vertical horizontal velocity and TKE profiles.

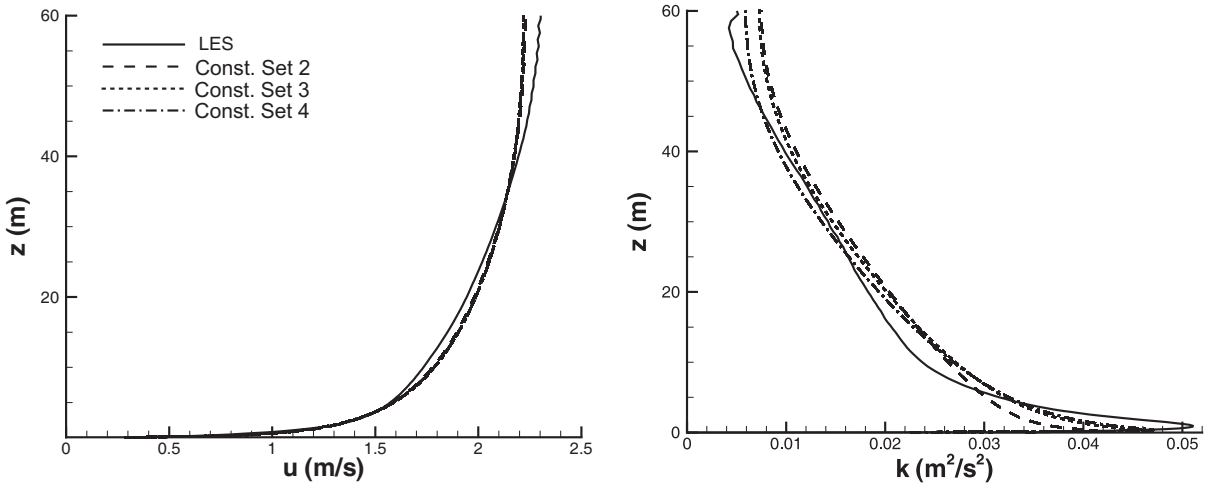

Figure 6.3: No canopy k-ε-$\overline{v^2}$-f model results compared with LES, using new model constants. Vertical horizontal velocity and TKE profiles.

cation) as

$$\beta = \sqrt{\frac{C_\mu \alpha''^2}{1+C_{f1}}\left(\frac{2}{3}C_{f1}+C_{f2}+\frac{2\alpha'' C_L^2}{C_\mu^*}\right)}, \tag{6.34}$$

$$\alpha'' = \sigma_\varepsilon\left(C_{\varepsilon 2}-C_{\varepsilon 2}\right). \tag{6.35}$$

The relationship (6.33) is obtained by applying the near-wall turbulent viscosity definition

$$\nu_t = \kappa u^* z \tag{6.36}$$

to the turbulent near wall viscosity definition used in the k-ε-$\overline{v^2}$-f model with wall functions (P. A. Durbin, personal communication)

$$\nu_t = \beta \frac{u^*}{\kappa} z. \tag{6.37}$$

Based on relation (6.33), the laboratory constants and $C_L = 0.23$, yields: $C_{f1} = 0.13$ and $C_{f2} = 0.12$. This set of constants is detailed in table 6.1, as "Constant set 3".

As we may observe on figure 6.3, this tuning produces a non negligible improve on k vertical profile, mainly attending to its shape near the ground.

Some other numerical experiments were made, in order to replicate the turbulent kinetic energy predicted by LES, but always imposing relation (6.33). Because C_L increases the k profile convexity, another set of tuned constants was used, also in table 6.1 ("Constant set 4"), which further improved the agreement with the LES results.

Table 6.2: Canopy model constant sets.

Canopy Model	RaNS constant sets	β_p	β_d	$C_{\varepsilon 4} = C_{\varepsilon 5}$
CM1	Constant set 1	0.17	3.37	0.9
CM2	Constant set 2	0.785	5.76	1.52
CM3	Constant set 3	2.18	10.65	1.52
CM4	Constant set 4	1.62	8.70	1.52

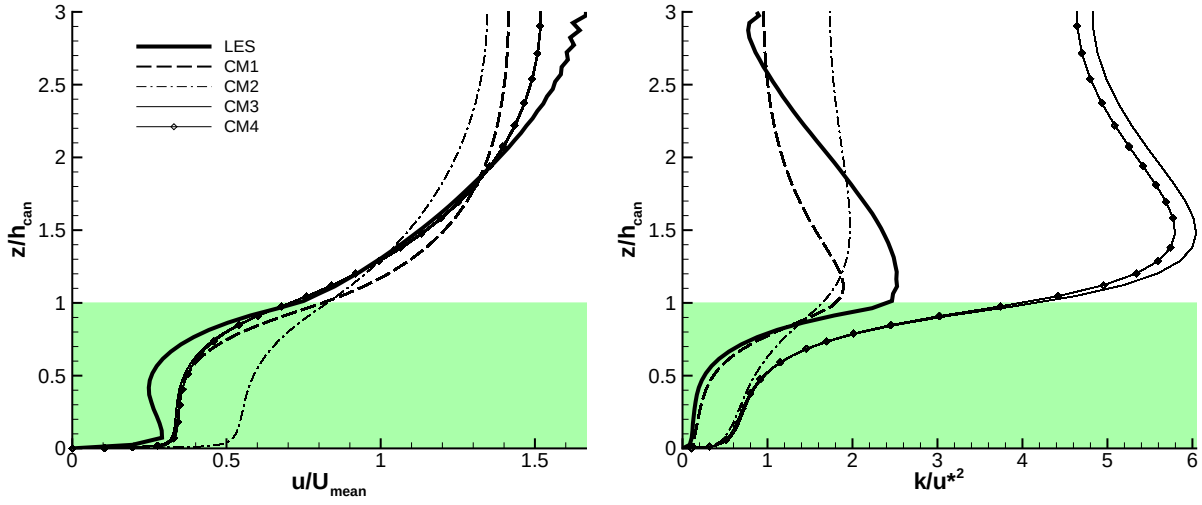

Figure 6.4: Velocity and TKE profiles for table 6.2 canopy models using k-ε-$\overline{v^2}$-f turbulence model.

6.4 Canopy model with new RaNS constants

As shownd in section 6.2, the canopy model constants, β_p, β_d, $C_{\varepsilon 4}$ and $C_{\varepsilon 5}$, depend on RaNS k-ε-$\overline{v^2}$-f model constants. In the previous section we tested several turbulence model constant sets, focusing on the four sets described on table 6.1. These four sets were used to found other four canopy model constant sets, as presented in table 6.2.

6.4.1 k-ε-$\overline{v^2}$-f simulations

RaNS k-ε-$\overline{v^2}$-f calculations where made using those canopy models, with the correspondent model constants.

The CM3 and CM4 constant sets, followed by CM1, present a better accordance with LES velocity profiles (figure 6.4). Meanwhile, CM2 fails completely in this matter. On

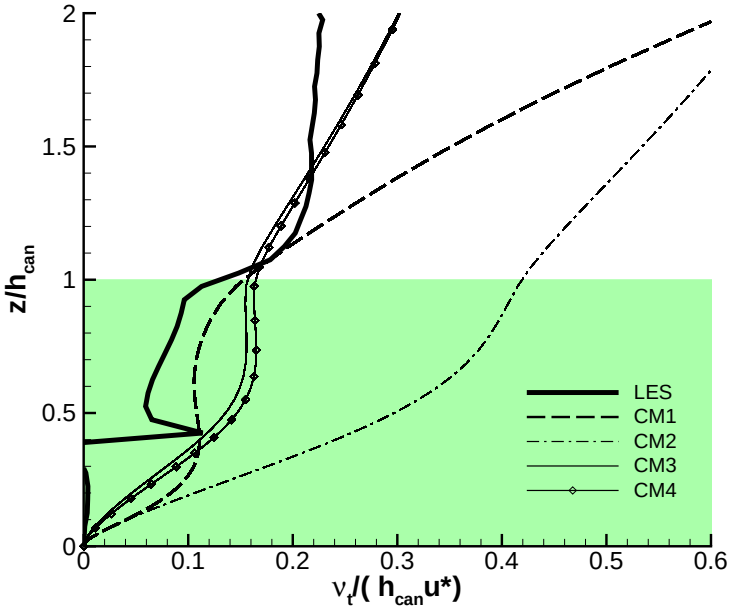

Figure 6.5: Turbulent viscosity profiles for table 6.2 canopy models using k-ε-$\overline{v^2}$-f turbulence model.

the other hand, TKE values are much higher with CM3 and CM4 than CM1, which is relatively close to LES results.

Regarding the turbulent viscosity profiles (figure 6.5), the increase above the canopy of CM1 is now much controlled with CM3 and CM4. CM2 over-predicts the turbulent viscosity. From those graphs, we may conclude that the adjustments by equation (6.33) produced the best velocity and turbulent viscosity profiles. The TKE profiles for CM3 and CM4 presented a similar trend to the LES results but with exaggerated magnitude.

6.4.2 k-ε simulations

In the next step, we have also tested the canopy model constants CM1, CM2, CM3 and CM4 on the standard k-ε turbulence model.

As we may observe, with k-ε turbulence model, CM2, CM3 and CM4 results completely failed (figures 6.6 and 6.7). Velocity, TKE and turbulent viscosity profiles were almost insensitive to the the canopy model constants. The main difference between CM1 and the others canopy model constant sets is the value of $C_{\varepsilon 4}$ (or $C_{\varepsilon 5}$), and based on

$$C_{\varepsilon 4}\,(=C_{\varepsilon 5}) = \sigma_k \left[\frac{2}{\sigma_\varepsilon} - \frac{C_\mu^{1/2}}{6} \left(\frac{2}{\alpha'} \right)^{2/3} (C_{\varepsilon 2} - C_{\varepsilon 1}) \right], \tag{6.32}$$

we can see that these canopy constants depend exclusively on k-ε model constants. This

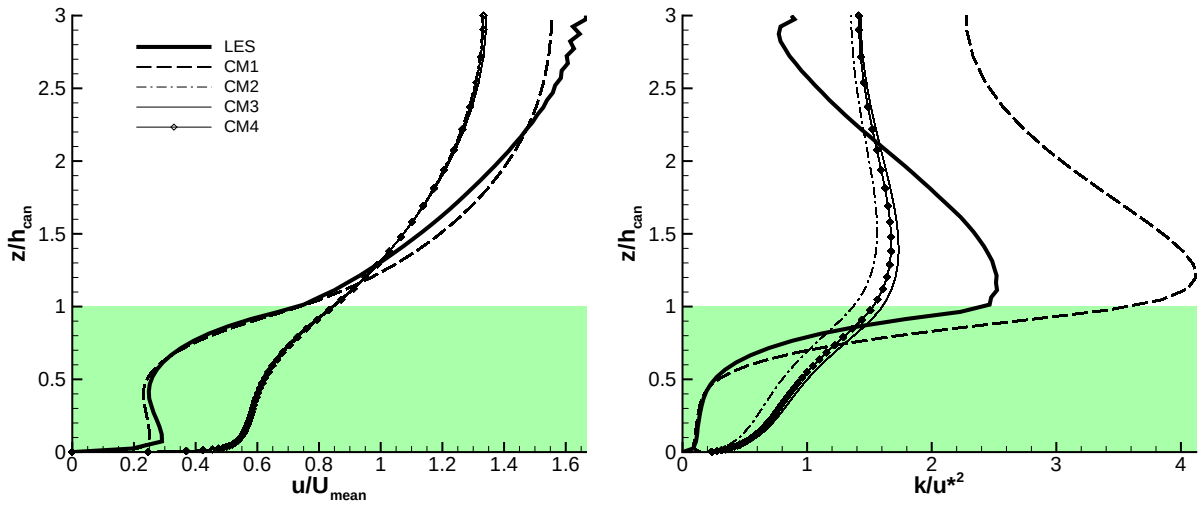

Figure 6.6: Velocity and TKE profiles for table 6.2 canopy models using k-ε turbulence model. Comparison with LES.

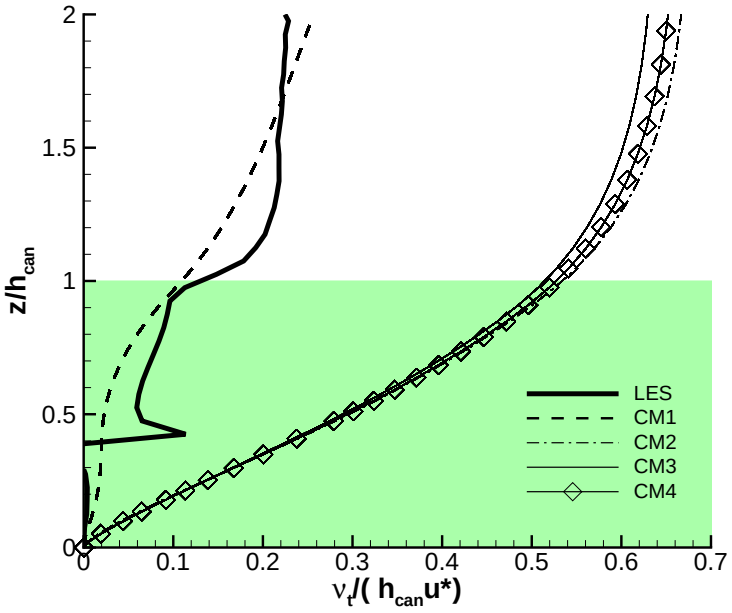

Figure 6.7: Turbulent viscosity profiles for table 6.2 canopy models using k-ε turbulence model. Comparison with LES.

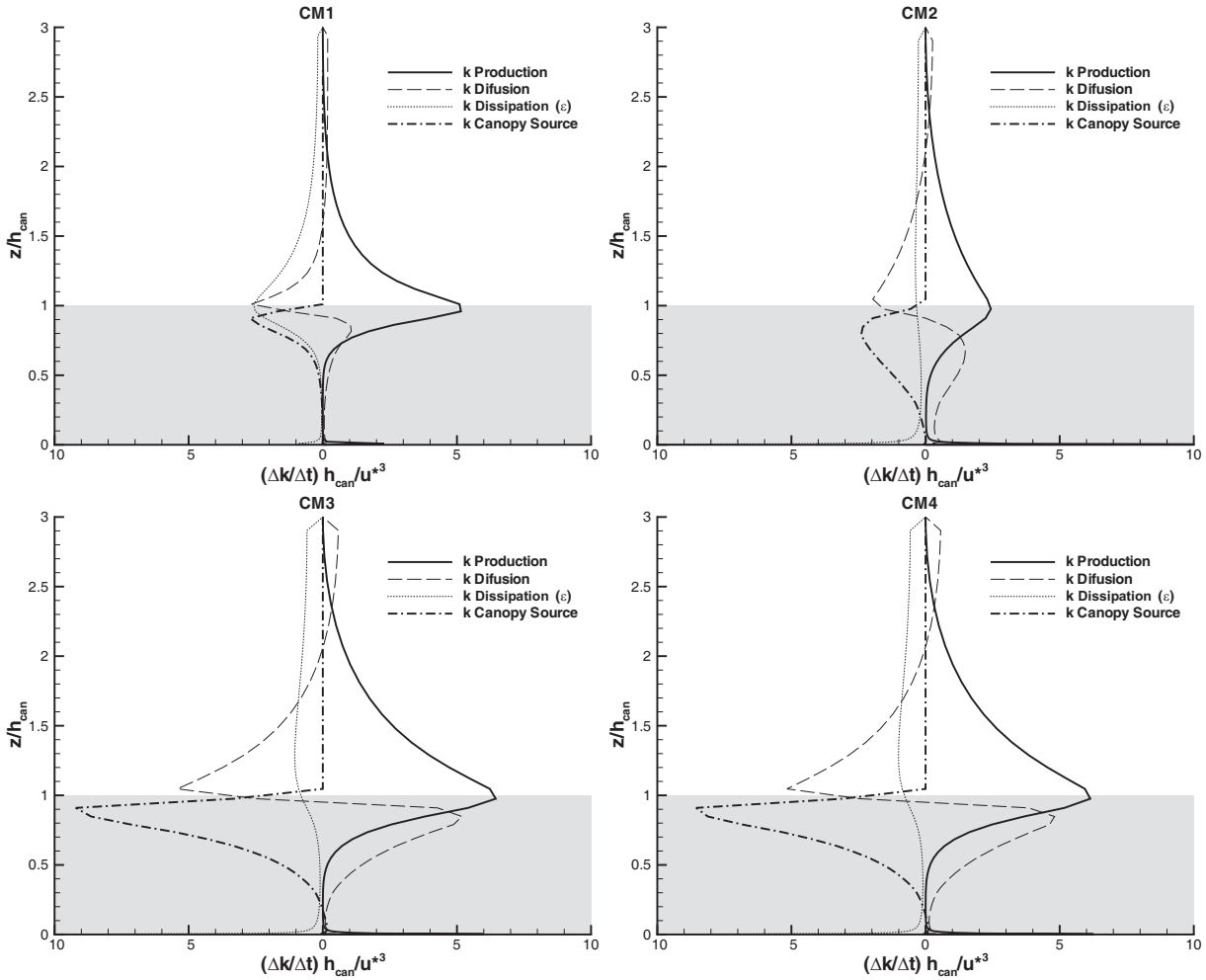

Figure 6.8: TKE budget terms of RaNS k-ε-$\overline{v^2}$-f with table 6.2 canopy models calculations.

suggests that somehow, the atmospheric k-ε constant set, the basis for the $C_{\varepsilon 4}$ and $C_{\varepsilon 5}$ values in CM1, are more suitable to simulate flows over canopy, contrary to the case of a flow over a flat rough surface without canopy, where the standard k-ε constants appeared to be superior.

These results also showed the importance of the constants $C_{\varepsilon 4}$ and $C_{\varepsilon 5}$, that were not very much explored in this work, namely the possibility of consider $C_{\varepsilon 4} \neq C_{\varepsilon 5}$.

6.4.3 Turbulent kinetic energy (TKE) budgets

In figures 6.8 and 6.9 the vertical profiles of the budget terms of the TKE equation for the previous calculations are presented: RaNS k-ε-$\overline{v^2}$-f and k-ε with the four canopy models, as described in table 6.2.

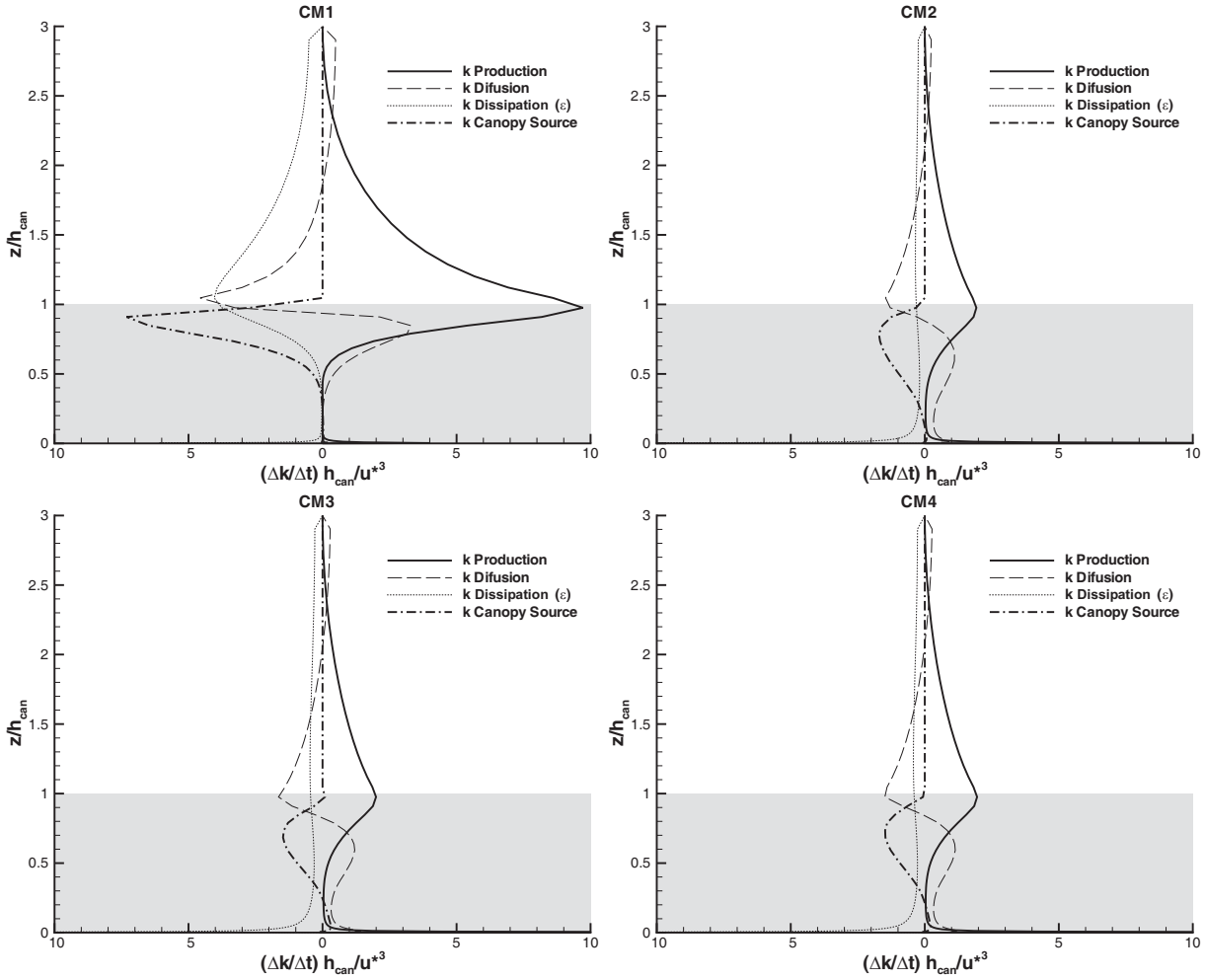

Figure 6.9: TKE budget terms of RaNS k-ε with table 6.2 canopy models calculations.

Table 6.3: Complete CM1 constants set used in RaNS calculation.

	k-ε constants					$\overline{v^2}$-f constants				Canopy model constants		
	C_μ	σ_k	σ_ε	$C_{\varepsilon 1}$	$C_{\varepsilon 2}$	C^*_μ	C_L	C_{f1}	C_{f2}	β_p	β_d	$C_{\varepsilon 4} = C_{\varepsilon 5}$
CM1	0.033	1.0	1.85	1.44	1.92	0.22	0.23	0.40	0.30	0.17	3.37	0.9

In the figure 6.8, on CM3 and CM4, we may observe that the canopy TKE negative term is largely exaggerated, which is compensated by a large term of positive diffusion inside the canopy zone. On the other and, ε term became smaller, much like the LES ε term (figure).

In the figure 6.9, the CM2, CM3 and CM4 TKE terms profiles seemed coarse representations of the same LES graphs. On the other hand, CM1 terms profiles are very similar to LES, in shape and intensity.

It is clear that CM1 presents the better results, using RaNS k-ε or k-ε-$\overline{v^2}$-f turbulence model. In the next section, we will compare CM1 canopy model constant set with LES results and with Sanz (2003) canopy model constant set, that we have concluded to be the the best canopy model found on published literature.

6.5 Comparing New Canopy Model Constants Set with Sanz (2003) Model

In the previous section, we showed that the best results were obtained in the case of the canopy model constants called CM1 (table 6.3). This model results are now compared with the Sanz (2003) canopy model results, using LES as a reference.

Velocity and turbulent kinetic energy are normalized both by the mean velocity, U_{mean}, and by the friction velocity at canopy heigh, u^*.

When it is applied to k-ε turbulence model, the new canopy model constants (called CM1) produces velocity profiles that appear to match to a large extent the LES results, even better than "Sanz CM" result. In the case of the k-ε-$\overline{v^2}$-f turbulence model, the velocity profile presents high values inside the canopy.

The TKE profiles, based on CM1 with k-ε turbulence model presents the best agreement with LES results of all the canopy models discussed previously, specially inside the canopy (see Chapter 5). With k-ε-$\overline{v^2}$-f turbulence model, CM1 also produces a k/U^2_{mean} profile more consistent with LES results than most of the other canopy models; however above the canopy there is a deficit of TKE.

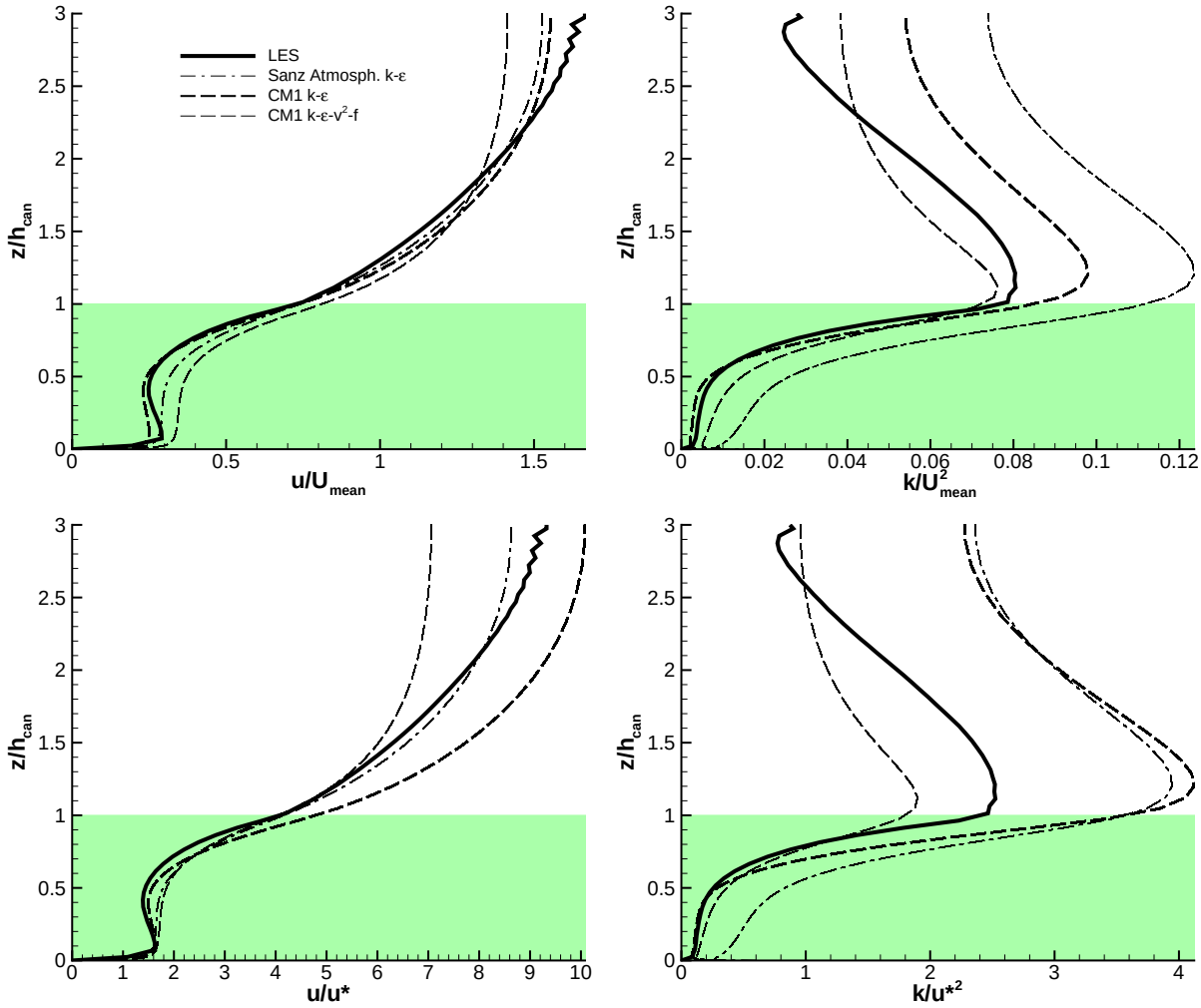

Figure 6.10: Velocity and TKE profiles for CM1 using k-ε or k-ε-$\overline{v^2}$-f turbulence model. Comparison with LES and "Sanz CM" results. Values normalised by canopy height, h_{can}, and mean velocity, U_{mean}, or friction velocity at canopy height, u^*.

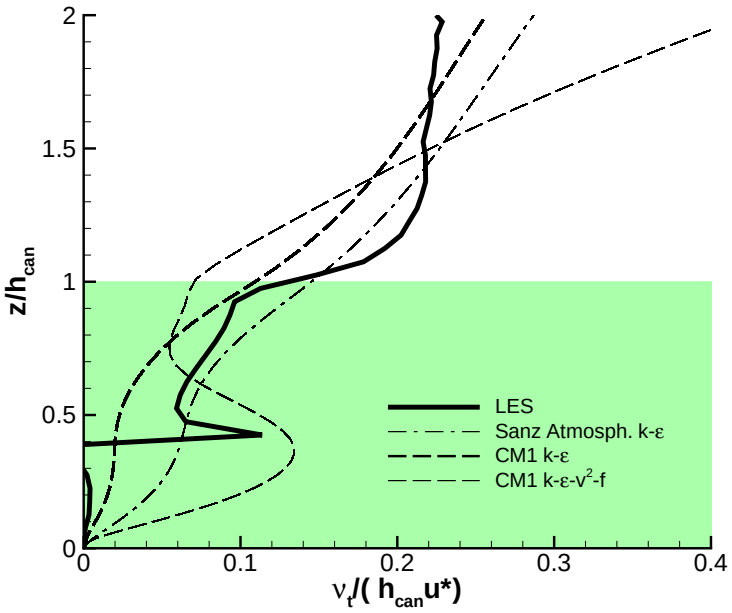

Figure 6.11: Viscosity profiles for CM1 using k-ε or k-ε-$\overline{v^2}$-f turbulence model. Values normalised by canopy height, h_{can}, and friction velocity at canopy height, u^*.

The turbulent viscosity profiles (figure 6.11) of CM1 with k-ε turbulence model shows a trend identical to "Sanz CM". With k-ε-$\overline{v^2}$-f turbulence model, turbulent viscosity is close to LES viscosity profile inside and near the canopy, but outside the canopy it increases sharply. The k-ε-$\overline{v^2}$-f turbulence model also works well inside and at the near vicinity of the canopy, but fails above it, over-predicting the turbulent viscosity.

Regarding the TKE budget terms (figures 6.12 and 6.13), we may observe that with the new canopy model constants on a k-ε turbulence model, the magnitude of the TKE terms is much similar to those obtained with LES (much better than "Sanz CM"), with the exception of the ε profile, which reach much higher values than LES. This problem is common to all RaNS results. On the other hand, the k-ε-$\overline{v}^2$-f turbulence model yields TKE terms profiles very similar to "Sanz CM", thought in a different scale, and also presenting a relatively high ε term.

Once again, the new constant set for the canopy model CM1 proves to have a better performance, mainly when used on a RaNS k-ε turbulence model. The use of the k-ε turbulence model, instead of the k-ε-$\overline{v}^2$-f turbulence model, has also the advantage of being a quicker and less computationally demanding. This is most convenient, in applications of this model on RaNS simulations over complex orography, where it is difficult and inadequate to implement the k-ε-$\overline{v}^2$-f turbulence model.

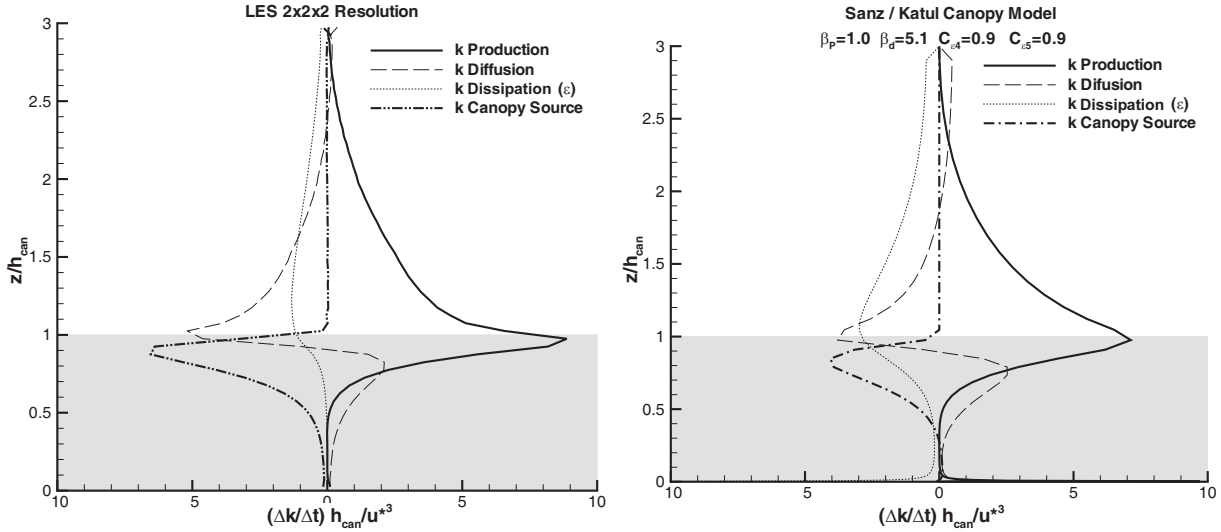

Figure 6.12: TKE budget terms for LES and RaNS calculation with "Sanz canopy model". Values normalised by canopy height, h_{can}, and friction velocity at canopy height, u^*.

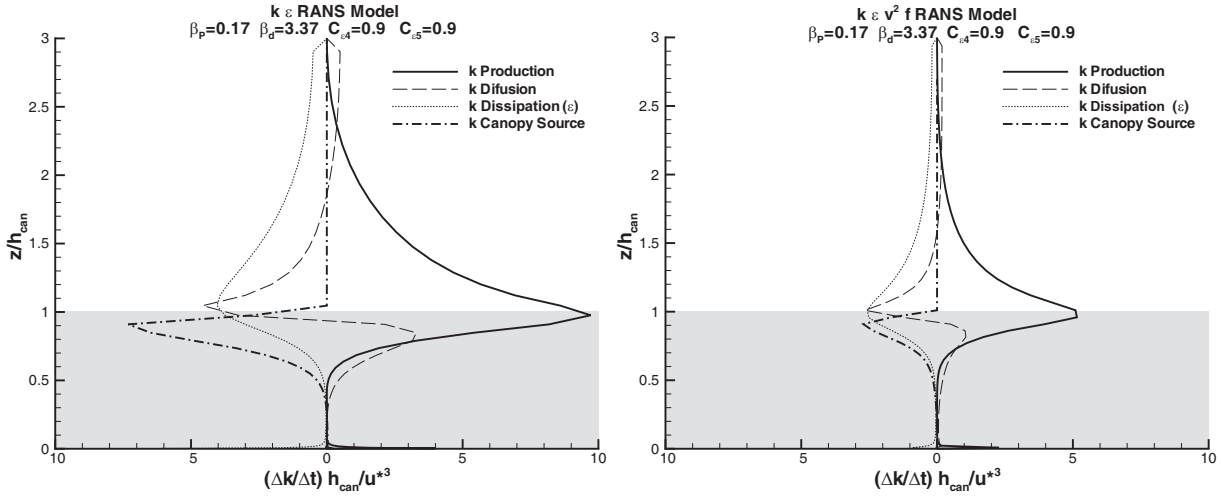

Figure 6.13: RaNS calculations: TKE budget terms for CM1, with k-ε and k-ε-$\overline{v^2}$-f turbulence model. Values normalised by canopy height, h_{can}, and friction velocity at canopy height, u^*.

6.6 Flow across a forest clearing

We also tested CM1 using a periodical canopy zone and RaNS k-ε turbulence model. The calculations procedures were the same presented in section 5.3.1, and its results are compared with LES and the best published canopy model chosen on Chapter 5, Sanz (2003).

6.6.1 Results

The results are presented on figures 6.14, 6.15 and 6.16. We compare LES, with RaNS k-ε atmospheric constants, using Sanz CM and our CM1 constants.

As it was shown in Chapter 5, RaNS models have a slower response to the appearing canopy, regarding LES results. The differences on the velocity fields (figure 6.14) are most obvious inside the canopy, and CM1 has the fastest response to the appearing canopy (figure 6.16), with the velocity contour more similar to LES.

The main differences between CM1 and Sanz CM were found in the TKE results (figure 6.15). LES produces lower TKE than the predicted by the RaNS models, but CM1 present the closer k values to LES. The LES field also shows that inside the canopy TKE is attenuated, whereas the mixing layer above the canopy acts as a TKE producer. This higher TKE region extends out far beyond the canopy zone. Regarding the RaNS results, the canopy models reacted slowly to the canopy, and over-predicted the TKE values. Once again, CM1 presents a closer behaviour to LES than Sanz CM.

Regarding the velocity and TKE representation of the flow across forest limits, when compared with LES applied to the same conditions, we might conclude the follow: although Sanz CM proved to be the best RaNS canopy model, when compared with other canopy models found on the literature, better results can be obtained using the CM1 constant set.

6.7 Conclusions

The computer simulation of the flows over both a homogeneous forest and forest clearing, showed the following:

1. The constant set named CM1, used under k-ε turbulence model, fielded the best agreement with the benchmark LES of the same flow. The complete constant set is the following:

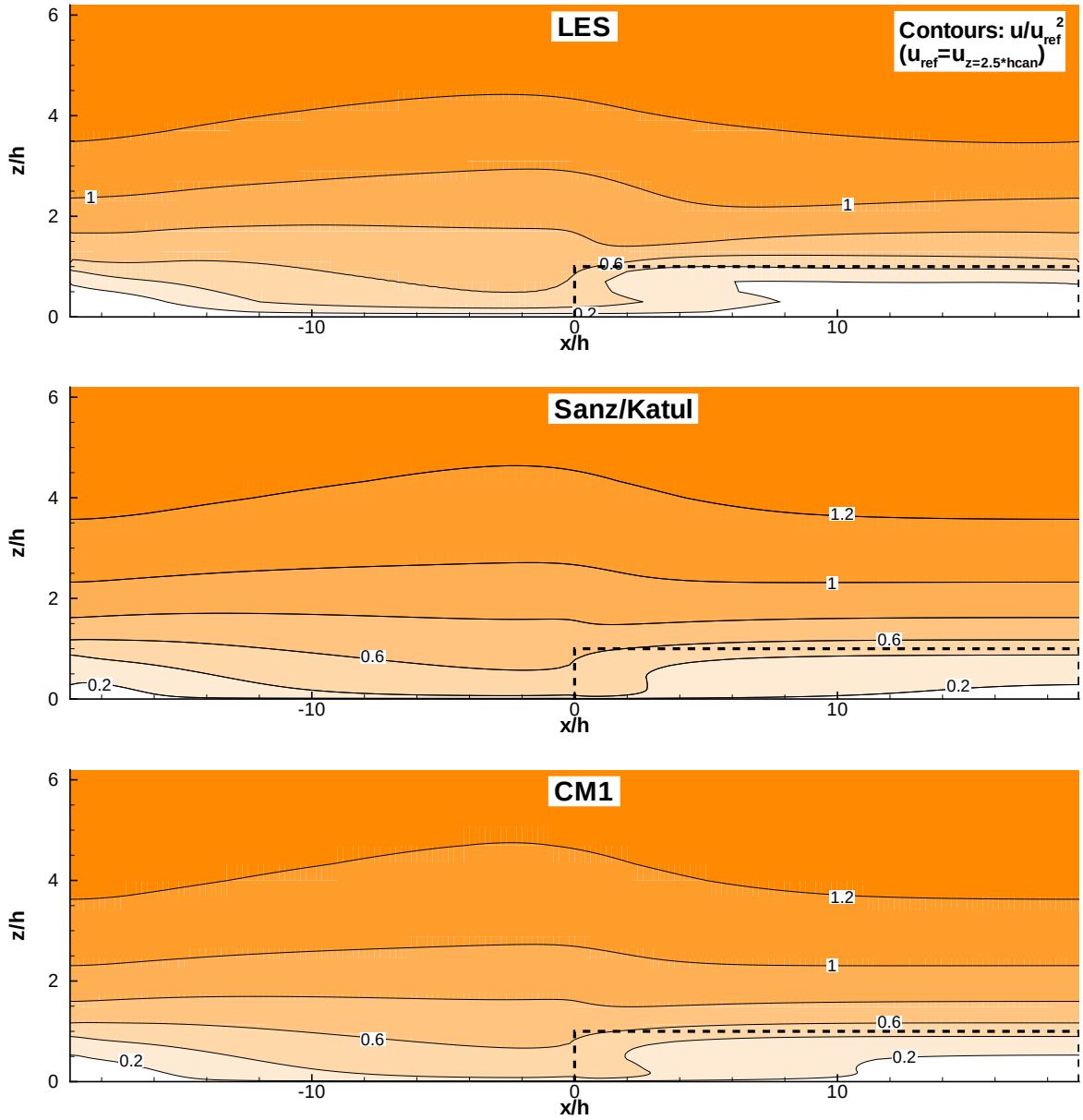

Figure 6.14: Longitudinal velocity contours, on a longitudinal section of the domain for LES, "Sanz canopy model" and CM1. Values normalised by u_{ref}, i. e., space average longitudinal velocity at $z = 2.5h_{can}$.

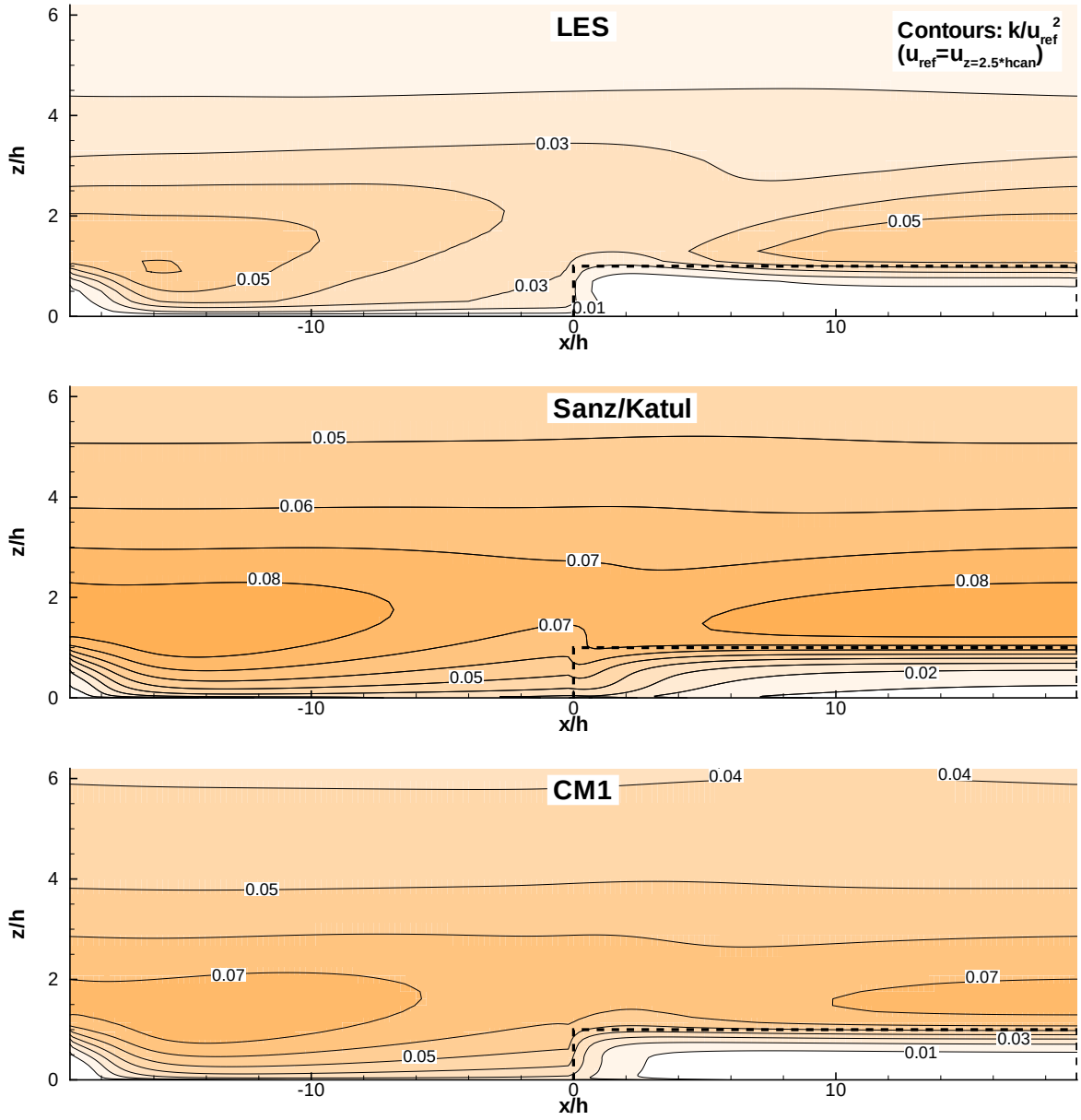

Figure 6.15: Turbulent kinetic energy contours, on a longitudinal section of the domain for LES, "Sanz canopy model" and CM1. Values normalised by u_{ref}, i. e., space average longitudinal velocity at $z = 2.5h_{can}$.

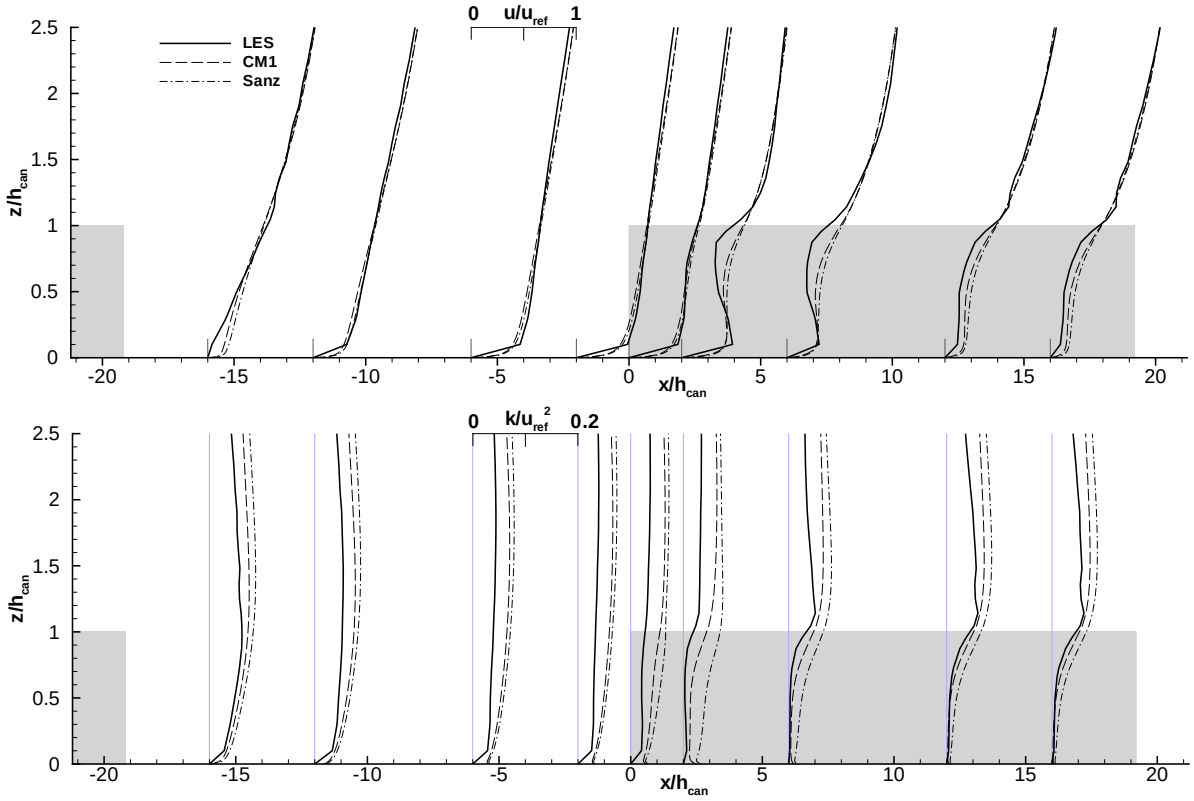

Figure 6.16: Velocity and turbulent kinetic energy profiles, on a longitudinal section of the domain. Values normalised by u_{ref}, i. e., space average longitudinal velocity at $z = 2.5h_{can}$.

	k-ε constants					Canopy model constants		
	C_μ	σ_k	σ_ε	$C_{\varepsilon 1}$	$C_{\varepsilon 2}$	β_p	β_d	$C_{\varepsilon 4} = C_{\varepsilon 5}$
CM1	0.033	1.0	1.85	1.44	1.92	0.17	3.37	0.9

2. The new canopy model constants CM1 present also better results than the "Sans CM".

3. It was established a new procedure to obtain relations between the canopy model constants β_p and β_d, using the k-ε-$\overline{v^2}$-f turbulence model equations. This procedure allowed us to obtain the CM1 constants.

4. Although it uses RaNS k-ε-$\overline{v^2}$-f formulation, its constants applied to the k-ε turbulence model improve the "Sans CM" results regarding velocity and TKE vertical distribution. Peculiarly, a combination of atmospheric (for k-ε) and laboratory (for $\overline{v^2}$-f) RaNS turbulence model constants produce a better canopy constants set for this matter. We have named this constant set as CM1.

5. The use of CM1 in the k-ε-$\overline{v^2}$-f turbulence model brings no significant improvement to canopy model results. In addition, it implies a larger calculation time. It must be remarked that k-ε-$\overline{v^2}$-f calculations were very hard to master numerically, and consumed important computational effort and time. On the other hand, RaNS k-ε calculations were much easy to implement and numerically converge to a solution much quicker than a k-ε-$\overline{v^2}$-f calculation.

6. For the horizontal continuous canopy, the CM1 constants applied to the k-ε turbulence model yields the better agreement with the k equations terms behaviour obtained by LES. The exception was the ε profile, which reach much higher values than LES. However, a relatively high ε profile is common to all RaNS results.

Final Note

When the writing up of the present dissertation was near completion, the study by Dupont and Brunet (2007) came to our knowledge. This is a piece of work similar to the contents of the present chapter - a study of the flow over both homogeneous canopies and forest clearings, using LES - against which our results should also be compared. At this point and to avoid changes within the body of text of the present chapter, we note that Dupont and Brunet (2007) also analyse various canopy vertical distributions and their effects on the so-called enhanced gust zone, characterized by both intense and intermittent wind gusts and to be found immediately after and above the beginning of the forest. There is a great similarity between ours and theirs results, namely the contours of turbulence kinetic distribution, which reinforces our confidence in the results and the conclusions of the present chapter.

Depending on a more detailed analysis, the study by Dupont and Brunet (2007) might provide the basis for future tests of CM1 canopy model constants.

Chapter 7

Revisiting the French Case

Abstract

The computer simulation of the wind flow over a forested region in the south of France was revisited, applying the CM1 canopy model constant set.

Slight improvements were found, and the main differences between CM1 and "Svensson CM" (previously used) were observed for heights *agl* equal to 3 canopy heights. The available field measurements were made relatively far above the canopy zone. This precluded a deeper analysis of the differences between the two canopy models.

The effect of the forest effects on turbulence to higher altitudes and downstream was studied. The relatively high TKE values at higher distances *agl* could not be predicted by the 'Svensson CM" nor the CM1, and it was found that this was due to the higher turbulence values at the domain inlet, associated to forested regions upstream the studied location, outside and inside the integration domain. Improved agreement with the field data was achieved via a well justified higher turbulence intensity as an inlet condition, along with

7.1 Introduction

In Chapter 4, the Svensson and Häggkvist (1990) canopy model proved to be adequate in the computer simulation of the wind flow over complex orography with forested areas. However, Chapter 5 showed the failure of the Svensson and Häggkvist (1990) to mimic the turbulence mechanisms, compared to other models. Later, on Chapter 6, new canopy model parameters were tuned to be applied in these models.

At this point, and also as a way of bringing the present study to an end, it was decided

to see whether the computer simulation of the French case in Chapter 4 could be improved, namely the turbulence profiles. The calculations presented in Chapter 4 were repeated here, but using the canopy model formulation, based on the CM1 parameters as in Chapter 6.

7.2 Model and Numerical Parameters

The numerical meshes and canopy geometrical definitions were identical to those described in section 4.3.2. Calculations were restricted to four wind quadrants: 120, 150, 300 and 330 degrees, with a friction velocity equal to 0.6 ms^{-1}. The canopy characteristics considered were a tree height h of 15 m, a density foliage equal to 0.125 m^2m^{-3} and a drag coefficient C_D equal to 0.25. The CM1 model parameters were used, as in Chapter 6: $\beta_p = 0.17$, $\beta_d = 3.37$, and $C_{\varepsilon 4} = C_{\varepsilon 5} = 0.9$.

7.3 Results

The results obtained with the CM1 coefficients determined in Chapter 6 will be compared with results of the canopy model as in Chapter 4 ("Svensson CM" - Svensson and Häggkvist (1990)) for the same canopy parameters.

7.3.1 North-Westerly winds (330° and 300°)

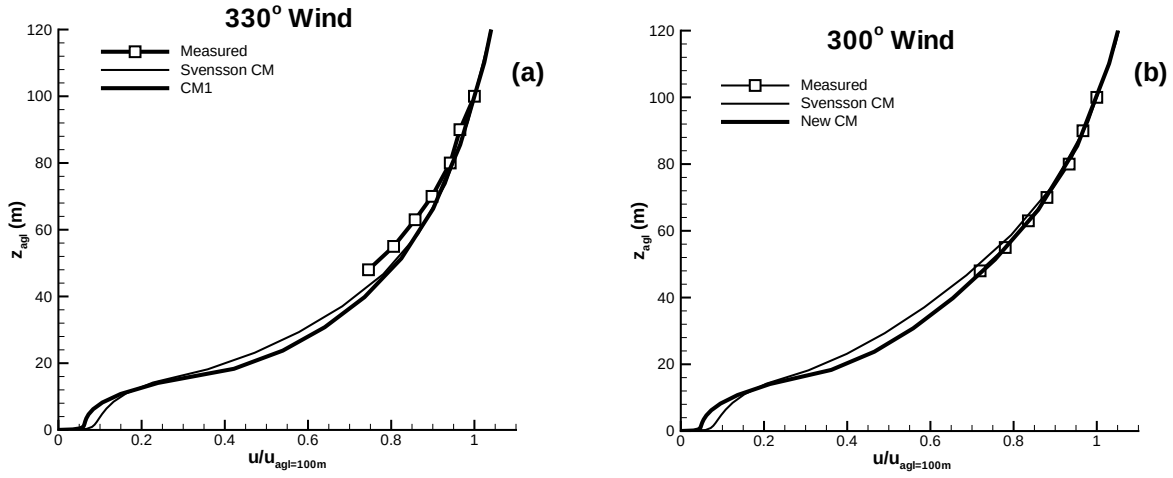

Figure 7.1: Velocity profiles at mast M208, in the case of 330° (a) and 300° (b) winds.

For the 330º and 300º wind directions (Figure 7.1), the horizontal velocity obtained with CM1 are in good agreement with the field data. It was difficult to improve the results in Chapter 4, which were already good, but nevertheless for 300º wind direction, the CM1 results were able to improve even further the agreement with field data.

The results for the horizontal turbulence k_h (equation 4.2) are presented on figure 7.2. In Chapter 6 it was found that the Svensson model, because of the deficiencies on its

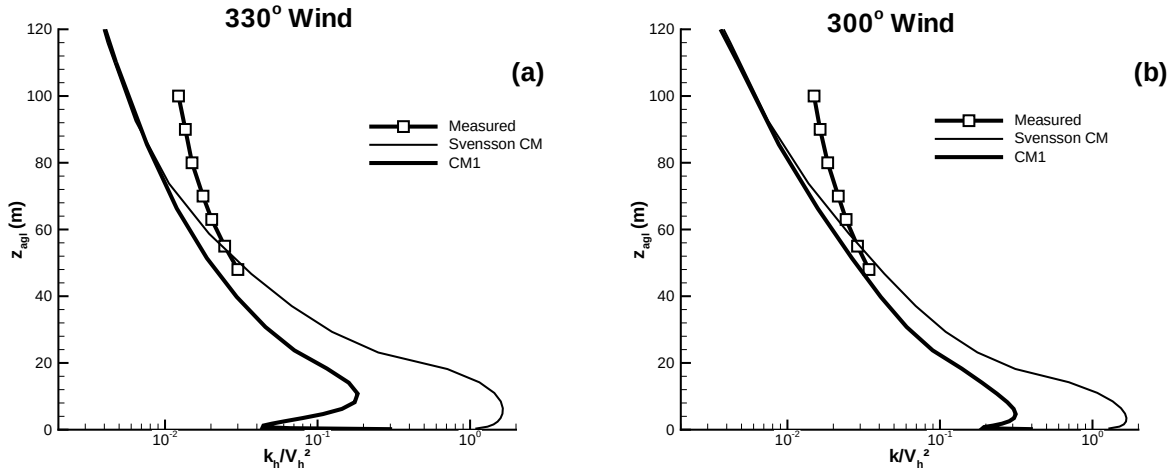

Figure 7.2: Turbulent kinetic energy profiles at mast M208, in the case of 330° (a) and 300° (b) winds.

formulation would tend to overpredict the turbulence levels. This conclusion however is not supported by the results in Chapter 4 which showed lower TKE compared with field data. Apparently based on figure 7.2, and although the Svensson model predicts higher turbulence levels compared to other models, it is still lower when compared with field data. Its level of agreement with field data is even better than the CM1 model whose development is much sounder.

A more detailed analysis of figure 7.2 reveals the following: the effects or the differences between the two models cannot reach beyond 80 m *agl*, i. e., about 3× the canopy height. Differences between computational results and field data above that heigh (the region where the discrepancies with the field data are greater) cannot be attributed to the canopy model.

The effect of the canopy models, as expected, occurs mostly within the canopy height and is much reduced at two canopy heights above ground level. Unfortunately this is a region not covered by the field data and which cannot be used to decide the quality of the two models. Based on the analysis in Chapters 5 and 6, it is our believe that the field data for $z < 40$ m could be closer to the CM1 results. This is reinforced by recent discussions

RES[1] staff, that noticed the overprediction of the TKE results in many other instances, contrary to what was noticed in the case of the French study, and *ad-hoc* corrections have been used in order to impare the agreement with turbulent field data.

The better agreement of Svensson results with field data is apparent and fortuitous, because it results of the crossing of the field data line with computational results line. This crossing is a consequence of higher values produced by Svensson model closer to the ground, which we believe to be wrong.[2] The results as given by CM1 are closer to field data, with the ability to replicate the field data trend and the differences in magnitude cannot be attributed to the model but to other aspects or parameters of the computer simulations, as shown in section 7.4.

7.3.2 South-Easterly winds (120° and 150°)

In the case of 120° and 150° winds, facing a more complex upwind orography, the CM1 wind velocity results (figures 7.3) yields a higher velocity value below canopy height, when compared to Svensson and Häggkvist (1990) model. In the case of the 120° direction, the "S shape" of the vertical profile is now smoothed, practically not showing a negative slope. However, a large improvement was not expected from a single computer simulation of a single direction, for the reasons in section 4.3.3.2. For the 150° direction, a slight improvement in the velocity profile was found.

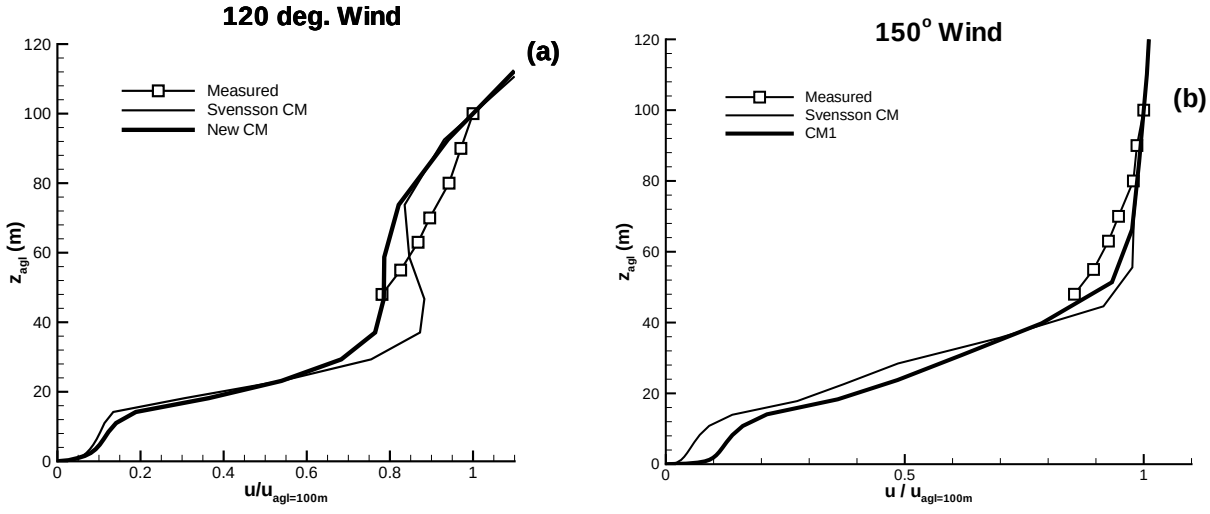

Figure 7.3: Velocity profiles at mast M208, in the case of 120° (a) and 150° (b) winds.

[1]Renewable Energy Systems Ltd., UK

[2]Note that the logarithmic scale was used in the horizontal axis, and the results given by either models differ by one order of magnitude and cannot be both close to the experimental data, that we do not know.

Regarding the vertical profiles of the turbulent kinetic energy, CM1 produce the turbulence intensity predicted by CM1 within the canopy was lower compared with the previous results. For 120° direction, these values remain slightly lower than those obtained by "Svensson CM", up to 70 m above ground level; at these levels, the profile presents values that are closer to the field measurements. For the 150° direction, the CM1 turbulence profile is also much less intense below canopy height, and the model still largely under-predicts the experimental values by two orders of magnitude.

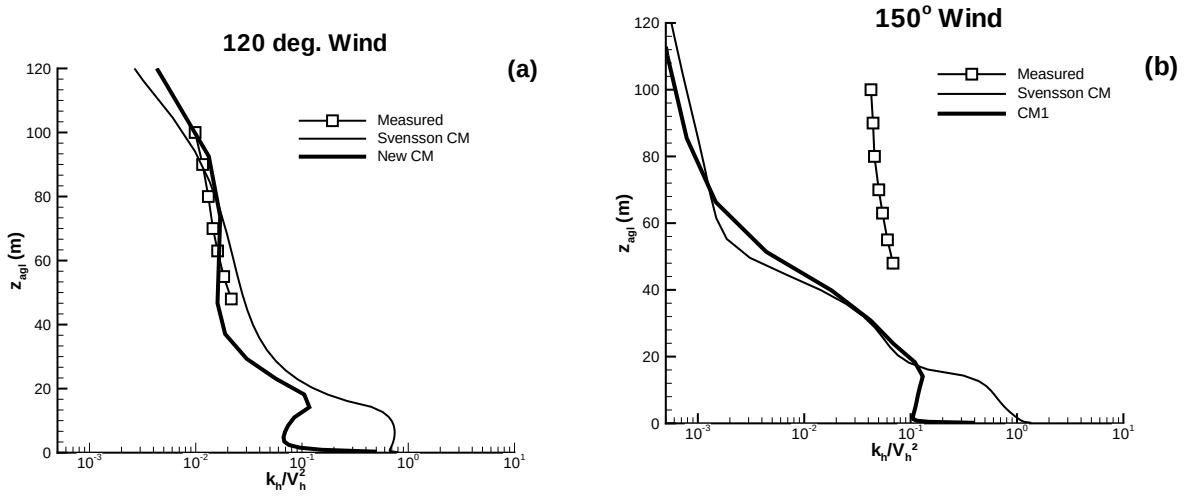

Figure 7.4: Turbulent kinetic energy at mast M208, for 120° (a) and 150° (b) wind directions.

7.4 Turbulence at Higher Distances above Ground Level

It was shown that the new model CM1 could not noticeably improve the TKE profiles. In this section we will try to understand the reasons for that and find solutions to deal with it.

Figures 7.5 shows the orange transparent iso-surfaces for $k = 4.0$ m^{2}s^{-2} as predicted by CM1 (top) and "Svensson CM" (bottom). The orography of the site is presented in white and grey surface, with a dark green patch representing the canopy zone. The referred orange transparent iso-surfaces show a high turbulent kinetic energy "bubble" above the forested area, that is propagating to higher altitudes and downstream (figure 4.16). On areas where we only considered surface roughness (white orography, outside the dark green canopy patch), the highest values of turbulent kinetic energy remain close to the ground. The canopy models turbulent footprint on the whole flow is much different

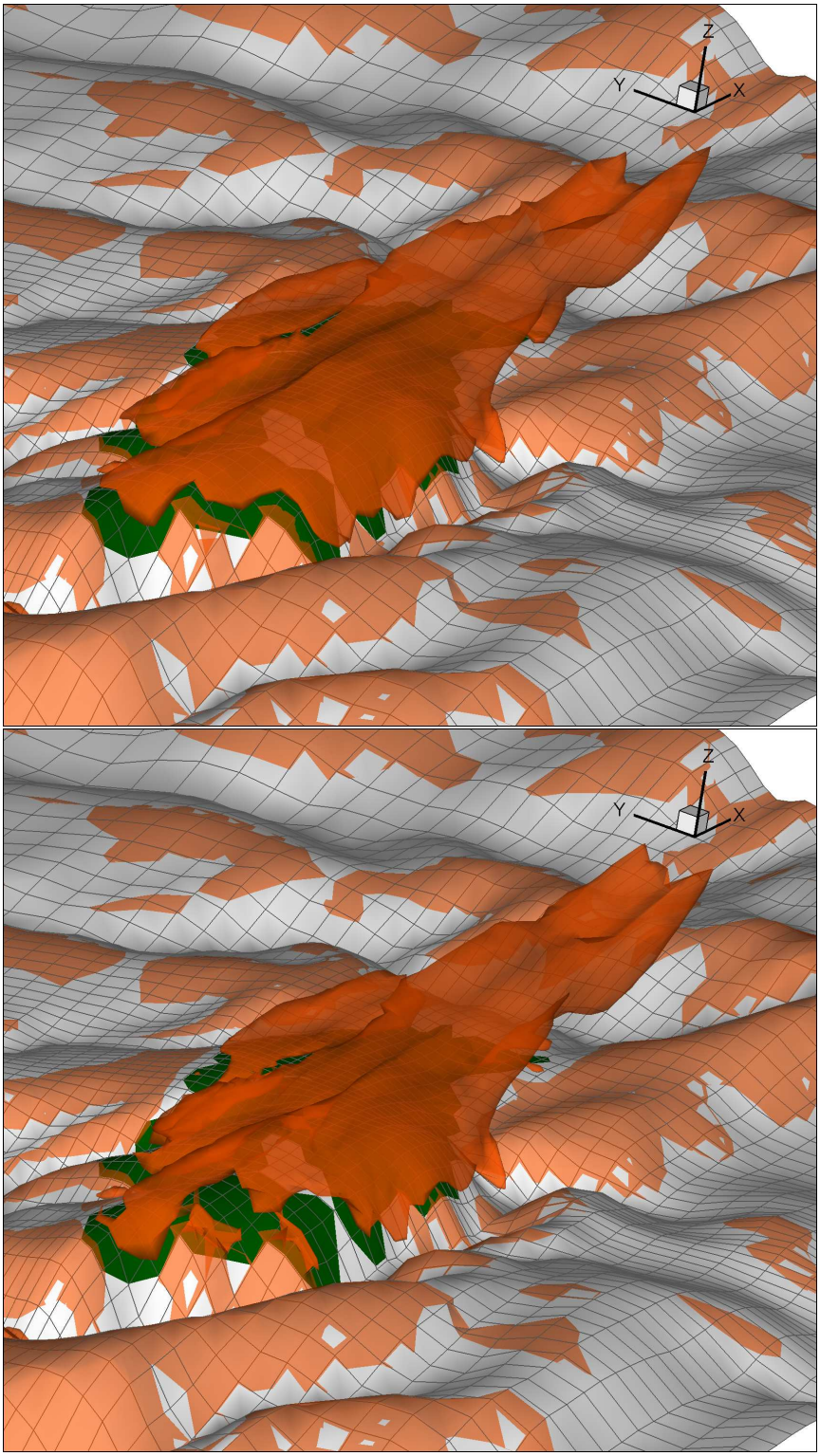

Figure 7.5: Turbulent kinetic energy iso-surfaces for $k = 4.0\text{m}^2\text{s}^{-2}$ over the French case topography (vertical scale amplified 3×) . The canopy area considered in calculations is represented as a dark green patch. Results obtained for 120° wind direction, using "CM1" (top) and "Svensson CM" (bottom).

from that obtained using surface roughness alone, i.e., with no canopy present. For these cases, the TKE is not capable to develop itself vertically and stays close to the ground, in contrast with the two canopy models, which yield a high turbulent region whose tail grows downstream and well above the forested area.

The only canopy patch that was modelled was the one represented in figures 4.9 or 7.5. However, it is known that the whole region is forested and it is most likely that the higher levels of turbulence at 70 m *agl* (figure 7.2) originated in other forested areas, outside the integration domain, have been convected to higher distances above ground level, as shown in figure 7.5. To confirm this analysis, some computer experiments were done, considering a larger extension of canopy or higher surface roughness. This had the effect of improving considerably the results with respects to the field measurements (figure 7.6). This was obtained with no changes to the velocity profiles results.

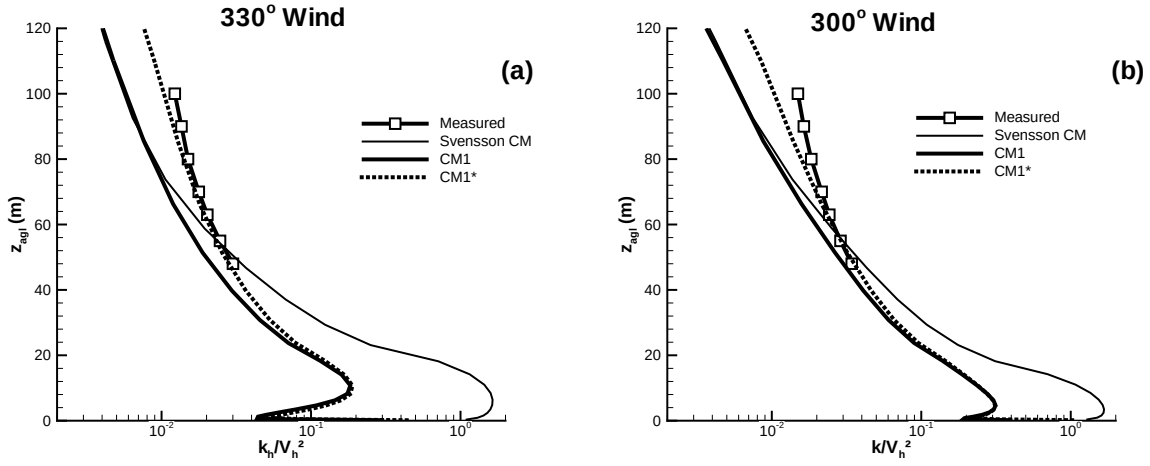

Figure 7.6: Turbulent kinetic energy profiles at mast M208, in the case of 330° (a) and 300° (b) winds. CM1* results were obtained considering an additional rectangular canopy upstream, (between -5000 and -3500 m relatively to mast position), and increasing the surface roughness from 0.03 m to 0.05 m.

No simulations were made for 120° winds, since its TKE previous results were already satisfactory. By contrast, calculated k profiles for 150° winds were very far from field measurements. Some experimental calculations were made, using more TKE in the inlet conditions and using canopy all over the domain. Figure 7.7 shows that these drastic modifications may render the TKE results more realistic, producing acceptable velocity results.

These results show that, with some reasonable adjustments, we can reach practically the same measured TKE levels at 100 m *agl*, without compromising the previous satisfactory velocity results and k profiles at lower heights. It also emphasizes the importance of fully characterizing the domain in terms of canopy regions and terrain roughness areas.

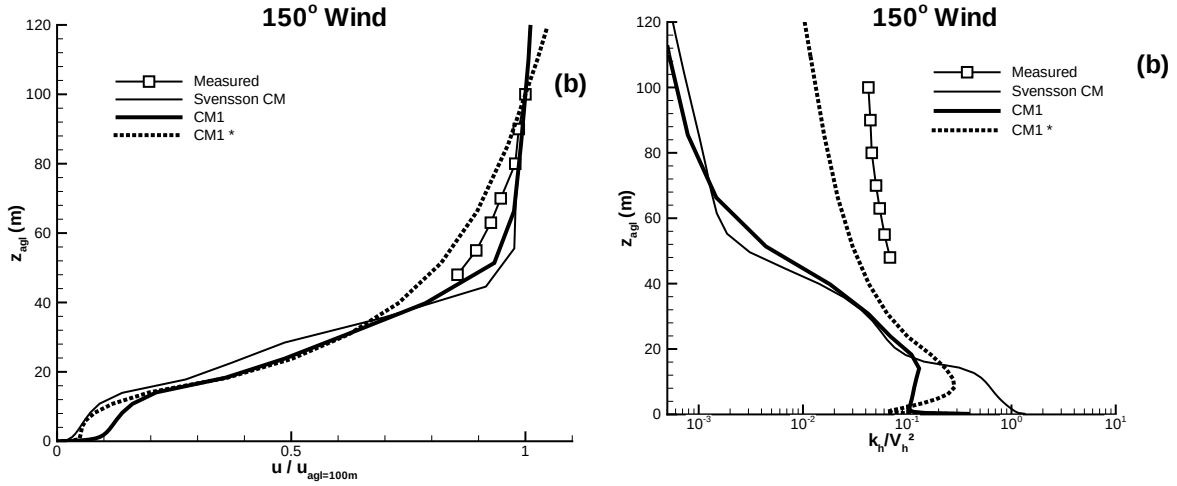

Figure 7.7: Velocity (a) and turbulent kinetic energy (b) profiles at mast M208, in the case of 150° winds. CM1* results were obtained considering canopy all over the domain, and considering for the incoming wind, upstream the domain, a 20 m roughness (wile in the domain surfaces a 0.03m roughness was used).

7.5 Conclusions

After revisiting the French case with the new canopy constant set CM1, we concluded that:

1. In general, and despite the similarity between the new results and those in Chapter 4, the CM1 improved slightly the agreement between computational and experimental results.

2. The CM1 k values inside the forest and in its vicinity were about one order of magnitude lower than "Svensson CM", which is closer to the measurements vertical profile trend. This confirms the practice established among the users of the VENTOS® code for engineering purposes, who have empirically noticed that the "Svensson CM" over-predicted the turbulence.

3. The TKE is very sensitive to inlet flow conditions and to canopy and surface roughness considerably far away from the region under study. Since the turbulent behaviour is an important issue of wind farm characterization, it is highly recommended that the canopy distribution over the whole domain be well defined.

Chapter 8

Conclusions and Future Work

8.1 Conclusions

In this work, simulations were made over simple and complex terrain, with and without forest canopies, with the purpose of reaching an adequate forest canopy model to be used in wind flow simulations around and over wind farm locations.

To illustrate the importance of non-linear models to resolve the wind flow over a mountainous region, the *Serra de Alvoaça* wind park site was studied using VENTOS®CFD (Chapter 3). Its location along a mountain ridge, with high terrain complexity, produced dramatic changes in the wind conditions, from the windward to the leeward side of the ridge, along with a non-stationary wind behaviour in the wake of the mountain.

CFD code predictions proved to be better than WAsP's, confirming the field measurements. The results also showed that the larger slope of the terrain upstream of the higher locations of the park deflects the wind vertically, with a consequent reduction of the horizontal wind velocity, producing unsteady wind conditions and high turbulence intensity, which makes these locations less suitable for turbine siting. Turbine locations were planned along a narrow corridor, where the wind conditions were the best in terms of wind speed, and do not suffer from high turbulence or wind shear.

In the next step (Chapter 4), our study advanced to include forest canopy. Computer simulations were made to simulate wind flow over forests at two real sites, in Scotland and in the South of France. The canopy model used was that proposed by Svensson and Häggkvist (1990), made to be used with the $k - \varepsilon$ model.

Results at the Scottish site, after the canopy model was added, showed better agreement with the field data. Computer flow simulations highlighted the wind flow structure caused by the trees. Numerical results also showed complex interactions among the wind direction, the terrain shape and additional wakes due to different forest patches distributed over the

region of interest. This was strongly dependent on the wind direction. Calculations with different values of canopy density showed the importance of this parameter, and that it is a major source of uncertainty in real canopy flows.

Results in the French region highlighted even more the need for a canopy model. It was possible to replicate the vertical profile of the horizontal velocity in most of the cases. The 120º winds were a more difficult challenge. Only the average of computer simulations for winds between 105º and 135º agreed with the measurements and revealed many of the detailed features of the wind flow and the importance of resolving all the geometrical details of both the forest and the orography.

It was also observed that the presence of canopy regions can augment the turbulence levels as much as two orders of magnitude, when compared with simulations performed without the canopy model.

The next step was to explore and test the several canopy models available in the literature (Chapter 5). Meanwhile, some LES on this subject were made, over a continuous forest and a forest clearing, following Shaw and Shumann (1992) and later works. Among the four RaNS canopy models tested (Svensson and Häggkvist, 1990; Green, 1992; Liu et al., 1998; Sanz, 2003; Katul et al., 2004), some of them completely fail to mimic the physics of turbulence as shown by LES, although they may produce acceptable velocity or TKE profiles.

The "Svensson" model, previously used in Chapter 4, performed well in the velocity prediction but fail in the TKE prediction by showing very large k values. The "Svensson" model and "Liu" model completely fail to mimic the physics of turbulence, when we observe the budget of the TKE equation, and compare it to LES. Only "Sanz" and "Green" models presented a comparable behaviour to LES on this issue.

The Sanz (2003) canopy model was the more correct and balanced canopy model, for the case in question. Velocity and TKE profiles are similar to those obtained by LES and the budget of turbulent kinetic energy showed that this canopy model was the one that better described the relative magnitude of the several mechanisms at play inside the roughness sub-layer, using the LES as the benchmark result.

Our next step was to explore the possibility of adjust canopy model constants using the RaNS k-ε-$\overline{v^2}$-f formulation (Chapter 6). Some relations were obtained that allowed us to explicitly determine canopy model β_p and β_d terms. Although it uses RaNS k-ε-$\overline{v^2}$-f formulation, its constants applied to the k-ε turbulence model improved results regarding velocity and TKE vertical distribution and, peculiarly, a combination of atmospheric (for k-ε) and standard (for $\overline{v^2}$-f) RaNS turbulence model constants produce the best TKE terms profiles, regarding LES results. This constant set named CM1, used under k-ε turbulence model, fielded the best agreement with the benchmark LES of the same flow. The complete constant set is the following:

	k-ε constants					Canopy model constants		
	C_μ	σ_k	σ_ε	$C_{\varepsilon 1}$	$C_{\varepsilon 2}$	β_p	β_d	$C_{\varepsilon 4} = C_{\varepsilon 5}$
CM1	0.033	1.0	1.85	1.44	1.92	0.17	3.37	0.9

The new canopy model constants CM1 present also better results than the "Sans CM".

The use of CM1 in the k-ε-$\overline{v^2}$-f turbulence model brings no significant improvement to canopy model results. In addition, it implies a larger calculation time.

As a way of bringing the present study to an end, it was decided to see whether the computer simulation of the flow over the French forest could be improved (Chapter 7). In general, and despite the similarity between the new CM1 canopy model and the previous results (using "Svensson" model), we can conclude that the CM1 slightly improved this agreement between computational and experimental results. The CM1 k values inside the forest and in its vicinity were about one order of magnitude lower then "Svensson CM", which confirms the practice established within the engineering users of the code VENTOS®, that have empirically noticed that "Svensson CM" over-predicted the turbulence.

It was also observed that TKE results are very sensitive to inlet flow conditions and to canopy and roughness considerably far away from the studied zone, which recommends to have attention to the canopy distribution even far away from the zone under study.

8.2 Future Work

Among the subjects covered by the present dissertation, different lines for possible future development have emerged and are shown here, organized in three main topics: continuing the appraisal of the canopy model under a wider range of flow and conditions; searching new relationships that can contribute to a set of canopy related constants based on more solid and consistent assumptions; and lastly, extending the modelling approach and methodology used here to a different wind engineering problem - the wake of a wind turbine.

1. Concerning the model appraisal, there is a need for performing this same exercise under more demanding conditions, also closer to real cases. The first one is the flow over idealized hills (e.g., sinusoidal), totally or partially covered with forest canopy. The study by Brown et al. (2001), with some LES results, and the laboratory data by Poggi and Katul (2007a,b), seem to be a good basis for such exercise. A more extensive comparison with field data than the one included in this dissertation is already being carried out jointly with RES (Renewable Energy Systems Ltd. - UK) based on the measurements of the flow over consecutive forested hills. This is a case with long term data where computer simulations using previous versions of the canopy model (based on Svensson and Häggkvist (1990)) did not perform satisfactorily.

2. The presently proposed canopy model constant set, CM1, is not a finished piece of work. Some questions remain unanswered, namely the over-prediction of k and ε fields, when compared to LES results, and the correct values for $C_{\varepsilon 4}$ and $C_{\varepsilon 5}$, i.e. a relationship that could not be found via the additional equations for the k-ε-$\overline{v^2}$-f turbulence model. These two problems, which deserve future attention, might be connected, as shown by preliminary experiments, assuming $C_{\varepsilon 4} \neq C_{\varepsilon 5}$, and maintaining the condition (6.18).

   Another possibility for determining the canopy model parameters is via the LES results and the evaluation of the individual terms of the transport equation that can lead us to the values of the canopy model parameters β_p, β_d, $C_{\varepsilon 4}$ and $C_{\varepsilon 5}$.

   The work by Dupont and Brunet (2007), in the Final Note to Chapter 6, can be an used to benchmark future studies involving a more detailed analysis of the CM1 constant set.

3. An important issue to be included in a CFD code for simulation of wind farm behaviour is the turbine wake and its effect on the flow and interference with the other machines in the park. This is a problem of great practical relevance to wind energy engineering that can be tackled via discrete sources/sinks of momentum and turbulence, i.e. an identical methodology to the one adopted for modelling the canopy.

Bibliography

A. R. Brown, J. M. Hobson, and N. Wood. Large-eddy simulation of neutral turbulent flow over rough sinusoidal ridges. *Boundary-Layer Meteorology*, 98:411–441, 2001.

BWEA. Workshop on the influence of trees on wind farm energy yields. Technical report, BWEA-British Wind Energy Association, 2004. Workshop held at The Arthouse Hotel (Glasgow, Scotland), 17th March 2004. http://www.bwea.com/planning/trees.html (31 May 2004, 16:51).

F. A. Castro. *Numerical Methods for the Simulation of Atmospheric Flows over Complex Terrain (in Portuguese).* PhD thesis, Faculty of Engeneering of Porto, 1997.

F. A. Castro and J. M. L. M. Palma. VENTOS$^{\text{TM}}$: a computer code for simulation of atmospheric flows over complex terrain. Technical report, Available from the authors, 2002. 21 pp.

F. A. Castro, J. M. L. M. Palma, and A. C. Silva Lopes. Simulation of the Askervein flow. Part 1: Reynolds averaged Navier-Stokes equations ($k-\epsilon$ turbulence model). *Boundary-Layer Meteorology*, 107:501–530, 2003.

F. A. Castro, J. M. L. M. Palma, and J. C. Lopes da Costa. VENTOS$^{\text{TM}}$: a computer code for simulation of atmospheric flows over forested complex terrain. Technical report, Available from the authors, 2004.

S. Chester, C. Meneveau, and M. B. Parlange. Modeling turbulent flow over fractal trees with renormalized numerical simulation. *Journal of Computational Physics*, 2007. Article in press.

E. Dellwik, L. Landberg, and N. O. Jensen. Wasp in the forest. *Wind Energy*, 9:211–218, 2006.

S. Dupont and Y. Brunet. Edge flow and canopy structure: a large-eddy simulation study. *Boundary-Layer Meteorology*, 2007. doi: 10.1007/s10546-007-9216-3.

P. A. Durbin. Near-wall turbulence closure modelling without damping functions. *J. Theor. Comput. Fluid Dyn.*, 3:1–13, 1991.

P. A. Durbin. Separated flow computations with the $k - \varepsilon - v^2$model. *AIAA Journal*, 33: 659–664, 1995.

Michael J. Dwyer, Edward G. Patton, and Roger H. Shaw. Turbulent kinetic energy budgets from a large-eddy simulation of airflow above and within a forest canopy. *Boudary-Layer Meteorology*, 84:23–43, 1997.

EWEA. Prioritising wind energy research: Strategic reserach agenda of the wind energy sector. Technical report, EWEA–European Wind Energy Association, July 2005.

J. Finnigan. Turbulence in plant canopies. *Annual Review of Fluid Mechanics*, 32:519–571, 2000.

J. J. Finnigan and S. E. Belcher. Flow over a hill covered with a plant canopy. *Quarterly Journal of the Royal Meteorological Society*, 130:1–29, 2004.

H. Foudhil, Y. Brunet, and J.-P. Caltagirone. A fine-scale k-ε model for atmospheric flow over heterogeneous landscapes. *Environmental Fluid Mechanics*, 5:247–265, 2005.

M. Germano, U. Piomelli, P. Moin, and W. H. Cabot. A dynamic subgrid-scale eddy viscosity model. *Physics of Fluids A*, 3:1760, 1991.

R. S. Green. Modelling turbulent air flow in a stand of widely-spaced trees. *Phoenics J.*, 5:294–312, 1992.

I. N. Harman and J. Finnigan. A simple unified theory for flow in the canopy and roughness sublayer. *Boundary-Layer Meteorology*, 123:339–663, 2007.

IEC. Wind turbine generator systems – part 1: safety requirements. Technical report, IEC-International Electrotechnical Commission, Geneva, Switzerland, 1999. International Standard IEC 61400-1.

M. R. Irvine, B. A. Gardiner, and M.K. Hill. The evolution of turbulence across a forest edge. *Boundary-Layer Meteorology*, 84:467–496, 1997.

P. S. Jackson and J. C. R. Hunt. Turbulent wind over a low hill. *Quarterly Journal of the Royal Meteorological Society*, 101:929–955, 1975.

G. G. Katul, L. Mahrt, D. Poggi, and Christophe Sanz. One- and two-equation models for canopy turbulence. *Boundary-Layer Meteorology*, 113:81–109, 2004.

M. H. Kobayashi, J. C. F. Pereira, and M. B. B. Siqueira. Numerical study of the turbulent flow over and in a model forest on a 2D hill. *Journal of Wind Engineering and Industrial Aerodynamics*, 53:357–374, 1994.

B. E. Launder and D. B. Spalding. The numerical computation of turbulent flow. *Computer Methods in Applied Mechanics and Engineering*, 3:269–289, 1974.

D. R. Laurence, J. C. Uribe, and S. V. Utyuzhnikov. A robust formulation of the v2-f model. *Flow, Turbulence and Combustion*, 73:169–185, 2004.

J. Liu, J. M. Chen, T. A. Black, and M. D. Novak. $e - \varepsilon$ modelling of turbulent air flow downwind of a model forest edge. *Boundary-Layer Meteorology*, 72:21–44, 1998.

A. Silva Lopes, J. M. L. M. Palma, and F. A. Castro. Simulation of the askervein flow - part 2: Large-eddy simulations. *Boundary-Layer Meteorology*, 2007. Submited. Waiting for publication.

J. C. Lopes da Costa, F. A. Castro, J. M. L. M. Palma, and P. Stuart. Computer simulation of athmosferic flows over real forests for wind energy resource evaluation. *Journal of Wind Engineering and Industrial Aerodynamics*, 94:603–620, 2006.

S. Mao, Z.-G. Feng, and E. E. Michaelides. Large-eddy simulation of low-level jet-like flow in a canopy. *Environmental Fluid Mechanics*, 7:73–93, 2007.

W. J. Massman. An analytical one-dimensional model of momentum transfer by vegatation of arbitrary structure. *Boundary-Layer Meteorology*, 83:407–421, 1997.

Charles Meneveau, Thomas Lund, and William H. Cabot. A lagrangian dynamic subgrid-scale model of turbulence. *J. Fluid Mech.*, 319:353–385, 1996.

N. G. Mortensen, L. Landberg, I. Troen, E. L. Petersen, O. Rathmann, and M. Nielsen. WAsP utility programs. Technical Report Risø-R-995(EN), Risøo National Laboratory, Roskilde, Denmark, September 2004. URL `www.wasp.dk`.

D. E. Neff and R. N. Meroney. Wind-tunnel modelling of hill and vegetation influence on wind power availability. *Journal of Wind Engineering and Industrial Aerodynamics*, 74–76:335–343, 1998.

E. G. Patton. *Large-eddy simulation of turbulent flow above and within a plant canopy.* PhD thesis, University of California, Davis, 1997.

E. G. Patton, R. H. Shaw, M. J. Judd, and M. R. Raupach. Large-eddy simulations of windbreak flow. *Boundary-Layer Meteorology*, 87:275–306, 1998.

J. D. J.-P. Pinard and J. D. Wilson. First- and second-order closure models for wind in a plant canopy. *Journal of Applied Meteorology*, 40:1762–1768, 2001.

D. Poggi and G. G. Katul. Two-dimensional scalar spectra in the deeper layers of a dense and uniform model canopy. *Boundary-Layer Meteorology*, 121:267–281, 2006.

D. Poggi and G. G. Katul. Turbulent flows on forested hilly terrain: the recirculation region. *Quarterly Journal of the Royal Meteorological Society*, 133:1027–1039, 2007a.

D. Poggi and G. G. Katul. The ejection-sweep cycle over bare and forested gentle hills: a laboratory experiment. *Boundary-Layer Meteorology*, 122:943–515, 2007b.

S. B. Pope. *Turbulent Flows*. Cambridge University Press, 2000.

M. R. Raupach. Simplified expressions for the vegetation roughness lenght and zero-plane displacement as functions of canopy height and area index. *Boundary-Layer Meteorology*, 71:211–216, 1994.

M. R. Raupach and A. S. Tom. Turbulence in and above plant canopies. *Annual Review of Fluid Mechanics*, 13:97–129, 1981.

B. Ruck and E. Adams. Fluid mechanical aspects of the pollutant transport to coniferous trees. *Boundary-Layer Meteorology*, 56:163–195, 1991.

T. Saba. Effects of tower shading on anemometers - field data and wind tunnel investigations. In *Proceedings of the NZWEA Conference*, 2002.

C. Sanz. A note on $k-\varepsilon$ modelling on a vegatation canopy. *Boundary-Layer Meteorology*, 108:191–197, 2003.

R. Shaw and U. Shumann. Large - Eddy simulation of turbulent flow above and within a forest. *Boundary-Layer Meteorology*, 61:47–64, 1992.

B. Silva and A. Rodrigues. Parque eólico de Alvoaça - estudo e caracterização do regime de ventos. Technical report, INEGI-Instituto de Engenharia Mecânica e Gestão Industrial, Unidade de Energia e Ambiente, Abril 2005. Estudo elaborado para EDP Produção EM –Engenharia e Manutenção, S.A. Relatório técnico N. 2004/07/EE/11.

A. Silva Lopes. *Flow Simulation in Complex Geometries by Large Eddy Simulation (*in Portuguese*)*. PhD thesis, University of Porto, Portugal, January 2000.

A. Sogachev and O. Panferov. Modification of two-equation models to accont for plant drag. *Boundary-Layer Meteorology*, 121:229–266, 2006.

P. D. Stuart. The application of the VENTOS$^{\text{TM}}$CFD model to wind turbine micrositing. Technical report, RES-Renewnable Energy Systems, United Kingdom, August 2003.

H.-B. Su, R. H. Shaw, K. T. P. U, C.-H. Moeng, and P. P. Sullivan. Turbulent statistics of neutraly stratified flow within and above sparse forest from large-eddy simulation and field observations. *Boundary-Layer Meteorology*, 88:363–397, 1998.

U. Svensson and K. Häggkvist. A two-equation turbulence model for canopy flows. *Journal of Wind Engineering and Industrial Aerodynamics*, 35:201–211, 1990.

I. Troen and E. L. Petersen. *European Wind Atlas*. Risø National Laboratory, Denmark, 1989.

A. Verhoef, K. G. McNaughton, and A. F. G. Jacobs. A parametrization of momentum roughness lenght and displacement height for a wide range of canopy densities. *Hydrology and Earth Sciences*, 1:81–91, 1997.

J. L. Walmsley, J. R. Salmon, and P. A. Taylor. On the application of a model of boundary-layer flow over low hills to real terrain. *Boundary-Layer Meteorology*, 23:17–46, 1982.

J. D. Wilson, J. J. Finnigan, and M. R Raupauch. A first-order closure for disturbed plant-canopy flows, and its application to winds in a canopy on a ridge. *Quarterly Journal of the Royal Meteorological Society*, 124:705–732, 1998.

Z. Xie and I. P. Castro. Les and rans for turbulent flow over arrays of wall-mounted obstacles. *Flow, Turbulence and Combustion*, 76:291–312, 2006.

B. Yang, M. R. Raupach, R. H. Shaw, K. T. Paw U, and A. P . Morse. Large-eddy simulation of turbulent flow across a fores edge. part i: Flow statistics. *Boundary-Layer Meteorology*, 120:377–412, 2006.

W. Yue, M. C. Parlange, C. Meneveau, W. Zhu, R. van Hout, and J. Katz. Large-eddy simulation of plant canopy flows using plant-scale representation. *Boundary-Layer Meteorology*, 124:183–203, 2007.